Polar Cap Ionospheric Oscillations in the ULF Frequency Range Observed with SuperDARN HF Radar

A Thesis Submitted to the
College of Graduate Studies and Research
in Partial Fulfillment of the Requirements
for the degree of Master of Science
in the Institute for Space and Atmospheric Studies of Physics and Engineering Physics
University of Saskatchewan
Saskatoon

By
Grant L.T. Scoular

Permission to Use

In presenting this thesis in partial fulfilment of the requirements for a Postgraduate degree from the University of Saskatchewan, I agree that the Libraries of this University may make it freely available for inspection. I further agree that permission for copying of this thesis in any manner, in whole or in part, for scholarly purposes may be granted by the professor or professors who supervised my thesis work or, in their absence, by the Head of the Department or the Dean of the College in which my thesis work was done. It is understood that any copying or publication or use of this thesis or parts thereof for financial gain shall not be allowed without my written permission. It is also understood that due recognition shall be given to me and to the University of Saskatchewan in any scholarly use which may be made of any material in my thesis.

Requests for permission to copy or to make other use of material in this thesis in whole or part should be addressed to:

Department Head
Physics Rm 158
116 Science Place
University of Saskatchewan
Saskatoon, Saskatchewan
Canada
S7N 5E2

Abstract

Pc3-4 waves are recorded as geomagnetic pulsations with periods of 6-100s. They are generated at the bowshock and propagate to mid and auroral latitudes as Alfvén waves along closed magnetic field lines. At these latitudes Pc3-4 waves have been studied on the ground using magnetometers and in the ionosphere using HF radar. These waves have also been observed using magnetometers at polar latitudes even though there is no known propagation mechanism to the "open" field lines of the polar cap regions.

In this work we used PolarDARN stations at Rankin Inlet and Inuvik to attempt the first study of Pc3-4 waves in the polar cap regions using radar. In ground scatter data, Doppler velocity oscillations with frequencies in the Pc3-4 range were found to be a common daytime occurrence. The oscillations are spatially coherent and in phase along the beam's line of sight, matching lower latitude observations. However, upon further study it became apparent that the characteristics of the oscillations are different from those known for Pc3-4 waves.

The observed oscillations have a diurnal trend that shows peaks in activity at 7:00 and 14:00 MLT, where Pc3-4 oscillations have a diurnal peak at 10:30-11:00 MLT. In addition, poor coherence was observed between oscillations in radar and ground magnetic field variations at the nearby Taloyoak magnetometer. Further confounding the problem, we found that although the oscillations were coherent along the line-of-sight of the radar, poor coherence is observed when comparing oscillations in different beams separated by similar spatial scales. This finding counters both the spatial coherence observed along the beam's line of sight and the spatial coherence of Pc3-4 waves at auroral latitudes. We conclude that it is unlikely that the observed oscillations are the result of Pc3-4 ULF waves. We instead propose that the observed Doppler velocity oscillations are caused by a change in the ionization along the ray's path due to auroral particle precipitation.

Acknowledgements

Thank you to my parents for supporting me in my studies. Thanks goes to my supervisors Pasha Ponomarenko and J.P. St.-Maurice for their guidance and assistance. Thanks to the SuperDARN team for radar data. Thank you to I.R. Mann, D.K. Milling and the rest of the CARISMA team for CARISMA magnetometer data. CARISMA is operated by the University of Alberta, funded by the Canadian Space Agency. Thanks to Ray Greenwald for fruitful discussions on the nature of the phenomenon. Thank you to the University of Saskatchewan, The College of Graduate Studies and Research, the CSA and NSERC for funding this work.

Contents

List of Tables

List of Figures

List of Abbreviations

CARISMA	Canadian Array for Realtime Investigations of Magnetic Activity
HF	High Frequency
IMF	Interplanetary Magnetic Field
MHD	Magnetohydrodynamic
Pc	Continuous Pulsation
Pi	Irregular Pulsation
PolarDARN	Polar Dual Auroral Radar Network
SuperDARN	Super Dual Auroral Radar Network
UHF	Ultra High Frequency
ULF	Ultra Low Frequency
VHF	Very High Frequency

Chapter 1

Introduction

1.1 The Solar Wind

The solar wind is the result of the very high temperatures of the solar corona (millions of °K), which allows a fraction of the coronal plasma (95% H, 5% He) to escape the gravitational attraction of the sun (*Parks*, 1991).

A basic fluid model for the the solar wind was developed by Parker (*Parker*, 1958). This model assumes steady state and considers only pressure gradient and gravity acting on the solar plasma. The solar plasma was modeled as an isothermal ideal gas that expands away from the sun into interplanetary space, driven by the pressure gradient away from the sun. For a steady state condition, the particle flux must be constant as a function of radius. The decreasing gravitational force results in the solar wind speed increasing with radius to the sun, satisfying constant flux. The solar wind speed increases to become superthermal at the "critical" distance, given by

$$r_c = \frac{GMm_i}{4k_BT}\,, \tag{1.1}$$

where G is the gravitational constant, M is the mass of the sun, m_i is the average ion mass, k_B is Boltzmann's constant, and T is temperature. Near the Earth, the speed of sound is approximately 100 km/s and the solar wind has a speed of approximately 500 km/s.

Although useful, the Parker model is a simplified model of the solar wind. For the solar wind flux to remain constant the solar wind velocity must increase before becoming constant as the distance goes to infinity. The only solution where this condition is met has very specific initial conditions, with any deviation in initial flux resulting in a plasma that does not escape or become supersonic. In the Parker model the isothermal assumption is not realistic. As the plasma expands it must cool. In addition, there is heat transfer in a pocket of solar wind plasma. If we consider the velocity distribution of the solar wind plasma we will see that some particles have more energy than others.

Some particles will have sufficient energy to escape the sun's gravity while others will not. In Figure 1.1 we show a cartoon of the distribution function for the radial velocity of particles. In a volume of space, particles will have both positive and negative velocities, corresponding to particles flowing away from before coming back towards the sun. As the distance increases, fewer and fewer particles are coming back as the gravitational field dies off (*Schunk and Nagy*, 2000). The result is that the average velocity of the gas becomes supersonic regardless of the initial flux.

The solar wind carries the interplanetary magnetic field (IMF). The frozen in theorem states that magnetic field lines in an infinitely conducting plasma will move with the plasma. If we approximate the solar wind plasma as having infinite conductivity, the magnetic field of the sun will be "frozen in" with the plasma of the solar wind. So, as the solar wind travels away from the sun into interplanetary space, its magnetic field lines are carried with it. Without the presence of the solar wind we would expect to see an approximately dipolar magnetic field from the sun

$$B_r(r) = B_0 \sin\theta \left(\frac{R}{r}\right)^3 \tag{1.2}$$

(*Hundhausen*, 1995), where R is the sun's radius, r is the distance from the sun, and θ is the angle from the sun's equator (latitude). However, as the solar wind flows in the radial direction, field lines move with it and radial magnetic flux is conserved. The radial magnetic field of the sun in this case is

$$B_r(r) = B_0 \left(\frac{R}{r}\right)^2 \tag{1.3}$$

(*Hundhausen*, 1995). The sun's rotation affects the structure of the solar wind, rotating with a period of approximately 25.4 days at the sun's equator (*Hundhausen*, 1995). Field lines on the surface of the sun will rotate with it, but field lines frozen into the interplanetary plasma move radially with the ejected plasma. This creates a "garden hose" effect with the azimuthal field now given as

$$B_\phi(r) = -B_0 \frac{\omega}{u} \frac{R^2}{r} \tag{1.4}$$

(*Hundhausen*, 1995), where ω is the angular frequency of the sun's rotation and u is the radial speed of the solar wind which is assumed to be constant. The azimuthal field falls off more slowly than the radial field, resulting in a spiral structure of the IMF; the IMF is therefore increasingly in the azimuthal direction as radius increases.

The frozen-in field dominates over the dipolar field at distances greater than 2 solar radii (*Hund-*

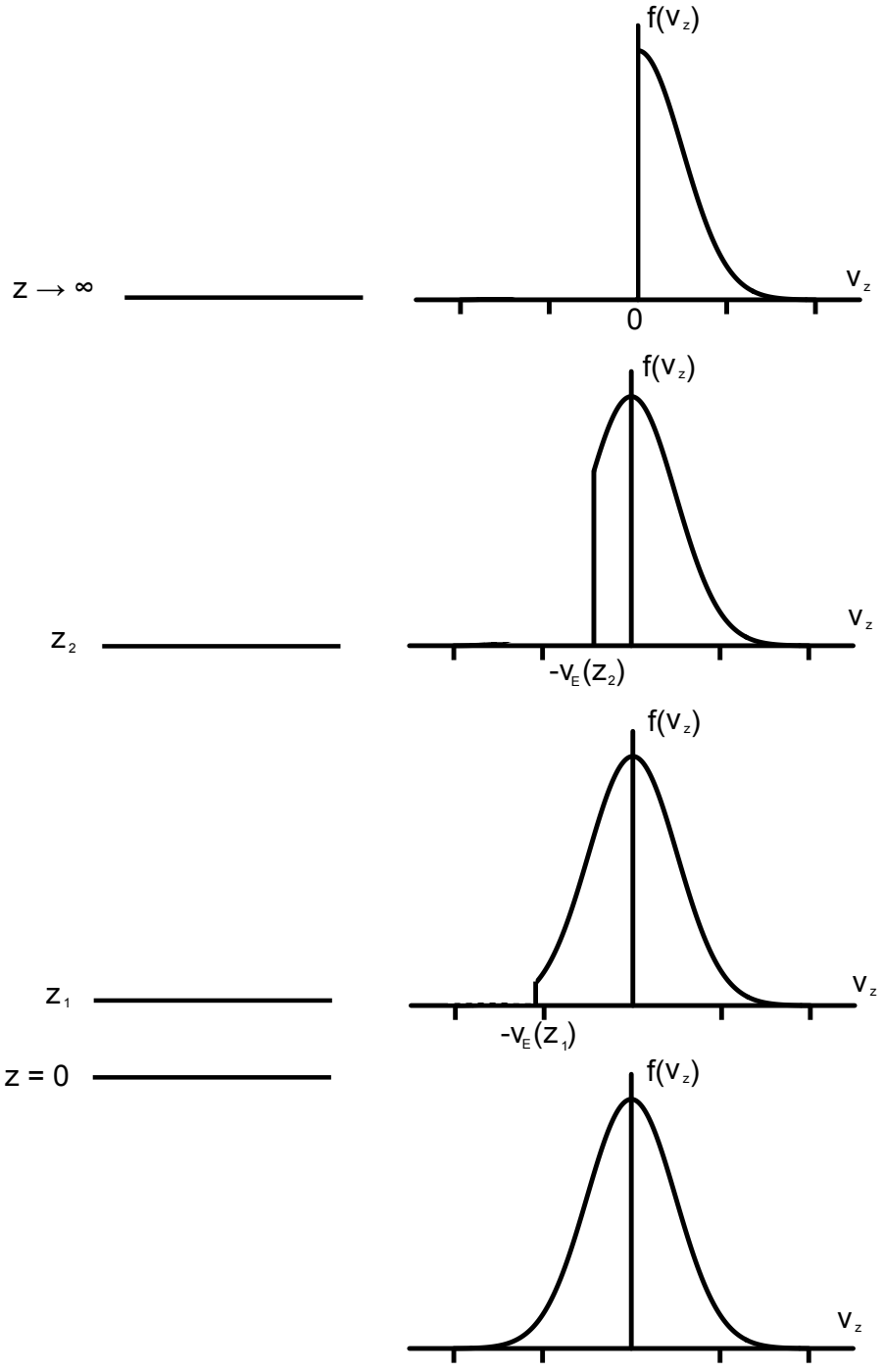

Figure 1.1: The radial velocity distribution function for solar wind particles. Low energy particles are unable to reach large distances, resulting in a cutoff of the distribution function as height increases. The average energy increases with height as low energy particles fall off. Adapted from 2011 Phys 821 class notes by J.P. St.-Maurice

hausen, 1995). Near the orbit of the Earth (approximately 215 solar radii), the IMF strength is of the order of 10^{-9} T. The angle that the direction of the IMF, determined by its radial and azimuthal components, makes with the radial sun-Earth line is called the cone angle, which varies, but is typically approximately 45°.

At approximately the plane of the sun's equator, the direction of the IMF will change from radially outward to radially inward. From Ampere's law, $\vec{\nabla} \times \vec{B} = \mu_0 \vec{J}$, at this boundary, a current will flow. Because of the geometry of the magnetic field, the current will be perpendicular to the magnetic field direction. This is called the current sheet. The current sheet is not perfectly flat, but instead ripples above and below the ecliptic plane. As the Earth passes through the current sheet in its journey around the sun, the IMF seen at the Earth regularly shifts from inward to outward and vice-versa. The sign of the magnetic field component along the North-South line, B_z, changes when the Earth crosses the current sheet.

1.2 The Earth's Magnetosphere

The Earth's magnetosphere is a region of space surrounding the Earth where plasma behaviour is dominated by the Earth's magnetic field. Beyond the magnetosphere, the IMF dominates. When the solar wind encounters the Earth's magnetic field it is deflected by the Lorentz force, preventing the penetration of high energy charged particles to low latitudes. The Earth's magnetic field effectively shields the Earth from high energy charged particles coming from the sun.

The boundary of the magnetosphere is called the magnetopause. It marks a surface where most of the particles of the solar wind are deflected by the Earth's magnetic field. On the sunward side of the magnetopause, the deflection of the solar wind plasma causes the solar wind to slow from supersonic to subsonic velocities. This boundary, known as the bowshock occurs at approximately 14 R_E from the Earth on the sunward side (*Burgess*, 1995). Between the magnetopause and the bowshock is the magnetosheath. When the solar wind attempts to flow around the magnetopause, it slows, causing temperatures to increase. The magnetosheath is a region of shocked solar wind plasma, so it is slower, hotter and more turbulent than the plasma in the solar wind (*Hargreaves*, 1992).

Further inside the magnetosphere the Earth's magnetic field can be approximated as being dipolar. On the Earth's surface at the equator, the Earth's magnetic field has an approximate strength of 0.3×10^{-4} T. As we move to higher latitudes the dipolar approximation ceases to apply. At these

high latitudes, field lines do not close within the Earth's magnetosphere. Instead, reconnection occurs between the Earth's field and the IMF. This happens when two magnetic field lines of opposite directions sum to zero at a point. At this point the magnetic field lines "break" and merge with each other. Reconnection results in connecting the magnetic field of the polar caps to the IMF so that the polar cap field lines are called "open". These "open" field lines are eventually pushed by the solar wind to the magnetotail, where they again reconnect back on the nightside, forming the plasma sheet. A diagram of the field lines in different regions of the magnetosphere is shown in Figure 1.2. In the diagram, the "open" field lines lie on the nightside of the neutral point in the north and south lobes.

The polar cap maps to the magnetotail lobes. The lobes are the regions in the magnetotail where there are open field lines. This region extends to greater that 200 R_E. Particles in this region have energies of up to 100 eV. The field lines eventually close at approximately 60 R_E forming the plasma sheet boundary. The plasma sheet is the closed field line region located between the North and South lobes in the magnetotail.

The cusp, shown in Figure 1.2 as the line between the neutral point and the Earth, is found at high latitudes on the sunward side of the Earth. Its center is near noon and it has a width of a few hours. The cusp marks where the magnetosphere transitions from "open" to "closed" field lines. Because there are no magnetic field lines to cross, particles from the magnetosheath can penetrate to low latitudes at the cusp with energies of 30-100 eV. The cusp field lines connect to the region where reconnection occurs and the magnetic field has a zero value (*Hargreaves*, 1992).

The boundary between the "open" and "closed" field lines is on average located at approximately 77° geomagnetic latitude (*Fraser-Smith*, 1982). This is not a fixed boundary. The position varies throughout the day, moving equatorward at night and with increased geomagnetic activity. The auroral regions are located equatorward from the boundary at high latitudes within the closed field line geometry, extending between approximately 67-77° (*Carlson and Egeland*, 1995). Like the polar cap boundary, this region's latitude varies with time of day and geomagnetic activity level.

1.3 The Earth's ionosphere

At altitudes above 80 km the Earth's atmosphere is ionized by solar UV, EUV and X-ray radiation. This region is known as the ionosphere. It typically extends from 80 km to as high as 1000 km above the Earth's surface, although the upper boundary is not well defined.

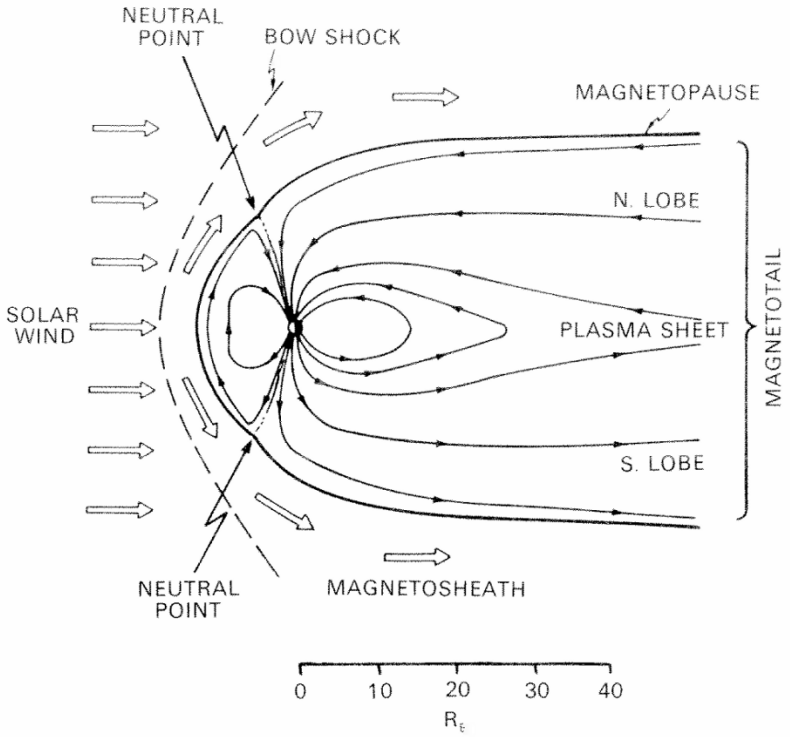

Figure 1.2: The regions of the Earth's magnetosphere (*Hargreaves*, 1992)

Ionospheric currents are derived assuming a steady state and a strong control by the Lorentz force and friction through collisions. The friction is between neutrals and the charged particles. Current is given by Ohm's law as

$$\vec{j} = \overleftrightarrow{\sigma} \cdot \vec{E}\,, \tag{1.5}$$

where $\overleftrightarrow{\sigma}$ is the conductivity tensor and $\vec{E}$ is the electric field. The conductivity tensor is given by *Blelly and Alcaydé* (2007)

$$\overleftrightarrow{\sigma} = \begin{bmatrix} \sigma_P & \sigma_H & 0 \\ -\sigma_H & \sigma_P & 0 \\ 0 & 0 & \sigma_0 \end{bmatrix}$$

$$\begin{aligned} \sigma_P &= \left[1 - \frac{1}{m_e\nu_{ei}}\frac{\alpha}{\alpha^2+\beta^2}\right]\frac{e^2 n}{m_e\nu_{ei}} \\ \sigma_H &= \frac{1}{m_e\nu_{ei}}\frac{\beta}{\alpha^2+\beta^2}\frac{e^2 n}{m_e\nu_{ei}} \\ \sigma_0 &= \left[\frac{\frac{1}{m_e\nu_{en}}+\frac{1}{m_i\nu_{in}}}{\frac{1}{m_e\nu_{ei}}+\frac{1}{m_e\nu_{en}}+\frac{1}{m_i\nu_{in}}}\right]\frac{e^2 n}{m_e\nu_{ei}} \\ \alpha &= \frac{1}{m_e\nu_{ei}} + \frac{1}{m_e}\frac{\nu_{en}}{\nu_{en}^2+\omega_e^2} + \frac{1}{m_i}\frac{\nu_{in}}{\nu_{in}^2+\omega_i^2} \\ \beta &= \frac{1}{m_e}\frac{\omega_e}{\nu_{en}^2+\omega_e^2} - \frac{1}{m_i}\frac{\omega_i}{\nu_{in}^2+\omega_i^2}\,, \end{aligned} \tag{1.6}$$

where ν_{en} is the electron-neutral collision frequency, ω is the gyrofrequency $\frac{qB}{m}$, n is the electron density, and the subscripts denote if the parameter is for ions or electrons. Also, σ_P, σ_H and σ_0 are the Pedersen, Hall and parallel conducitivities, respectively.

While the ion and electron gyrofrequencies are constant, the collision frequencies depend on densities and as a result they change with altitude as shown in Figure 1.3. As a result, the conductivities change with height, shown in Figure 1.4. The electron cyclotron frequency is much greater than the collision frequency in the ionosphere regardless of amplitude. The Hall conductivity therefore dominates for electrons: namely they basically undergo $\vec{E} \times \vec{B}$ drift.

$\vec{E} \times \vec{B}$ drift dominates when the cyclotron frequency is much greater than the collisional frequency, $\omega \gg \nu$ (*Kivelson*, 1995). In the absence of an electric field the charged particle will simply gyrate around the magnetic field line. Assuming a positively charged ion, if there is an electric field perpendicular to the magnetic field it will accelerate the particle along the electric field. However, the magnetic field will cause the ion to change direction. When the ion is accelerated by the electric field, the ion gyroradius increases. However, when the ion is moving anti-parallel to the electric field, it decelerates and the gyroradius decreases. This process is shown in Figure 1.5. The resulting

motion has velocity given by

$$\vec{v} = \frac{\vec{E} \times \vec{B}}{B^2} \,. \tag{1.7}$$

Because both the ion and electron response to the electric field and their gyration direction are opposite, ions and electrons drift in the same direction.

Pedersen drift dominates when the collision frequency is much greater than the gyrofrequency. In this case collisions with neutral particles will stop the charged particle before the effects of the magnetic field can be felt. Ions and electrons will flow in opposite directions along the electric field.

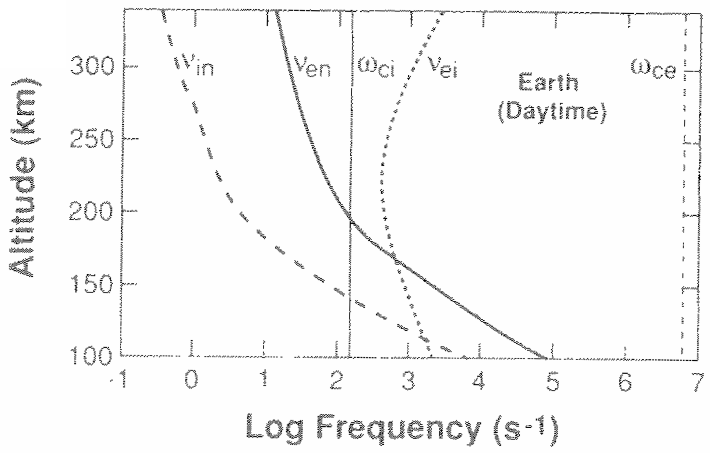

Figure 1.3: Profile of collision frequencies and gyrofrequencies in the Earth's ionosphere (*Luhmann*, 1995)

There are several distinct regions of the ionosphere characterized by altitudinal variation in electron density, shown in Figure 1.6. The E region, typically observed at approximately 90-130 km with a peak near 120 km is characterized by electron densities during the day of the order of 10^5 cm^{-3}. The dominant positive ions in this region are [NO^+] and [O_2^+]. Throughout the E region, conductivities vary as the ratio of the ion-neutral collision frequency and ion cyclotron frequency changes. Below 120 km, the ion cyclotron frequency is much smaller than the ion-neutral collision frequency. As a result, the ions flow along the electric field. In the E-region, above 120 km, ion collisions are infrequent, resulting in Hall conductivities that are comparable to Pedersen

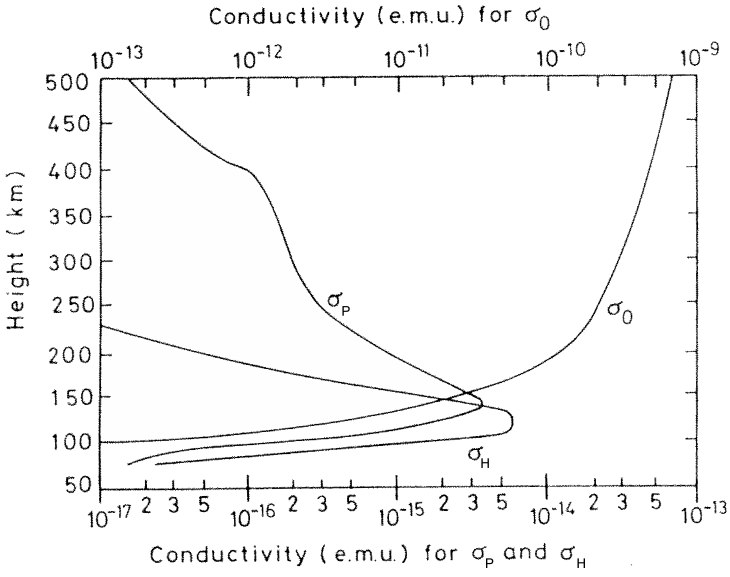

Figure 1.4: Conductivity profile of the Earth's ionosphere. Parallel, Pedersen and Hall conductivity are labelled as σ_0, σ_P and σ_H. The Hall and Pedersen conductivities peak at different altitudes within the E region. So that they can be shown in the same plot, the x-axis for parallel conductivity is shown above the figure. (*Hargreaves*, 1992)

conductivities. Hall and Pedersen conductivies both peak in the E region.

The F region is above the E region, and reaches a peak at approximately 300 km with daytime electron densities of the order of 10^6 cm^{-3}. The dominant ion at these heights is $[O^+]$. In this region, the neutral density is small so that collisions between the neutrals and ions are rare, $\omega_i \gg \nu_i$. The Hall conductivity dominates, causing $\vec{E} \times \vec{B}$ drift for both ions and electrons. No net current results from this motion as electrons and ions move together. Instead, a bulk motion of the plasma occurs.

The conductivity along magnetic field lines is only limited by collisions. As a result, at ionospheric altitudes, parallel conductivity is very high. When an electric field is directed along a magnetic field line the field is quickly canceled out by flowing electrons. Electric fields can generally only be sustained perpendicular to the Earth's magnetic field. If there is a localized build up of plasma in a region, high conductivity along magnetic field lines quickly diffuses the density perturbation along the field line creating a field aligned structure in the ionosphere. These structures have

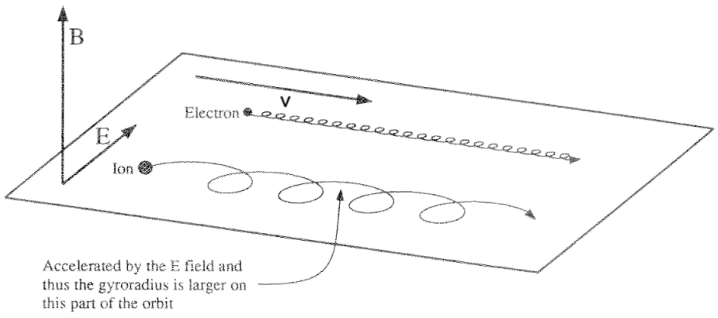

Figure 1.5: $\vec{E} \times \vec{B}$ motion of electrons and ions. (*Kivelson*, 1995)

ion and electron densities that vary from the surrounding plasma. These field aligned structures are essential for HF radar operation, as will be explained in Chapter 2.

1.4 Magnetohydrodynamic Waves

Magnetohydrodynamic (MHD) waves are a class of waves that propagate at relatively low frequencies in a plasma. The two basic types of MHD waves are Alfvén and magnetosonic waves. The dispersion relations for MHD waves can be derived (*Cross*, 1988) using Ampere's and Faraday's laws assuming an ideal, one fluid plasma with zero resistivity. Plane wave solutions are assumed for $\vec{v}$, $\vec{E}$, $\vec{B}$, $\vec{j}$, and ρ of the form $\propto e^{i(k_x x + k_y y + k_z z - wt)}$. The wave frequency ω is assumed to be much smaller than the ion cyclotron frequency $\omega \ll \omega_{ic}$. From these assumptions a dispersion relation can be found,

$$(\omega^2/v_A^2 - k_\parallel^2)(\omega^2/v_A^2 - k^2) = 0\,, \tag{1.8}$$

where $k_\parallel$ is the wave vector parallel to the background magnetic field $\vec{B}$ and k is the magnitude of the wave vector. The Alvén velocity, v_A is given by

$$v_A = \frac{B}{\sqrt{\mu_0 n m_i}}\,, \tag{1.9}$$

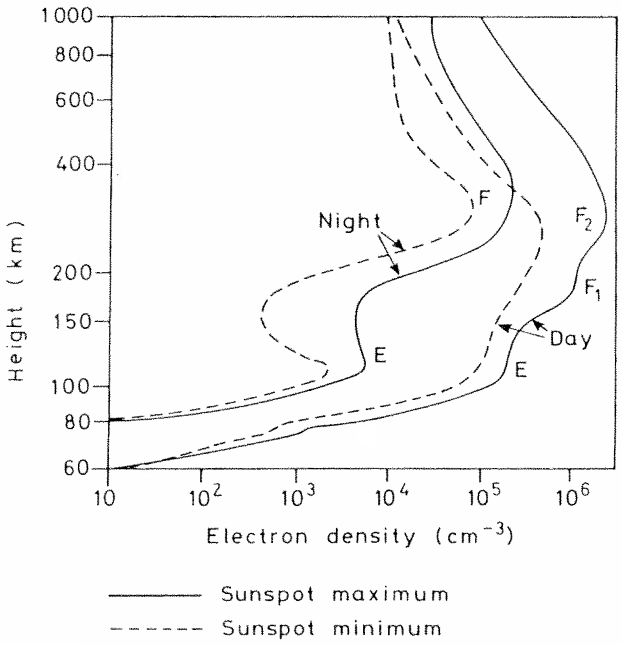

Figure 1.6: Electron density profile of the Earth's ionosphere. Curves are shown for night and day for sunspot minimum and maximum conditions. The E and F regions are clearly marked. Densities peak in the day and during sunspot peaks when ionizing radiation from the sun is at a maximum. Adapted from *Hargreaves* (1992)

where μ_0 is the permeability of free space, n is the electron density, and m_i is the ion mass. The roots of Equation 1.8 are

$$\omega/k_{\|} = v_A \tag{1.10}$$

and

$$\omega/k = v_A\,. \tag{1.11}$$

Equation 1.10 is the dispersion relation for an Alfvén wave. Alfvén waves only travel along magnetic field lines. The magnetic and electric field perturbations are perpendicular to the propagation vector, and therefore, the background field. Equation 1.11 is the dispersion relation for the mag-

netosonic wave. Magnetosonic waves propagate isotropically as a compressional wave with electric and magnetic field components.

1.5 ULF Geomagnetic Oscillations

Ultra-low-frequency (ULF) waves are electromagnetic waves with periods from 0.1 to 600 seconds which are usually recorded as variations on the Earth's magnetic field. These "geomagnetic pulsations" can be recorded at all latitudes and times at the Earth's surface. The presence of geomagnetic pulsations has long been known, but it was during the International Geophysical Year of 1958 that study of ULF waves intensified. This led to magnetometer records from across the globe being gathered and studied for geomagnetic oscillations.

ULF waves have a variety of causes and characteristic behaviours. Following the collection and study of magnetometer records, several classification schemes were proposed. The conventional classification scheme, shown in Table 1.1 makes divisions based on frequency and the duration of pulsation (*Jacobs et al.*, 1964). This scheme was created before the generation and propagation mechanisms for ULF waves were known and instead used morphology to make distinctions. Pulsations were divided into 2 categories based on duration: Irregular pulsations (Pi) which have a duration of 10-20 minutes, and continuous pulsations (Pc) which can last for several hours. These categories were further divided based on period, as shown in Table 1.1. Of interest to this thesis are Pc3 and Pc4 waves. Although these were originally placed in two separate categories, Pc3 and Pc4 waves are now believed to share a common generation and propagation mechanism and are often referred to as a single category, Pc3-4.

Notation	Period Range (sec)
Pc1	0.2 - 5
Pc2	5 - 10
Pc3	10 - 45
Pc4	45 - 150
Pc5	150 - 600
Pi1	1 - 40
Pi2	40 - 150

Table 1.1: Classification of ULF waves (*Jacobs et al.*, 1964)

1.6 Generation and Propagation of Pc3-4 Waves

Pc3-4 waves are generated by the cyclotron motion of solar wind protons reflected from the Earth's bowshock (*Yumoto*, 1985). The generated waves are magnetosonic and pass through the bowshock and into the magnetosphere where they travel in the equatorial plane. As the magnetosonic waves move earthward, they interact with magnetic field lines. This interaction causes transverse motion of the field lines, generating Alfvén waves. These Alfvén waves travel to auroral and cusp latitudes along field lines (*Yumoto et al.*, 1985; *Howard and Menk*, 2001) as shown in Figure 1.7. The time required for Pc3-4 waves to travel from the Earth's bowshock to the ground can be estimated from the Alfvén speed in the magnetosphere and the distance to the bowshock. With the bowshock at $10R_E \approx 60,000km$, and the Alfvén velocity of the order of 1,000 km/s we can estimate that the propagation time, $T_{prop} \approx 1$ minute. This is of the order of a single Pc3-4 period (10s-150s).

After traveling along the field lines to ionospheric heights, Alfvén waves are usually reflected by the high Pedersen conductivity in the E region. If the length of the field line permits, a standing wave can be established on the field line, similar to a transverse wave on a string. The points where the field line meets the E region act as nodes for the wave's electric field. At certain latitudes a field line resonance can be established, enhancing the magnitude of the observed oscillations.

MHD waves are purely a plasma phenomenon and cannot propagate in a neutral atmosphere. For ULF waves to reach the ground a conversion from MHD to electromagnetic propagation must take place. *Hughes* (1974) provided an explanation for how this conversion takes place, and is illustrated in Figure 1.8. Because the Pedersen conductivity in the E region is large the incident wave is reflected. Some part of the incident wave will propagate as an evanascent mode to the ground, but will decay quickly with decreasing altitude due to the skin effect. The Hall conductivity also peaks in the E region and the incident electric field and the background magnetic field will cause an $\vec{E} \times \vec{B}$ drift of electrons. The electron drift creates a current that generates an electromagnetic wave that can propagate to the ground. In the ideal case the ground magnetic field is rotated 90° with respect to that in the incident ULF wave as shown in the figure. The incident magnetic field is attenuated by the ratio of the Hall to Pedersen conductivities in its conversion across the E region.

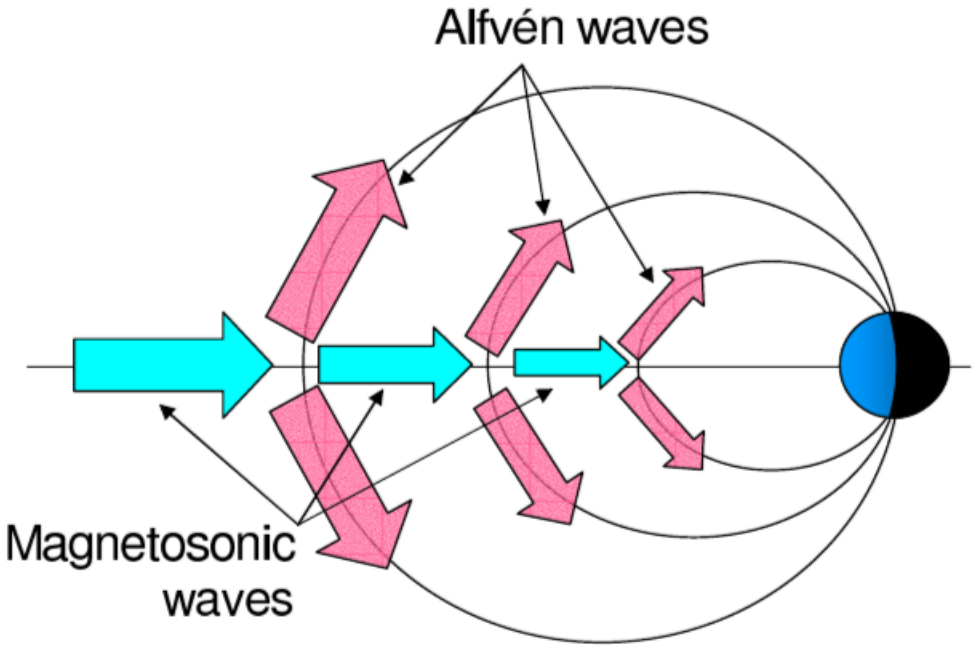

Figure 1.7: Propagation mechanism of Pc3-4 waves from the Earth's bowshock to high latitudes (*Ponomarenko et al.*, 2005)

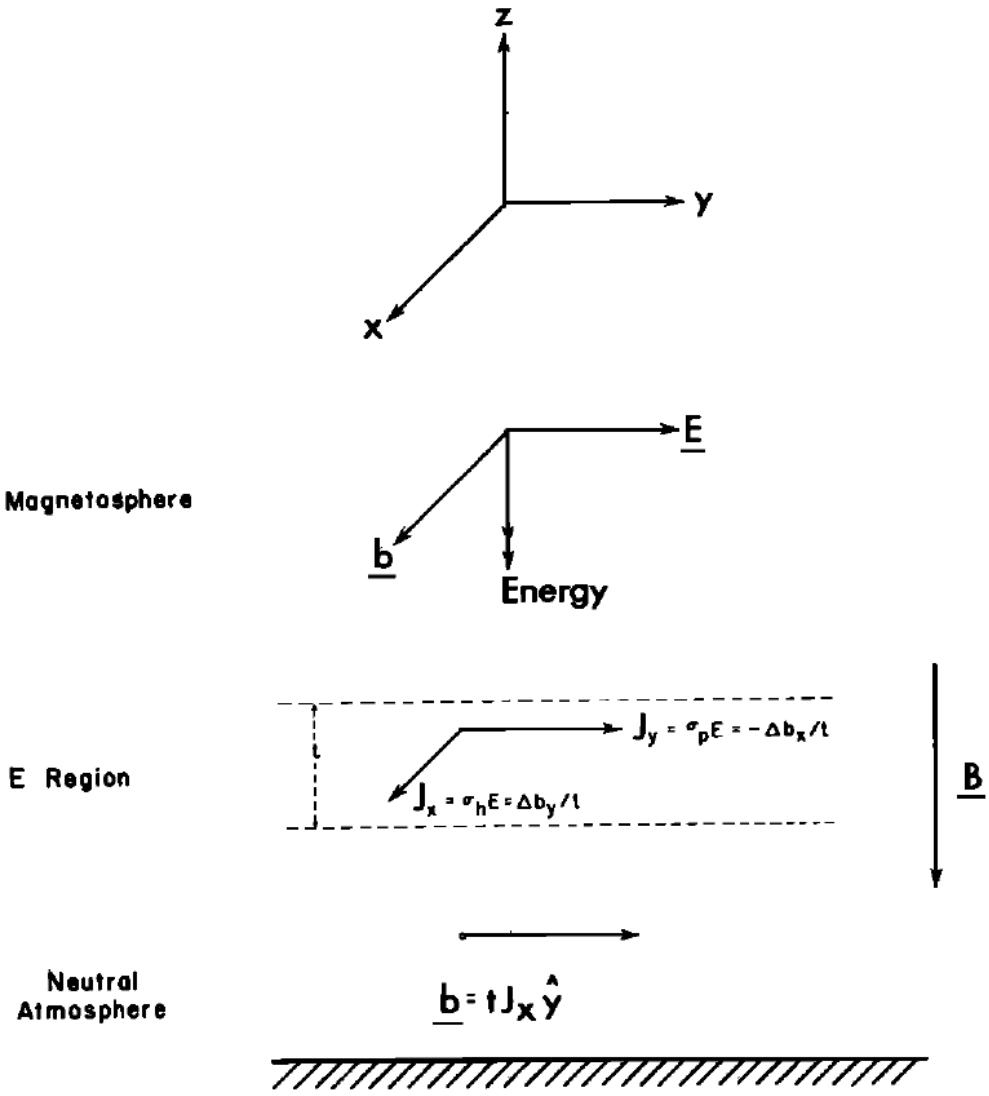

Figure 1.8: The passage of an Alfvén wave in the magnetosphere through the ionosphere to the ground. The Hall current in the E region causes a 90° rotation of the incident magnetic field. (*Hughes and Southwood*, 1976)

1.7 Applications of ULF Waves

The generation and propagation of ULF waves depend on conditions of interplanetary space and the magnetosphere. Changing conditions alter the behaviour of the propagating wave, leaving their signature on the resulting oscillations. A deep understanding of the processes that shape ULF waves would allow us to utilize them as a tool for remote sensing of the magnetosphere (*Gul'elmi*, 1974; *Troitskaya and Gul'Elmi*, 1967; *Fraser*, 2003; *Allan and Poulter*, 1992). However, before this can be reliably implemented, greater understanding of ULF waves and their processes must be obtained. Some of the techniques that have been suggested or implemented to study the magnetosphere are included here.

One technique utilizes the dependence of the conversion of MHD waves in the ionosphere on the height integrated Hall and Pedersen conductivities (*Hughes and Southwood*, 1976). By comparing measurements of ULF waves in the ionosphere and on the ground, an estimate of the conductivities can be obtained (*Allan and Poulter*, 1992).

Another technique links the resonant frequency of a field line with the distribution of mass along the field line (*Fraser et al.*, 2005; *Waters*, 2000). By observing the resonant frequencies of a field line, and using a reasonable model for the magnetic field and variation of mass along the field line, the plasma density can be calculated. This dependence on frequency and ion density can also be exploited to determine the location of the plasmapause (*Waters*, 2000). The Alfvén velocity and resonant frequency reach a maximum at the plasmapause, decreasing with the radial distance to the Earth due to the sharp increase in plasma density. By comparing the phase difference of measurements made at two latitudes, the phase will cross zero at the resonant frequency if the plasmapause is between them.

In contrast to being used as a magnetospheric diagnostic tool, ULF activity can be a hindrance to studies that use magnetic field measurements. Aeromagnetic surveys map the magnetic field on the Earth's surface to determine the location and distribution of minerals below the surface. ULF wave activity can interfere with these surveys (*Vallée et al.*, 2007). Strong Pc3 activity can cause surveys to be rejected, forcing crews to resurvey an area or causing the grounding of aeromagnetic aircraft until conditions improve, resulting in downtime. Improving our understanding of Pc3 activity can lead to more efficient planning and better cost estimation of these surveys.

1.8 Pc3-4 Waves at Auroral Latitudes

Pc3-4 waves have been extensively studied within the closed field line region. They are principally a day-side phenomenon, with a peak in power being observed pre-noon at 10:30-11:00 MLT (*Ponomarenko et al.*, 2002), although they have recently been observed on the nightside (*Ponomarenko et al.*, 2010b). Peaks in power occur at auroral latitudes (*Fraser-Smith*, 1982).

Usually ULF spectra in the Pc3-4 range consist of two components, a band-limited enhancement found at 10-50 mHz which is produced by the upstream generation mechanism at the bowshock and a power-law background proportional to f^{-4} (*Ponomarenko et al.*, 2002). A typical spectrum is shown in Figure 1.9. The center frequency of the band limited enhancement is related theoretically to the IMF magnitude B_{IMF} and cone angle θ_{xB} (*Takahashi et al.*, 1984) by

$$f(mHz) = 7.6 \cos^2 \theta_{xB} |B_{IMF}|(nT)\,. \tag{1.12}$$

This relationship has been verified experimentally by *Ponomarenko et al.* (2002) who found the relation between frequency measured on the ground and IMF strength to be

$$f(mHz) \approx 4.4 |B_{IMf}|(nT) \tag{1.13}$$

for an effective average cone angle of 40°. Cone angle also affects the power of oscillations, with maximum power observed for cone angles of $\theta \approx \pm 30°$ (*Ponomarenko et al.*, 2002).

Howard and Menk (2001) found the spatial coherence of Pc3-4 waves on closed field lines at cusp latitudes to be of the order of thousands of kilometers, with the amplitude of waves decreasing towards the equator. Comparing the magnetic field from stations covering a wide range of latitudes, shown in Figure 1.10(a), we can see simultaneous oscillations in the magnetic meridional component. By comparing activity between stations a coherence length was estimated. Figure 1.10(b) shows the cross power, coherence and phase of the oscillations for two stations SORH and KILH. We can see high coherence from 20-30 mHz. The phase of the coherence between stations shows poleward propagation of the oscillations. This propagation is consistent with the propagation theory of *Yumoto et al.* (1985): oscillations at a higher latitude must travel longer along field lines before reaching the ionosphere, resulting in apparent poleward propagation.

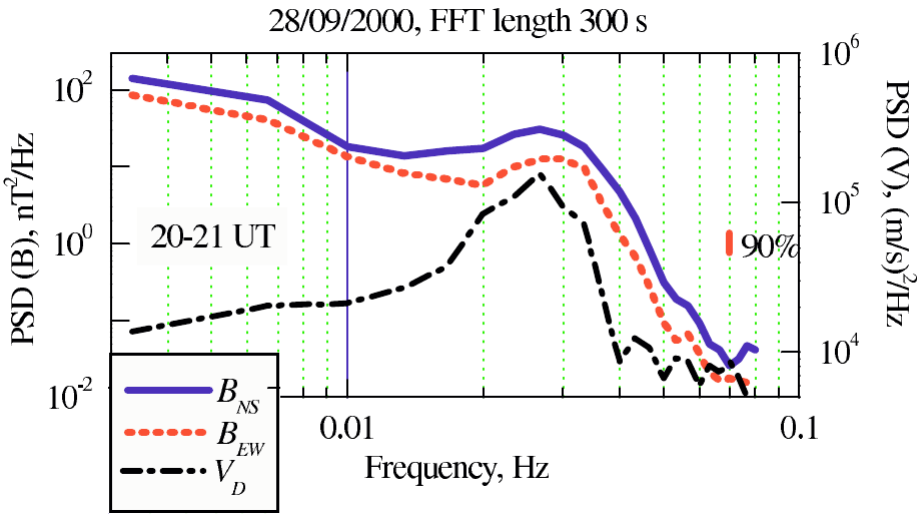

Figure 1.9: Spectrum of Pc3-4 waves seen at mid latitudes. The magnetic field spectra are shown in blue and red. Spectrum found using radar is shown in black. The spectra consist of a flat power law background, with a band limited enhancement at 10-50 mHz. Adapted from *Ponomarenko et al.* (2005)

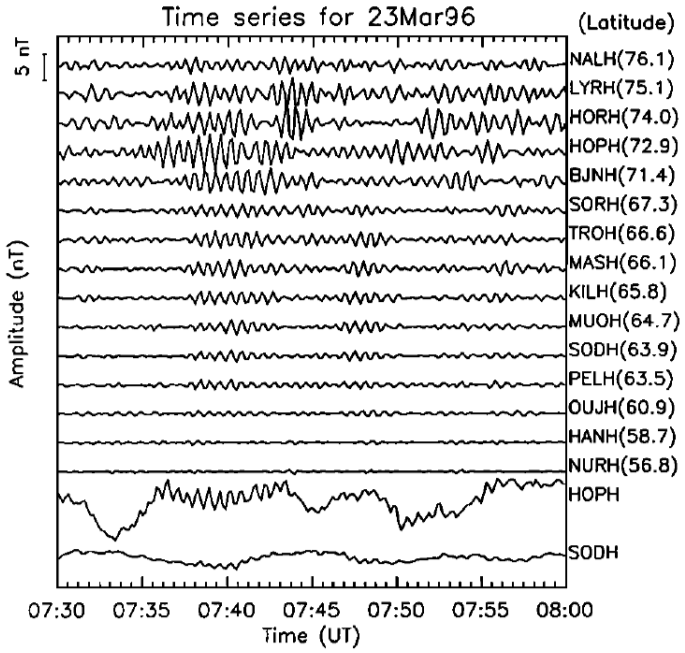

(a)

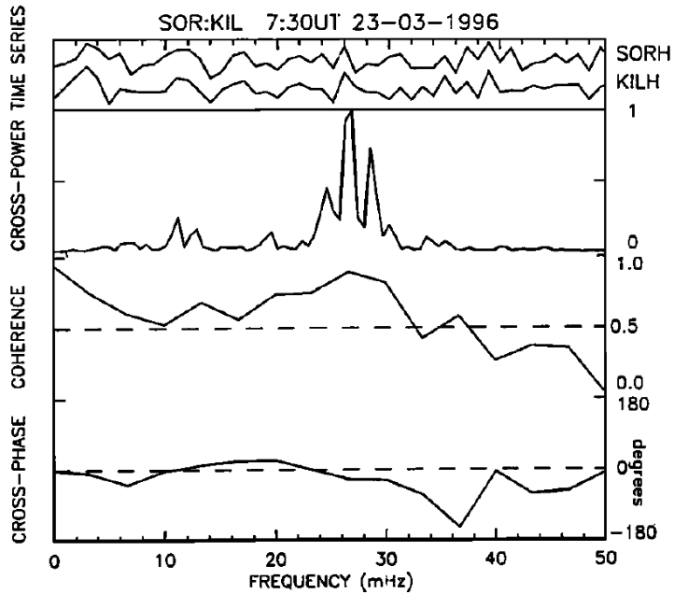

(b)

Figure 1.10: (a)Simultaneous oscillations observed at multiple ground stations. Traces for two stations are shown in the bottom two plots before detrending was applied. (b) The cross power and coherence between two of the stations. Good coherence is observed at 20-30 mHz (*Howard and Menk*, 2001).

1.9 ULF waves in the Polar Cap regions

The presence of Pc3-4 waves in the Earth's polar caps is puzzling. In the accepted propagation model (*Yumoto et al.*, 1985) Pc3-4 waves propagate as Alfvén waves along closed field lines to high latitudes, but there is no known mechanism for Pc3-4 waves to travel from the bowshock to the open field line regions in the polar caps. Despite this, Pc3-4 waves are commonly recorded using ground-based magnetometers in the polar cap region (*Fraser-Smith*, 1982; *Villante et al.*, 2000; *De Lauretis et al.*, 2005; *Villante et al.*, 2006; *Francia et al.*, 2009). Studies have been mainly limited to Antarctic stations by the coverage of magnetometers, with no studies conducted in the northern polar cap due to the absense of a substantial landmass to support ground-based measurements.

Some mechanisms for Pc3-4 propagation to open field line regions have been suggested (*Engebretson et al.*, 2006). One such mechanism suggests that magnetosonic waves propagate along the magnetosheath to the open field line region where Alfvén waves are then excited. Another mechanism suggests that there is an unknown non-MHD process that carries oscillations from the bowshock to the tail lobe lines, at which point there is a conversion into an Alfvén wave. There is currently no evidence that supports either of these hypotheses.

De Lauretis et al. (2005) analyzed pulsations at Antarctic station Terra Nova Bay (80° S MLAT) and at Dome C (89° S MLAT). A simultaneous pulsation event at both stations is shown in Figure 1.11. The pulsations were found to have similar spectral features as those found by *Ponomarenko et al.* (2002) at lower latitudes. The study shows the presence of a band-limited component whose center frequency is proportional to B_{IMF} at both stations. The slope of center frequency vs B_{IMF} agrees with lower latitude studies.

Villante et al. (2000, 2006) studied oscillations in the southern polar cap at the same stations. At Terra Nova Bay a diurnal Pc3-4 power trend with a noontime peak in Pc3-4 power was found similar to that at lower latitudes, but no diurnal trend was observed deeper in the polar cap at Dome C. They also found correlation between pulsation power and IMF magnitude, orientation, and solar wind speed being stronger than those found at lower latitudes.

Chugunova et al. (2006) searched for diurnal variations in Pc3-4 pulsations at multiple stations across a range of Antarctic latitudes. They found very inconsistent diurnal trends which differ considerably from station to station. This discrepancy may be due to the use of a new statistical technique introduced in the same paper. This technique relies heavily on statistical analysis of spectral features. While the results are contradictory, they do highlight the problems with applying

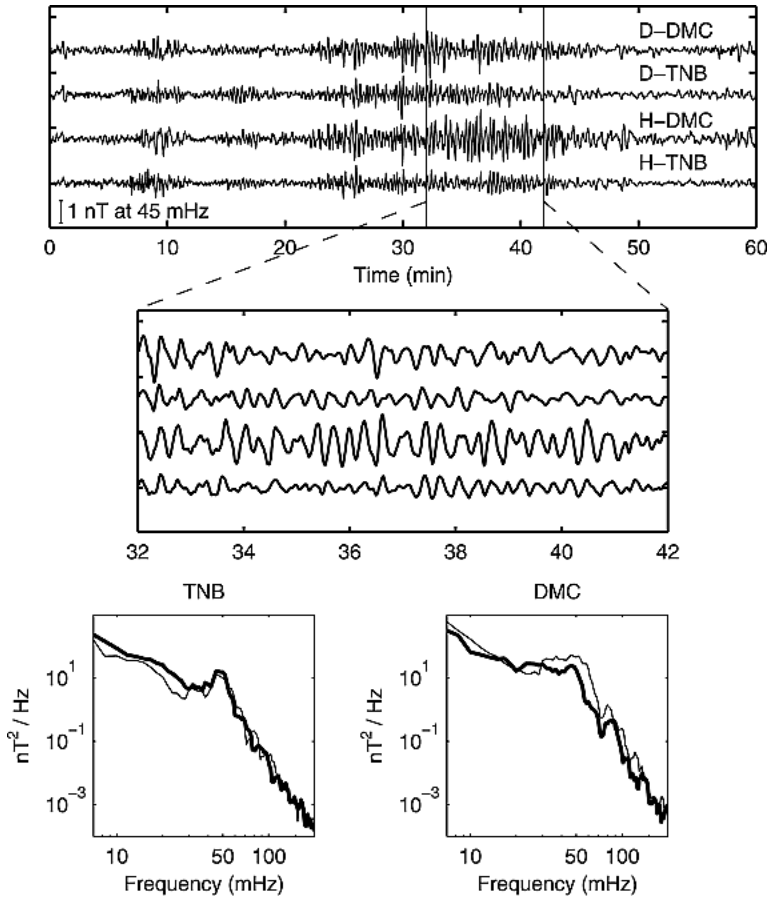

Figure 1.11: Occurrence of simultaneous Pc3-4 oscillations at Terra Nova Bay and Dome C (*De Lauretis et al.*, 2005). Spectral features are similar to those found by *Ponomarenko et al.* (2002) at lower latitudes.

geomagnetic coordinates and magnetic local time to high polar cap latitudes where closely located field lines can map to vastly different regions in the magnetosphere. Adding to the controversy, *Chugunova et al.* (2007) found that Pc3 and Pc4 bands exhibited different dependence on the solar wind cone and clock angle $\tan^{-1} \frac{B_y}{B_z}$. They concluded that the activity in the two frequency bands must be generated by different processes.

While HF radars have been used to study Pc3-4 waves in the closed field line region, no studies have yet used radar to study Pc3-4 waves in the polar cap. HF radar can observe Pc3-4 waves before they are transmitted to the ground where their signatures are distorted by transmission through the ionosphere. SuperDARN observations can provide a spatial view of Pc3-4 waves in a region where magnetometer coverage is sparse or absent. In this work I use the PolarDARN stations at Rankin Inlet (72.6° N MLAT) and Inuvik (71.5° N MLAT) to observe oscillations at Pc3-4 periods in the polar cap ionosphere in order to shed light on their properties.

Chapter 2

Instruments

In our study of Pc3-4 wave activity we use HF radar to make observations in the polar cap ionosphere. As described in the previous section, ULF waves propagate through the ionosphere to the ground where they can be detected by ground-based magnetometers. Because the majority of ULF wave studies have used magnetometers we will compare our observations made with radar against magnetometer records.

In this section I will describe the general principles behind the HF radar and flux-gate magnetometers used in this study and how they are applicable to the study of ULF waves. The HF radars and magnetometers used are part of the SuperDARN radar network and CARISMA magnetometer array, respectively. These networks will also be discussed.

2.1 Principles of HF Radar

HF radar can be used to study the ionosphere at high latitudes by measuring the Doppler shift of signals that are scattered from plasma irregularities in the E and F regions of the ionosphere. We consider the case where the transmitting and receiving station are at the same location. It is believed that the irregularities are aligned with the magnetic field. For the scattered signal to be received at the transmission station the electromagnetic wave propagation direction will be perpendicular to the magnetic field aligned structures (*Greenwald et al.*, 1995). At high latitudes, the magnetic field orientation approaches the vertical direction. In order to achieve this orthogonality, refraction of HF electromagnetic waves in a plasma is utilized.

In ionospheric plasmas, the index of refraction in ionospheric plasmas is given as

$$n^2 = 1 - \frac{{f_n}^2}{f^2}\,, \tag{2.1}$$

where f is the frequency of the propagating electromagnetic wave and f_n is the plasma frequency,

given by

$$f_n = \frac{1}{2\pi}\sqrt{\frac{Ne^2}{\epsilon_0 m_e}}, \tag{2.2}$$

where N is the electron density, e is the charge on an electron, and m_e is the electron mass. Equation 2.1 requires the assumption that the electromagnetic wave has a much greater frequency than the electron gyro-frequency and collision frequency. From Equation 2.1 we can see that for any frequency, $n < 1$. If the index of refraction is less than unity an electromagnetic wave obliquely incident on the ionosphere from the neutral atmosphere ($n = 1$) will bend downwards. It is this bending that allows rays to achieve orthogonality with the magnetic field lines. For an F region plasma we have a plasma frequency of approximately 5 MHz. HF radars signals with a frequency of 10-15 MHz will have strong bending. Rays at higher frequencies in the VHF-UHF band ($f > 30$ MHz) will have an index of refraction that approaches unity, and will not experience this bending, and will propagate in approximately straight lines.

Several types of propagation are possible depending on the frequency of the transmitted signal and the angle of incidence, ϕ_0, on the ionosphere. The ray tracing diagram in 2.1 shows three possible types of propagation. The first type are escaping rays, which will reach an altitude where the electron density is at a maximum. The rays pass through the ionosphere and will not be deflected back towards the Earth if $f \cos\phi_0 > f_p$. In the diagram the peak electron density is indicated by the dashed line at 300 km. As the angle of incidence increases (or the elevation angle from the ground station decreases), the ray path will be directed past the horizontal towards the ground. These rays no longer escape from the Earth's atmosphere. As can be seen in the figure, the path length that the ray travels to the ground decreases with elevation angle and the rays will encounter the surface of the Earth closer to the base station. These rays are known as Pedersen rays (*Davies*, 1990). The range will decrease with elevation angle until the ray path reaches its minimum range at the end of the skip zone, shown in the figure at 900 km. After this, low angle rays propagate with the range increasing with decreasing elevation angle.

At the bottom of the ionospheric layer, the electron density increases with height so that the rays continue to bend as altitude increases. Ionospheric scatter (IS) occurs when the transmitted wave-vector bends enough to become orthogonal to the geomagnetic field and there are field aligned structures in the ionosphere. When this happens some fraction of the wave's energy is scattered back to the transmission station. This contrasts with so-called ground scatter (GS), which occurs when the unscattered wave reaches the ground and is scattered by the rough ground surface. The rays

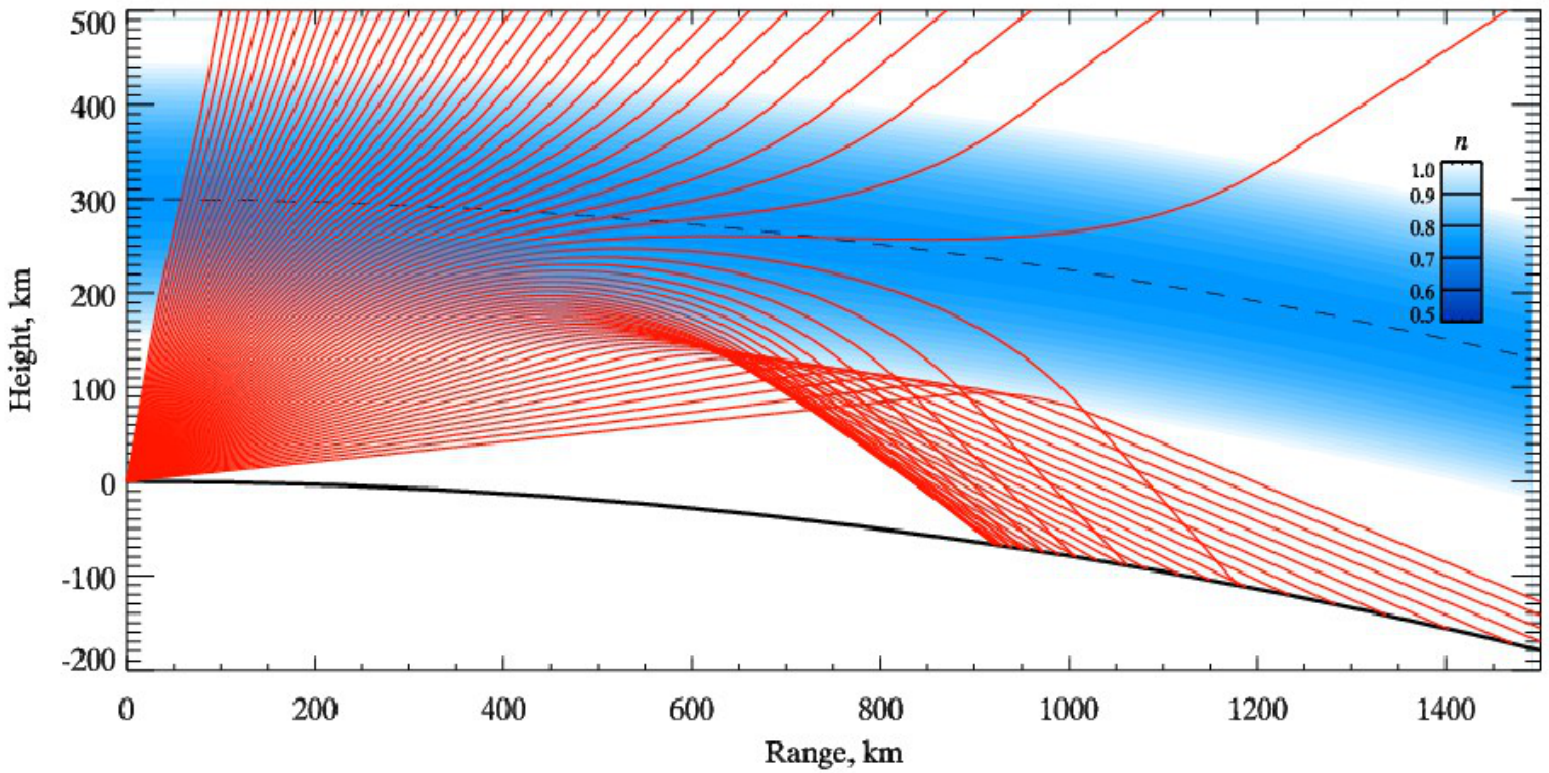

Figure 2.1: Ray tracing diagram of HF radar for a parabolic ionosphere. Escaping, Pedersen and low-angle rays can be seen. The shading indicates the index of refraction for various altitudes. The dashed line at 300 km indicates the peak electron density. Courtesy of P.V. Ponomarenko

that meet the Earth's surface can be reflected further from the transmission station, repeating this process in their propagation through the ionosphere (multiple hop propagation), or if the ground terrain provides a suitable structure a part of the scattered signal will retrace it's path through the ionosphere back to the ground station. Water waves and mountains have a suitable shape and are believed to be the strongest contributors to ground scatter (*Ponomarenko et al.*, 2010a).

The Doppler shift of a wave that travels through a plasma is caused by a change in the phase path length with time. The Doppler shift is derived (*Ponomarenko et al.*, 2009) from

$$\Delta\omega_{AB} = -k_0 \frac{\partial L}{\partial t}\,, \tag{2.3}$$

where k_0 is the free space wavenumber and L is the phase path length of the wave, given as

$$L = \int_A^B n ds\,, \tag{2.4}$$

where A and B are the locations where the signal is transmitted and received, respectively. n is the index of refraction, and ds is an element of the signal's path. The Doppler shift is then

$$\Delta\omega_{AB} = -k_0 \left[\int_A^B \frac{\partial n}{\partial t} ds + \frac{\partial B}{\partial t} n(B) - \frac{\partial A}{\partial t} n(A) \right]. \tag{2.5}$$

For our purpose the transmitting and receiving station are at the same location A, and the wave is scattered by a target located at B. The Doppler shift must then be doubled to account for the return journey as well. The Doppler shift of the second and third terms are caused by the line of sight motion of the transmission station or the target. However, the transmission station is usually motionless, so $\frac{\partial A}{\partial t} = 0$. The first term is integrated over the path length of the ray and is not associated with the motion of a single point. We can explore the meaning of this integral term by taking the time derivative of the index of refraction given by Equation 2.1

$$\frac{\partial n}{\partial t} = \frac{-e^2}{8\pi^2 \epsilon_0 m_e n f^2} \frac{\partial N}{\partial t}\,. \tag{2.6}$$

For rays that are reflected to the ground we assume that the vertical gradient in electron density

plays a dominant role (*Bourdillon et al.*, 1989), namely, $\vec{\nabla} \cdot (N\vec{v}) \approx v_z \frac{\partial N}{\partial z}$. The continuity equation

$$\frac{\partial N}{\partial t} = -\vec{\nabla} \cdot (N\vec{v}) \tag{2.7}$$

then reduces to

$$\frac{\partial N}{\partial t} \approx -v_z \frac{\partial N}{\partial z}\,. \tag{2.8}$$

Substituting Equations 2.6 and 2.8 into Equation 2.5 and ignoring the contributions from the motion of A and B we obtain

$$\Delta f_{AB} = -\frac{k_0 e^2}{16\pi^3 \epsilon_0 m_e f^2} \int_A^B \frac{v_z}{n} \frac{\partial N}{\partial z} ds\,. \tag{2.9}$$

We can see the Doppler shift associated with this term is caused by the vertical motion v_z of the ionosphere over the path of the ray.

In the case of ionospheric scatter, the motion of the field aligned structures at B dominates over the integral term in Equation 2.5. Contributions from the integral are neglected and Doppler shifts are assumed to be caused entirely by the motion at B. However, when considering ground scatter the target B is the ground surface and is either slow-moving (water waves) or motionless (ground). The Doppler shift of ground scatter is then caused entirely by the integral of the ionosphere's vertical motion as shown in Equation 2.9.

2.2 SuperDARN HF Radar Network

The Super Dual Auroral Radar Network (SuperDARN) is used to study ionospheric plasma circulation at high latitudes. It consists of more than 30 HF (8-18 MHz) stations across the northern and southern hemispheres. These radars use HF backscatter to detect the motion of E and F region ionospheric plasmas. By combining the line-of-sight measurements of ionospheric velocity from multiple stations, a global view of horizontal ionospheric plasma circulation can be obtained (*Greenwald et al.*, 1995). The usefulness of SuperDARN is not limited to studies of convection. SuperDARN has been successful in studying a broad range of phenomena including ionospheric convection, field-aligned currents, magnetic reconnection, substorms, ULF waves, gravity waves, mesospheric winds, polar mesosphere summer echoes and E region irregularities (*Chisham et al.*, 2007).

SuperDARN operates by transmitting a sequence of 7 or 8 pulses separated by a number of

unique time lags. Transmitted pulses normally have a length of 300 μs. By sampling the returning signal and comparing to the transmitted signal, the distance (group range) to the echoes can be determined. Each range gate covers 45 km in range, which represents the spatial resolution provided by a 300 μs pulse length. For each range gate, a complex auto-correlation function (ACF) is calculated from the received signal. The slope of the ACF phase is assumed to be linear with the time lag. The Doppler frequency is calculated from the slope of the phase. The Doppler velocity is then found from

$$v_D = \frac{-f_D \lambda_0}{2n}\,, \tag{2.10}$$

where λ_0 is the wavelength of the transmitted signal and n is the index of refraction of the scattering point which is currently assumed to be 1 in the SuperDARN data processing.

As shown in Figure 2.2, the ideal ACF looks like a decaying sinusoid. An exponential or Gaussian decay curve is fitted to the ACF power, and the spectral width is determined from the decay constant of the fitted curve (*Ponomarenko and Waters*, 2006). Connecting this with a physical process, the spectral width is determined by the lifetime of the structures causing scattering. The spectral width of ground scatter is usually very small compared to ionospheric scatter because the scattering structures on the ground change very slowly (ocean waves) or not at all (ground). In addition to low spectral width, ground scatter also has low Doppler velocities. Based on the empirical information above, ground scatter is identified by SuperDARN data processing by the empirical criterion

$$g = |v| - (v_{max} - (v_{max}/\omega_{max}) * |\omega|) < 0\,, \tag{2.11}$$

where v is the Doppler velocity and ω is the spectral width. The maximum Doppler velocity and spectral width in this equation are 30 m/s and 90 m/s respectively. This criterion is not 100% accurate; some signals can be misidentified as ground scatter instead of ionospheric scatter and vice-versa.

PolarDARN is an extension of the SuperDARN HF radar network to latitudes which are higher than those of conventional SuperDARN radars. This enables the study of plasma motions in the polar cap. PolarDARN consists of three HF radars in the Northern polar cap at Rankin Inlet, Inuvik and most recently, Clyde River. There are also three polar cap radars in Antarctica. This work uses the PolarDARN stations at Inuvik and Rankin Inlet. Auroral latitude radars at Saskatoon and Prince George were used to compare polar cap results with auroral latitudes. The locations and fields of view of the HF radars used in this work are shown in Table 2.1 and Figure 2.3. A single

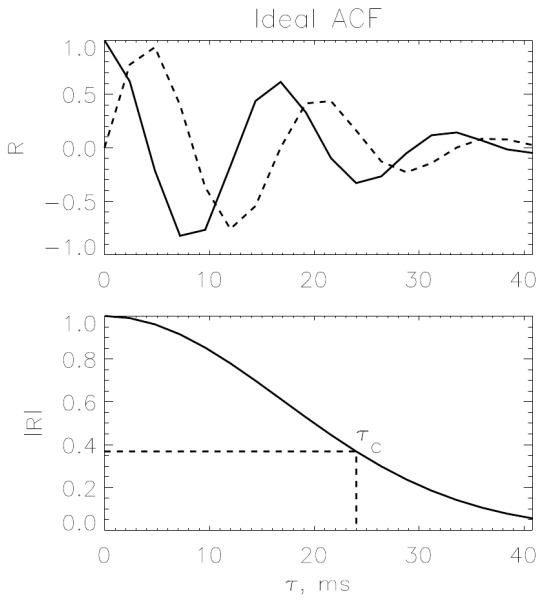

Figure 2.2: The ideal auto-correlation function of a SuperDARN signal. The real and imaginary components are shown as the solid and dashed lines respectively in the top figure. The absolute value is shown in the bottom figure. The decay constant τ_c shown is used to determine the spectral width. Long correlation times (as is the case for ground scatter) correspond to low spectral widths. From *Ponomarenko and Waters* (2006)

SuperDARN radar typically covers 54° in azimuth with 16 beams. Each beam has a width of ≈ 3.5°.

2.3 Magnetometers

The two main types of research magnetometers are induction and fluxgate. An induction magnetometer consists of a coil of wire. The EMF induced in the coil is given by

$$\epsilon = -AN\frac{dB_n}{dt}\,, \tag{2.12}$$

where A is the cross sectional area of the coil, B_n is the magnetic field perpendicular to the plane of the coil, and N is the number of loops in the coil. By measuring the voltage across the coil,

Station	Geographic		Geomagnetic	
	lat [°]	long [°]	lat [°]	long [°]
Rankin Inlet	62.82	93.11	72.6	26.4
Inuvik	68.42	133.5	71.5	85.1
Saskatoon	52.16	106.53	60.9	43.8
Prince George	53.98	122.59	59.6	64.3

Table 2.1: SuperDARN locations

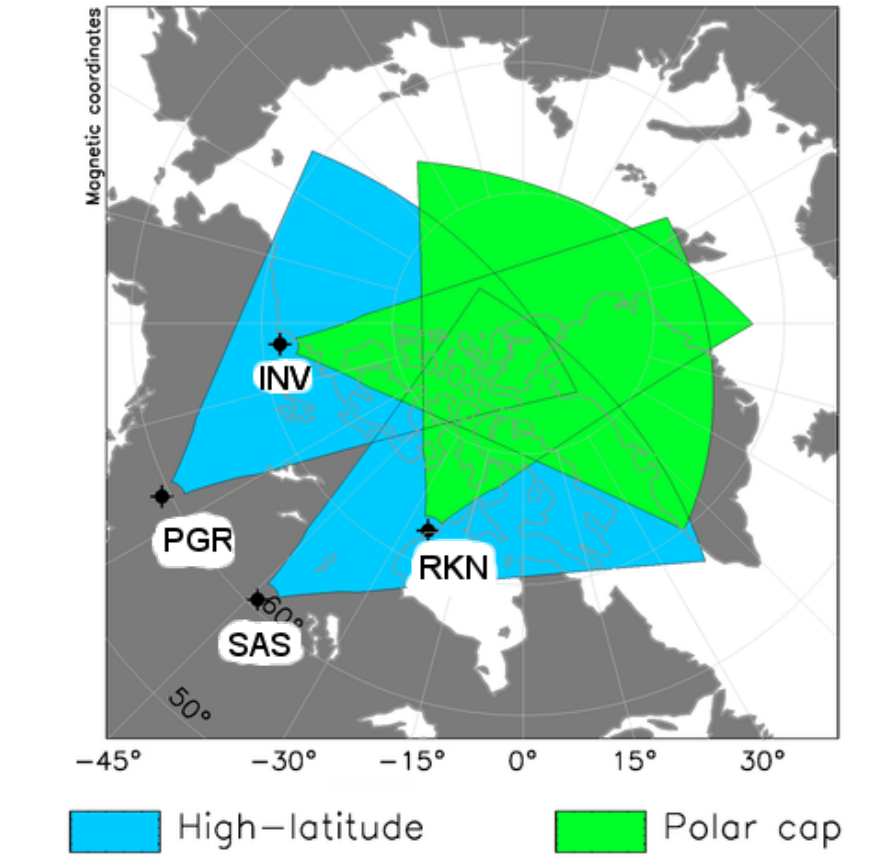

Figure 2.3: Location and fields of view of Rankin Inlet and Inuvik PolarDARN radar are shown in green. Saskatoon and Prince George can be seen at lower latitudes in blue.

the rate of change of the normal magnetic field strength with time can be determined. The main drawback to induction coil magnetometers is that the signal amplitude is proportional to frequency, accentuating high frequency variations and distorting the signal.

This work uses fluxgate magnetometers, which do not have the frequency dependence limitations of induction coil magnetometers. The principles of fluxgate magnetometers are as follows (see *Kaufman et al.* (2009)). A loop of wire has a sinusoidal current passed through it so that the magnetic field generated by the circuit is

$$B_c(t) = p\sin(\omega t)\,, \tag{2.13}$$

where p is the amplitude of the generated magnetic field, ω is the angular frequency, and t is time. With the addition of a background magnetic field, such as the Earth's magnetic field B_e, the total field becomes

$$B_0(t) = B_e + p\sin(\omega t)\,. \tag{2.14}$$

If a ferromagetic material is placed in a changing external magnetic field, the magnetic field inside the core will follow a saturation curve as shown in Figure 2.4. The three curves in the diagram are caused by hysteresis effects. In the figure, curve 1 begins with an unmagnetized core and the external magnetic field at $B = 0$. The magnetic field of the core follows the external magnetic field but approaches a maximum value. This is known as saturation. If the magnetic field is then decreased (curve 2) the core's magnetic field will not return along curve 1 due to the magnetization of the ferromagnetic core. This hysteresis effect gives us curves 2 and 3 as the external magnetic field oscillates.

For a fluxgate magnetometer, the core is chosen so that hysteresis effects will be minimal: that is, curves 1,2 and 3 will almost overlap. If a ferromagnetic core is placed inside the current driven loop described previously, the resulting magnetic field in the core will be given by a third order approximation as

$$B = (aB_0 - bB_0^3)\,, \tag{2.15}$$

where B is the magnetic field in the core and a and b are parameters of the saturation curve determined by the material of the core. The second order term is neglected because the saturation curve is an odd function. Putting Equations 2.14 and 2.15 together we get

$$B(t) = (B_e + p\sin(\omega t))[a - b(B_e^2 + 2B_e p\sin(\omega t) + p^2\sin^2(\omega t)]\,. \tag{2.16}$$

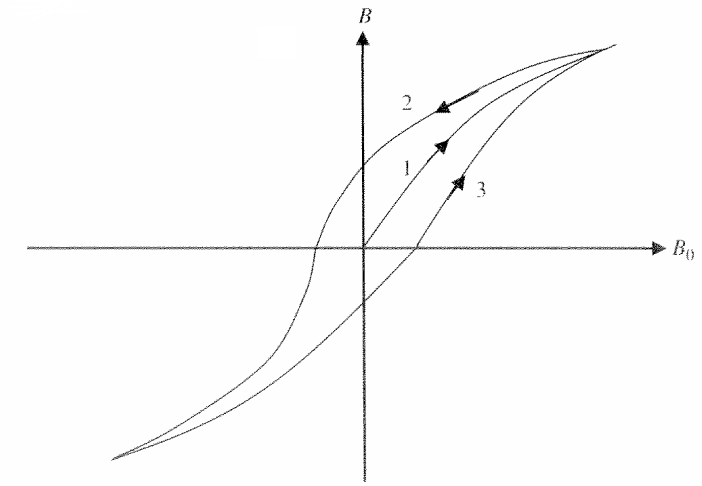

Figure 2.4: Saturation curve of the magnetic field in a ferromagnetic material (B) and an external magnetic field. Curves 1, 2 and 3 represent different portions of the hysteresis curve, as described in the text. (*Kaufman et al.*, 2009)

Around the initial loop we place a sensing loop where the EMF is measured. The EMF in the sensing loop given by

$$\epsilon = -AN\frac{dB}{dt} \tag{2.17}$$

which gives us

$$\epsilon = -NA[p\omega(a - 3bB_e^2)\cos(\omega t) - 3B_e p^2 \omega b \sin(2\omega t) + \frac{3}{4}bp^3\omega\cos(3\omega t)]\,. \tag{2.18}$$

If we can measure the second term of Equation 2.18, a measurement proportional to B_e can be obtained. A flux gate magnetometer is a device to measure the second term. Figure 2.5 shows diagrams of fluxgate devices. The configuration on the left consists of two ferromagnetic cylinders, each wrapped in opposite directions and connected to the same AC source. A single sensing coil is wrapped around the two cores. The configuration on the right consists of a wrapped toroidal core. Two sensing coils are wrapped on opposite sides of the core and the EMF in each of these coils is then added. Because the cores are wound in opposite directions, the sign of p is opposite for

each core. The first and third term depend on odd powers of p. These terms therefore cancel when adding the emf caused by the 2 coils. The second term is proportional to p^2 so that superposition of the coils' emf doubles this term. If we know the saturation curve of the magnetic cores, the magnetic field generated by the driving current, and the physical dimensions of the sensing coil we can determine B_e from the second term in equation 2.18. This device can therefore be used to measure a background magnetic field.

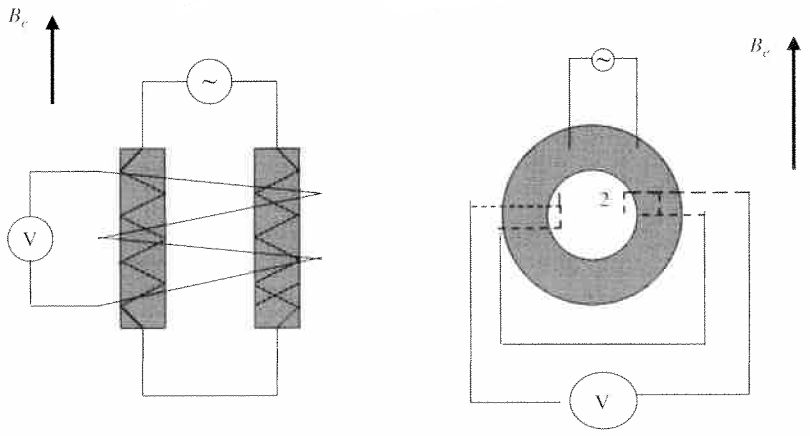

Figure 2.5: Schematics of two different fluxgate magnetometers. The configuration on the left uses two cores and a single sensing coil that measure the sum of their magnetic fields. The configuration on the right uses two sensing coils on opposite sides of a wound torus. The EMF in each coil is then added. (*Kaufman et al.*, 2009)

2.4 CARISMA Magnetometer Array

The Canadian Array for Realtime InvestigationS of Magnetic Activity (CARISMA) magnetometer network consists of 28 fluxgate and induction magnetometers stationed across Canada, Alaska, and the Northern United States.

Each station measures x, y, and z components of the magnetic field: x corresponding to East-West, y corresponding to North-South, and z to the vertical direction at each station. The fluxgate magnetometers are sampled at 8 Hz. The data is then low-pass filtered and resampled at 1 Hz.

The sensitivity of 0.025 nT (*Mann et al.*, 2008) for flux gate magnetometers is well suited to ULF wave studies, where amplitudes observed on the ground are typically >0.1 nT.

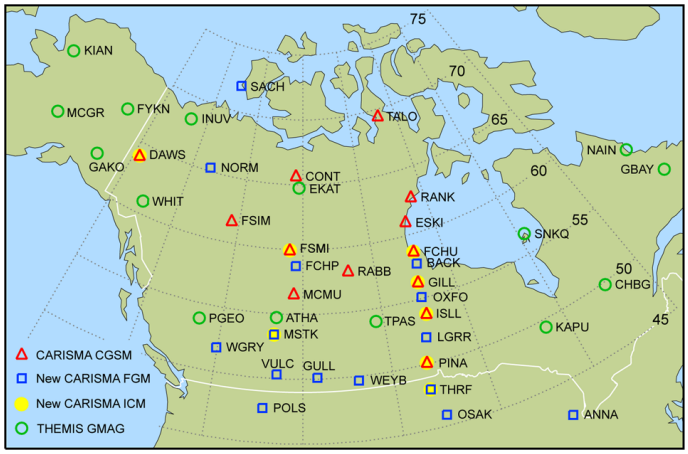

Figure 2.6: Carisma magnetometer array (*Mann et al.*, 2008)

Magnetometers can give a spatially integrated view of the ionospheric currents within a ≈200 km wide area above them. Variations seen with magnetometers can be compared with radar observations if the scattering region is approximately above the magnetometer.

The magnetometers used in this work and their locations are shown in Table 2.2 and Figure 2.6.

Station	CGM lat [°]	CGM long [°]	L
Taloyoak	78.28	330.93	N/A
Gillam	66.03	330.05	6.15
Rabbit Lake	66.85	319.11	6.57
Fort Simpson	67.23	294.29	6.78

Table 2.2: CARISMA magnetometer locations (*Mann et al.*, 2008)

2.5 Data Sets

In the conventional mode, all 16 SuperDARN beams are sampled consecutively at a 3.5 second rate so that each beam is sampled every minute, giving a Nyquist frequency of 8.33 mHz. The Pc3-4 range extends from 6.7 to 100 mHz and special modes are therefore required to study Pc3-4 studies. The THEMIS mode of operation provides a higher temporal resolution than the conventional mode by sampling a particular beam every second sample. The pattern for sampled beams follows 1, 7, 2, 7, 3, 7... . This gives a sampling time of 6 seconds for the THEMIS beam and a Nyquist frequency

of 83 mHz, which is more appropriate for ULF wave study. The high resolution beam for THEMIS mode is selected as the beam that looks North along a single magnetic meridian.

THEMIS modes provide a high temporal resolution on a single beam. In order to determine the spatial characteristics of Pc3-4 waves in the polar cap we designed a special ULF mode which was used to obtain a spatial picture of ULF wave activity. These scans would sample 3 beams only, one after the other, which gives a sampling time of 9 seconds per beam and a Nyquist frequency of 56 mHz. With this ULF mode we could compare activity between beams, giving us a side-to-side perspective instead of being restricted to looking along the line of sight of a single beam. The spatial separation between beams varied. Initially beams 0, 4 and 8 at Rankin Inlet and 8, 12 and 15 at Inuvik were selected. This spread was later narrowed to beams 5, 7 and 8 to obtain better spatial resolution. The date and station of THEMIS and ULF mode SuperDARN scans that were used in this work are listed in Appendix A.

CARISMA magnetometer data from Taloyoak were used for May to August 2008, with 23 days excluded due to disturbed conditions. These days are listed in Appendix B. These data were used to determine a diurnal trend in ULF wave power as observed in the magnetic field on the ground.

Specific events observed using the SuperDARN radar stations were compared to CARISMA magnetometers at Taloyoak, Gillam, Rabbit Lake and Fort Simpson. These events are discussed more in Chapter 3

Chapter 3

Analysis

Ponomarenko et al. (2003) presented a procedure for observing ULF waves in SuperDARN data. Their demonstation used a mid-latitude radar located in Tasmania, Australia (54.8° S, 133.2 E° CGM) sampled at 12 s resolution.

The technique used to visualize ULF signatures is demonstrated in Figure 3.1. Doppler velocity was plotted in grey scale using range-time format. Figure 3.1(a) shows Doppler velocity data when plotted in grey scale with limits of ±500 m/s, which are common limits for plotting Doppler velocity. The presence of ground scatter dominates most of the plot, characterized by the grey color indicative of small velocities and identified by spectral width (not shown). Ionospheric scatter is also present, indicated by large velocities from 7:00-10:00 UT along range gates 40-60 and 11:00-15:30 UT in range gates 15-40. There is very little evidence of oscillations in this figure. However, by imposing plotting limits of ±10 m/s to the range of velocities, variations with small amplitudes that center around 0 m/s can be observed as shown in Figure 3.1(b). Oscillations can now be easily observed along range gates 20-50 from 10:00-11:00 UT. By detrending the data, oscillations that are offset from 0 m/s can be viewed. This is shown in Figure 3.1(c), which shows data that have been detrended with a 10 minute boxcar window. Oscillations can now be observed from 7:00-14:00 UT in both ground and ionospheric scatter.

The radar observations were compared to the induction magnetometer at the nearby Macquarie Island. A single time series was obtained for the radar data by averaging over range gates 24-34 from 9:00-10:00 UT. This is justified by the high coherence observed across these range gates. The data from the induction magnetometer was integrated with time to obtain the magnetic field strength of both the NS and EW components (not shown). The oscillations seen in Doppler velocity were very similar to the oscillations seen in the NS magnetic field with similar maxima observed in their spectra at 2.22 mHz and 3.16 mHz: Pc5 frequencies. This agreement indicates that the velocity oscillations observed by the radar were caused by ULF geomagnetic oscillations.

In *Ponomarenko et al.* (2005) this technique was expanded to Pc3-4 waves. Using the same

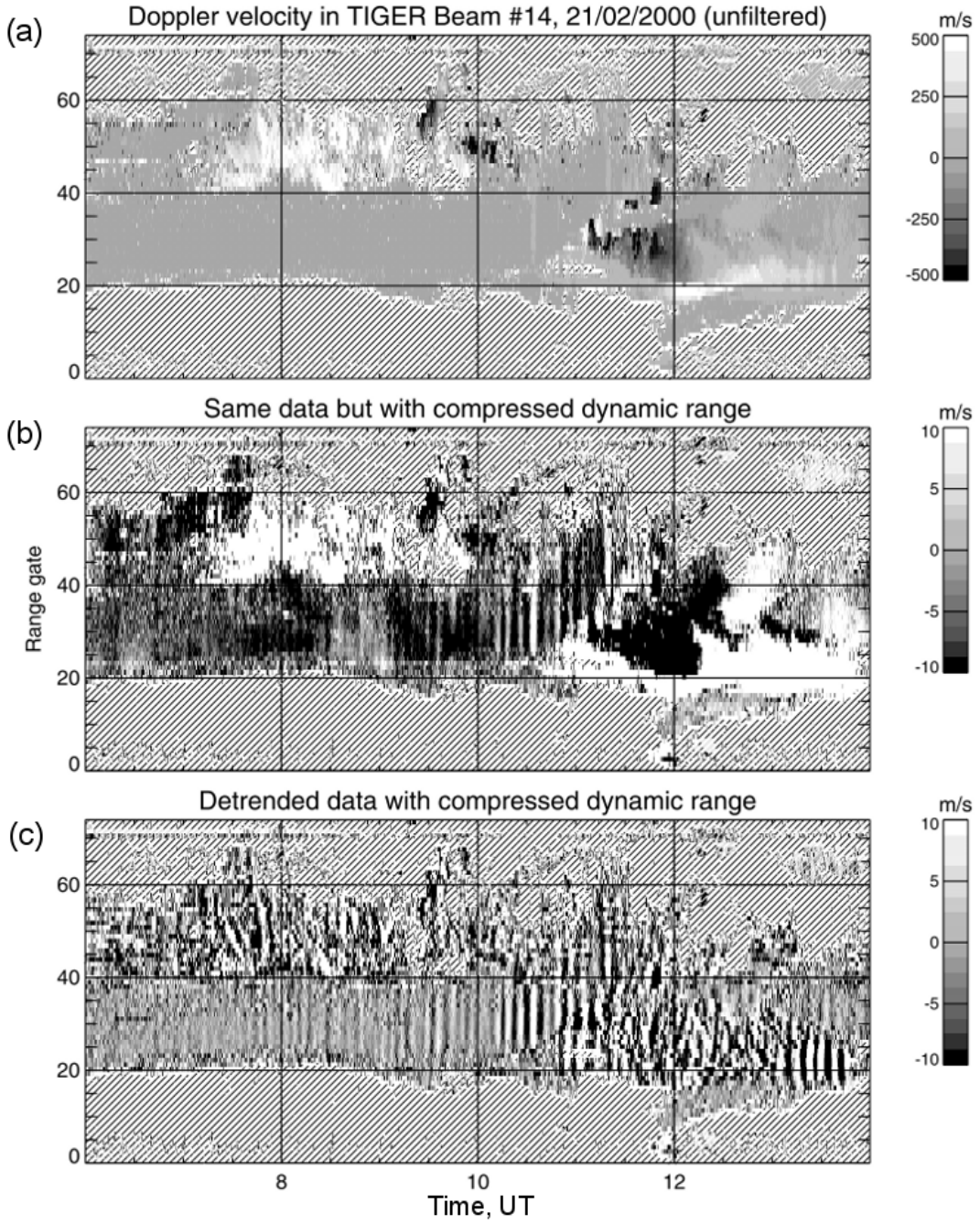

Figure 3.1: The original technique used to visualize ULF wave signatures in radar data. Panel (a) shows the Doppler velocity plotted in greyscale. Panel (b) shows the same data as (a) but limits the greyscale to ±10 m/s. Oscillations become visible as stripes of black and white from approximately 10:00-11:00 UT from range gates 20-50. Panel (c) shows the same interval after applying high pass filtering with a ten minute boxcar window. The greyscale is the same as in (b). Figure from *Ponomarenko et al.* (2003)

Tasmanian radar but a sampling rate of 6s, 28 days of data from the year 2000 were examined. It was found that Pc3-4 signatures were present daily in radar data from 8:00-12:00 MLT within ground scatter signals. Shown in Figure 3.2 is an example of Pc3-4 oscillations. Doppler velocity is plotted in range-time format for the interval 20:00-24:00 UT (≈8:00-12:00 MLT). These plots have been despiked and detrended with a 5 minute boxcar window. The velocity range has been restricted to ±10 m/s. Oscillations are clear in the ground scatter signals found in range gates 45-55 at 20:00 UT, and moving towards gates 35-45 as time progresses.

Figure 3.3 shows the power spectral density of the oscillations observed in radar from Figure 3.2 and the magnetic field data from Macquarie Island. The Doppler velocity spectra were computed for range gates 45 for 20:00-22:00 UT and gate 35 for 22:00-24:00 UT. The figure shows a spectral density maximum at 25-30 mHz in all spectra, linking the oscillations in radar to the Pc3-4 magnetic field oscillations observed on the ground.

3.1 ULF Wave Signatures in Radar Data

Visual analysis of SuperDARN data from Rankin Inlet was performed according to the techniques described by *Ponomarenko et al.* (2003). Data spikes were removed by removing points with velocities more than 3 standard deviations above the mean and Doppler velocities were high pass filtered using a detrending window of 10 minutes. Detrending the dataset makes it possible to identify oscillations that are offset from 0 m/s. For example, if an oscillation had an amplitude of 30 m/s but was superimposed on a drift of 100 m/s it would not be visible with the plotting limits. Detrending removes the long period background drifts. Plotting was done with time and range along the x and y axes respectively, and with Doppler velocity plotted in grey scale with limits of ±30 m/s. Special attention was paid to ground scatter data where Pc3-4 activity is most easily viewed. An example that shows the presence of velocity oscillations in ground echoes is shown in Figure 3.4(a). In this figure we can see synchronous oscillations between positive and negative Doppler velocities across range gates 20-50. These oscillations are spatially coherent and in phase along the beam's line of sight. The grey scale is deliberately saturated, giving these oscillations their contrasting black and white "zebra stripe" appearance. Their appearance is similar to the results from previous studies conducted at auroral latitudes shown in Figures 3.1 and 3.2. For contrast, Figure 3.4(b) shows an interval with ground scatter that lacks the velocity oscillations. Ground scatter is present in Figure 3.4(b) between range gates 40 and 60 and can be identified by the grey, unsaturated colour scale.

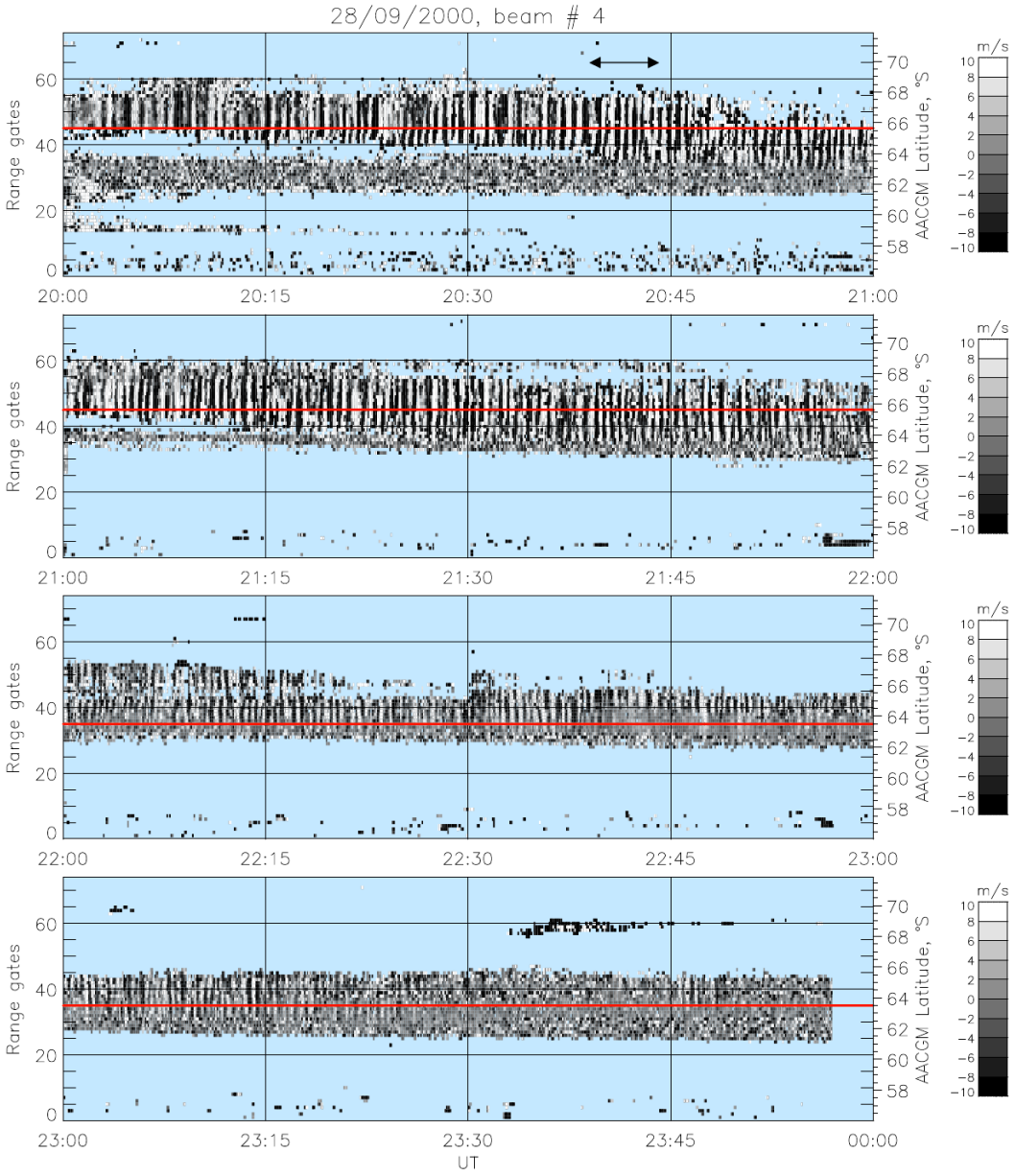

Figure 3.2: Pc3-4 waves visualized in Doppler velocity using the SuperDARN Tasmania station. The velocity was detrended with a 5 minute window and velocity is restricted to ±10 m/s. Each plot shows a consecutive hour. Oscillations can be seen within ground scatter data between range gates 45-55 at 20:00 and moving to lower ranges with time. The red line goes through the oscillations and indicates range gate 45 from 20:00-22:00 and gate 35 from 22:00 to 24:00. Figure from *Ponomarenko et al.* (2005)

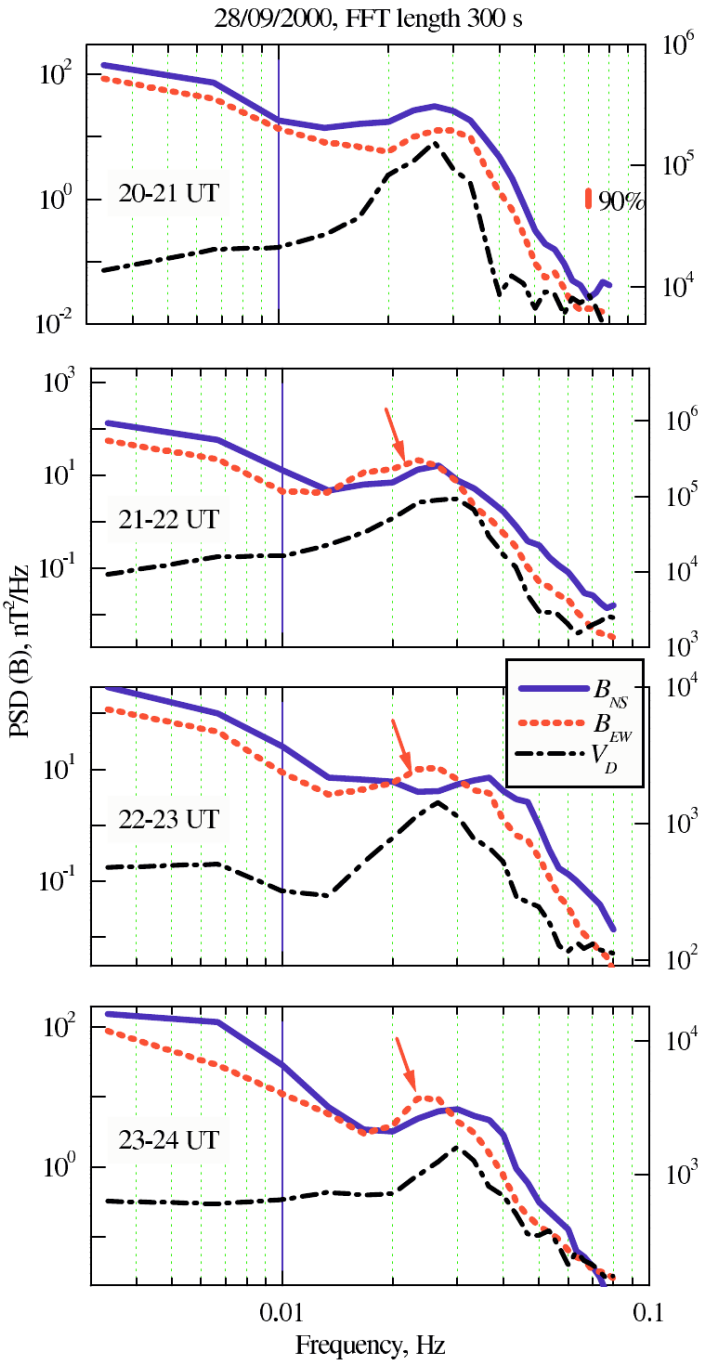

Figure 3.3: The power spectral density of Doppler velocities (black) from Figure 3.2. The windows show consecutive one hour intervals. The blue and red lines are the power spectra of the NS and EW components of the magnetic field measured on the ground for the same interval. The spectra show a peak in power at 25-30 mHz in all components. Figure from *Ponomarenko et al.* (2005)

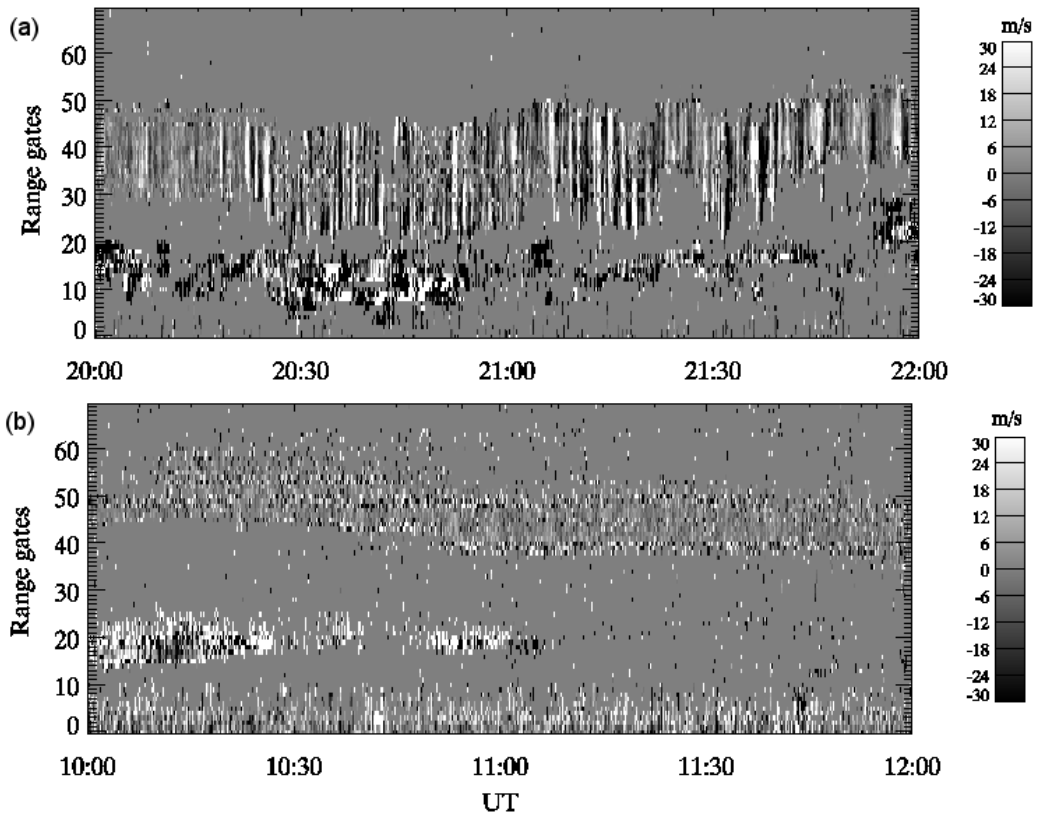

Figure 3.4: Panel (a) shows oscillations seen in Doppler velocity at Rankin Inlet beam 7 on April 17, 2008. Oscillations are observed in groundscatter between range gates 20-50. Panel (b) shows an example of groundscatter without the presence of oscillations on June 24, 2008 seen in range gates 35-60.

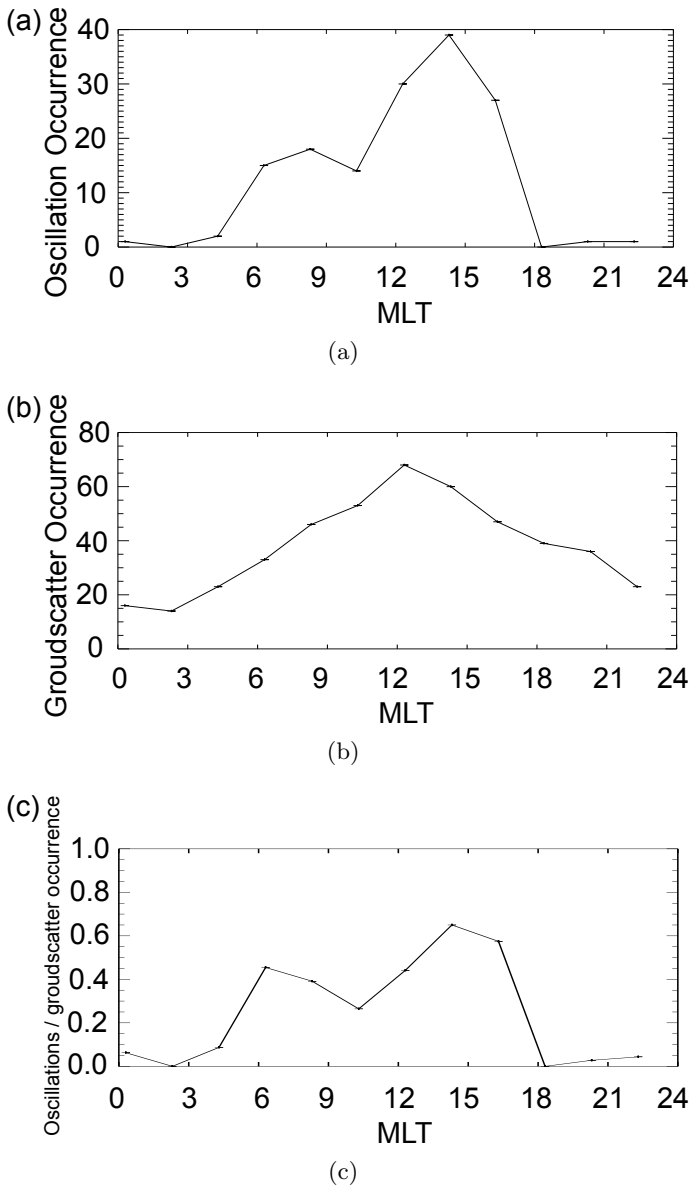

Figure 3.5: Results of time domain analysis. Panel (a) shows the number of occurrences of oscillations, panel (b) shows ground scatter occurrence and panel (c) shows their ratio within two hour windows at Rankin Inlet for 2008.

3.2 Visual Analysis

Variations in diurnal activity were first investigated manually by visually inspecting two-hour intervals: first for the presence of ground scatter and then for oscillations within that ground scatter. The presence of ground scatter was identified by large patches of amplitude-limited Doppler velocity deviations; no consideration was given to spectral width. Analysis was conducted for the year 2008. The number of two-hour intervals throughout the day of ground scatter with oscillations present is shown in Figure 3.5(a). Two peaks in activity are visible at 8:00 and 14:00 MLT. Because observability of the oscillations is dependent on the presence of ground scatter, Figure 3.5(b) shows the overall number of intervals with patches of ground scatter regardless of the velocity oscillations. The presence of ground scatter increases throughout the morning, peaks at noon, and decreases in the afternoon and evening. By normalizing the observations of oscillations within ground scatter with the observations of ground scatter itself we find the occurrence probability of oscillations. The diurnal trend of this probability is shown in Figure 3.5(c) which again shows two peaks, but pushes the morning peak earlier to 6:00 MLT. There are local minima in activity at approximately 10:00-11:00 MLT and at night. The local minimum found prior to noon contrasts with the cusp latitude findings which show a peak in activity in magnetometer (*Ponomarenko et al.*, 2002) and radar (*Ponomarenko et al.*, 2005) data prior to noon.

3.3 Spectral Analysis

Next we employed spectral analysis to study the oscillations observed in radar. For the two hour interval shown in Figure 3.6(a) we used ground scatter data from multiple ranges to construct a time series that we will Fourier analyze. The FITACF process determines ground scatter using Equation 2.11 Figure 3.6(a) shows an example of oscillations present in ground scatter Doppler velocity and 3.6(b) shows the Doppler velocities that are flagged as ground scatter by the FITACF process. While oscillations are still present, their amplitudes are clipped and the most powerful oscillations are excluded. The current ground scatter flag is insufficient to capture the amplitude of the oscillations that can be in excess of 50 m/s. We redefine the ground scatter flag using equation 2.11. A maximum Doppler velocity of 60 m/s was used and we didn't change the maximum spectral width value of 90 m/s. Figure 3.6(c) shows the plot of ground scatter Doppler velocity with the new ground flag considered. In Figure 3.6(a) the oscillations are only seen between range gates 20-50 and

we therefore took a median value for all valid ground scatter velocity values between range gates 20 and 50 for each time point. We could do this because the oscillations were spatially coherent with range, so that by taking a median of the points between these ranges we could specify the common trend across these range gates. As can be seen in the figure, there are often patches of missing data, making it difficult to select a range gate with continuous samples. Taking a median fills in missing data points with values from nearby ranges at the same time. A minimum of three valid points were required to determine the median value. The resulting median timeseries is shown in Figure 3.6(d). The time series was then resampled with a 6 second sample rate to obtain evenly spaced samples for Fourier analysis. This step was necessary because THEMIS mode does not take evenly spaced samples of the beam. THEMIS mode samples beam 7 every other other sample (6 s resolution) for a beam pattern: 1, 7, 2, 7, 3, 7... When beam 7 is sampled three times in a row, with 3 second resolution: 6, 7, 7, 7, 8, 7, 9... . Fourier analysis was conducted by processing 30 minute intervals with 50% overlap. Each interval was weighted by the Hanning window. The average spectrum was then found for the entire two hour interval, shown in Figure 3.6(e). The spectrum has a broad peak at 10 mHz, with a decrease in power towards higher frequencies. Figure 3.7 shows the same process for the period when oscillations were not present on June 24, 2008. Only data from range gate 47 were considered. The spectrum is shown in Figure 3.7(c) and is generally flat, with a slight power law decay as frequency increases.

The visual technique described in Section 3.2 is a time consuming and subjective process. Because of this we searched for a different method of determining the diurnal trend based on spectral analysis. In order to achieve this, we considered only instantaneous 30-min spectra. To illustrate the processing details, data from April 17, 2008 are shown in figure 3.8(a) for between 20:00 and 22:00 UT. The time series was extracted by taking a median of ground scatter Doppler velocity from range gates 20-50. This timeseries is shown in Figure 3.8(b) for the interval 20:30 to 21:00, which corresponds to the velocity oscillations confined to the red box in the top panel. The power spectral density of the time series is shown in black in Figure 3.8(c). For the entire year of 2008, average spectra were computed for half hour time intervals throughout the day. If a timeseries had fewer than 90% valid points before interpolation, the spectrum for that timeseries was rejected in the determination of the average. The red line in Figure 3.8(c) shows the average spectrum obtained for time interval 20:30 to 21:00 UT for the year 2008. Figure 3.9(a) shows the resulting average diurnal dynamic spectra for 2008. This result shows a trend similar to the one obtained by the visual time series analysis, i.e. peaks in power are seen at approximately 7 and 14 MLT and

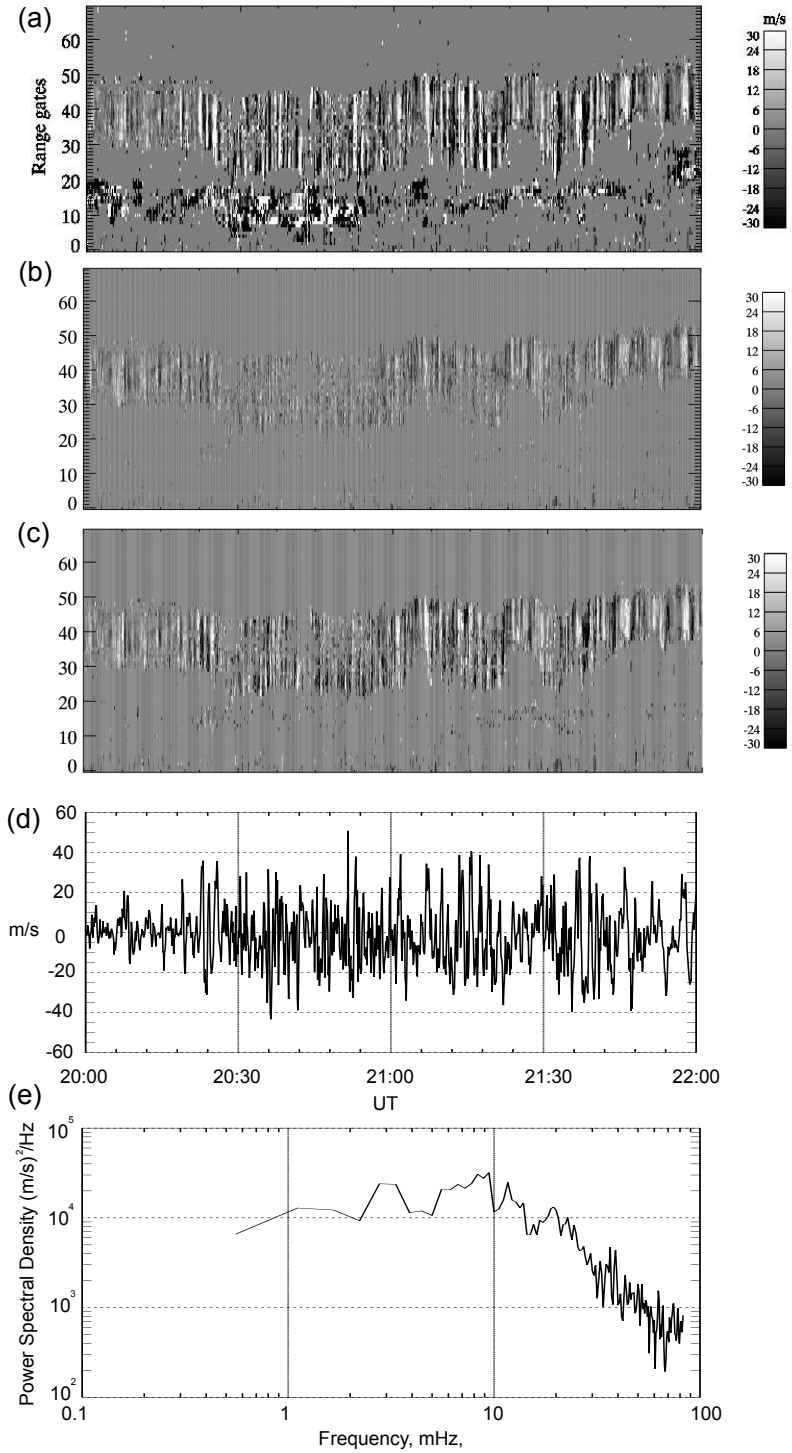

Figure 3.6: Panel (a) shows oscillations seen in Doppler velocity in Beam 7 of Rankin Inlet on April 17, 2008. Panel (b) shows ground scatter data as identified by FITACF. Panel (c) shows ground scatter data using redefined ground scatter flag. The timeseries obtained from (c) by taking a median ground scatter velocity from range gates 20-50 is shown in panel (d). The spectrum of the timeseries in (d) is shown in panel (e).

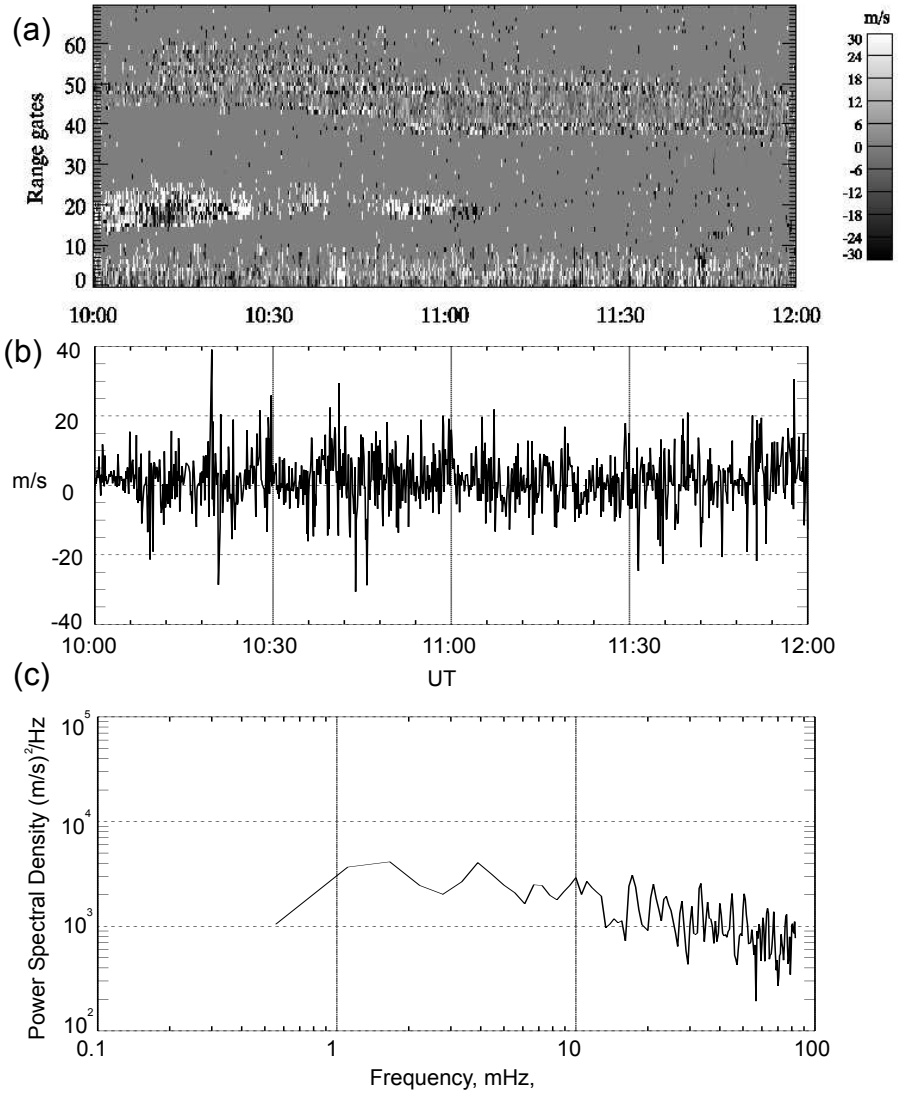

Figure 3.7: An example of groundscatter without the presence of oscillations can be seen on June 24, 2008 in beam 7 of Rankin Inlet from range gates 35-60 is shown in panel (a). Panel (b) shows the Doppler velocity of groundscatter in range gate 47. The spectrum of the timeseries in (b) is shown in panel (c).

a minimum in activity near noon at 11 MLT. The number of valid timeseries used to determine the diurnal trend is shown in Figure 3.9(b). It can be seen that the statistics during the night are poor, with fewer than ten valid timeseries available between 19:00 and 6:00 MLT. This gives unclear power spectra during the nighttime in Figure 3.9(a). More than 20 valid timeseries are available from 6:00 to 17:00 MLT, resulting in a clearer trend.

Figure 3.10 shows the spectral shapes obtained from the diurnal power spectra shown in Figure 3.9(a). Average spectra are shown for the morning peak from 6:15 to 7:45, the pre-noon minimum from 9:45 to 11:15, and the afternoon peak from 13:15 to 14:45 MLT. Comparing the three curves there is no prominant spectral enhancement in the morning or afternoon intervals. Instead,there is a broad increase in power across most of the spectrum.

3.4 Magnetometer Data

3.4.1 Experimental Setup and Data Processing

The Taloyoak magnetometer is located in the same region as the ionospheric reflection of ground-scatter signals from the Rankin Inlet radar. To determine the diurnal trend of magnetic oscillations on the ground we performed a spectral analysis similar to the process described in Section 3.3 for radar data. Magnetic data for May-August 2008 were analyzed by taking the spectra throughout the day with half-hour Hanning windows with 50% overlap. Some days were excluded from analysis due to highly disturbed conditions. Only summer data were considered because the majority of events observed with radar occur during the summer. The spectra were found for both the x (North-South) and y (East-West) components. The resulting diurnal spectra are shown in Figure 3.11. Both components show only a single peak in activity near noon, contrasting with the radar results in Figure 3.9 but agreeing with the auroral latitude findings of *Ponomarenko et al.* (2002).

We wish to compare the magnetic field measurements to the radar Doppler velocities. In order to compare two time series, their coherence can be found to determine the common frequencies. The coherence gives the absolute value of the correlation coefficient at every frequency, and can be thought of as the Fourier transform equivalent of correlation. The coherence, γ, and the phase of coherence ϕ, are given by

$$\gamma(f) = \frac{|\overline{S_{xy}}|}{\sqrt{\overline{S_{xx}}\,\overline{S_{yy}}}} \tag{3.1}$$

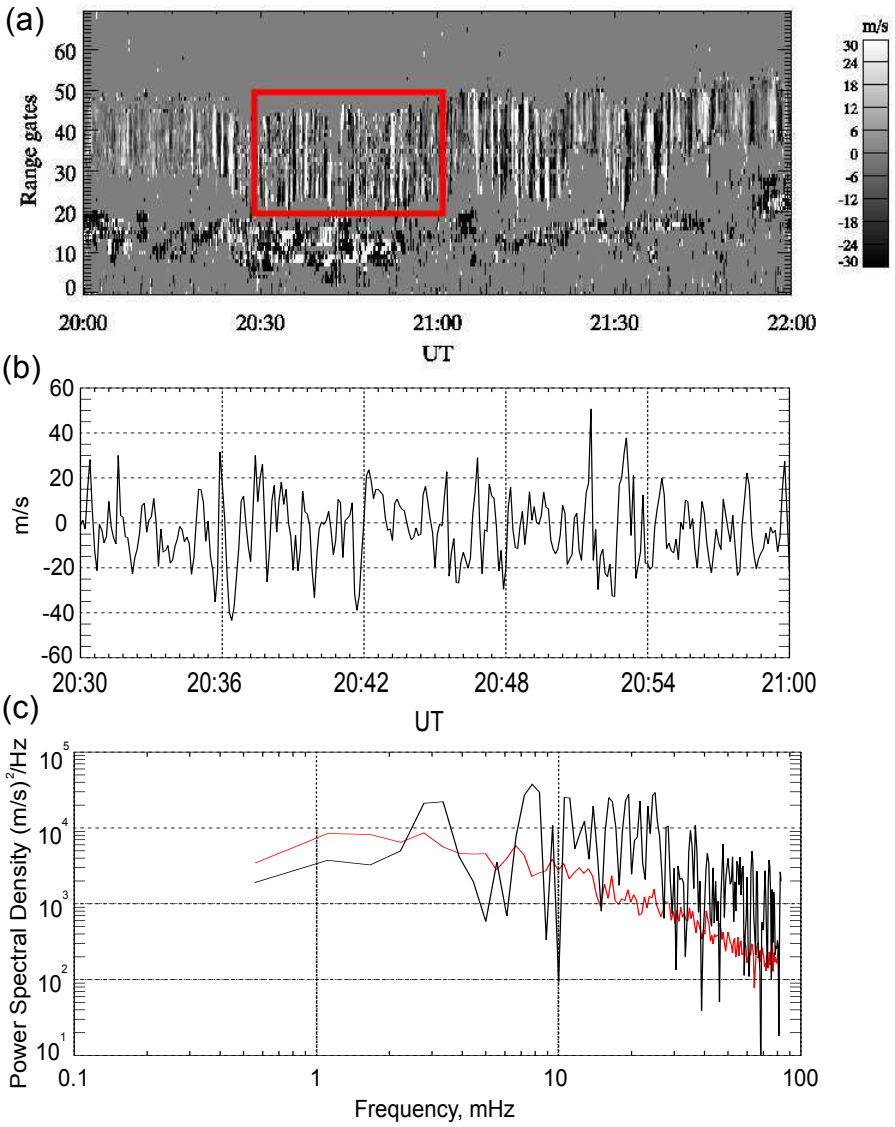

Figure 3.8: Determination of average diurnal spectra. Panel (a) shows the Doppler velocity from Beam 7 of Rankin inlet on April 17, 2008. The highlighted area in (a) is used to generate the timeseries shown in panel (b) which is then Fourier analyzed. The spectrum of the timeseries is shown by the black line in panel (c). The red line shows the average spectrum for the time interval 20:30-21:00 UT for 2008.

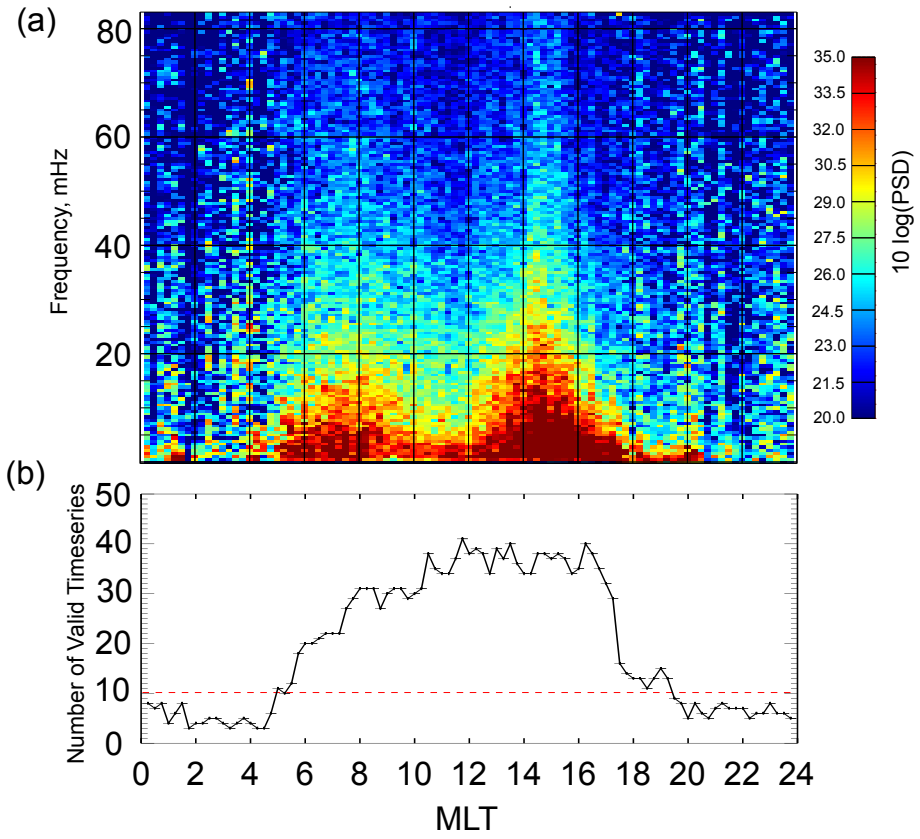

Figure 3.9: (a)Average diurnal power spectra of the Doppler velocity of ground scatter seen in beam 7 of Rankin Inlet for the year 2008. (b) The number of spectra used to compute the average shown in (a). The red line marks 10 valid spectra along the y-axis. Poor statistics are available at night, with <10 for any time between 19:00 and 5:00 MLT, with typical values of N =5. The spectra for nighttime is therefore unclear. During the day, more than 20 spectra are used to compute an average, giving a much clearer trend. The diurnal power shows peaks at approximately 7:00 and 14:00 MLT with a minimum in power at 11:00 MLT.

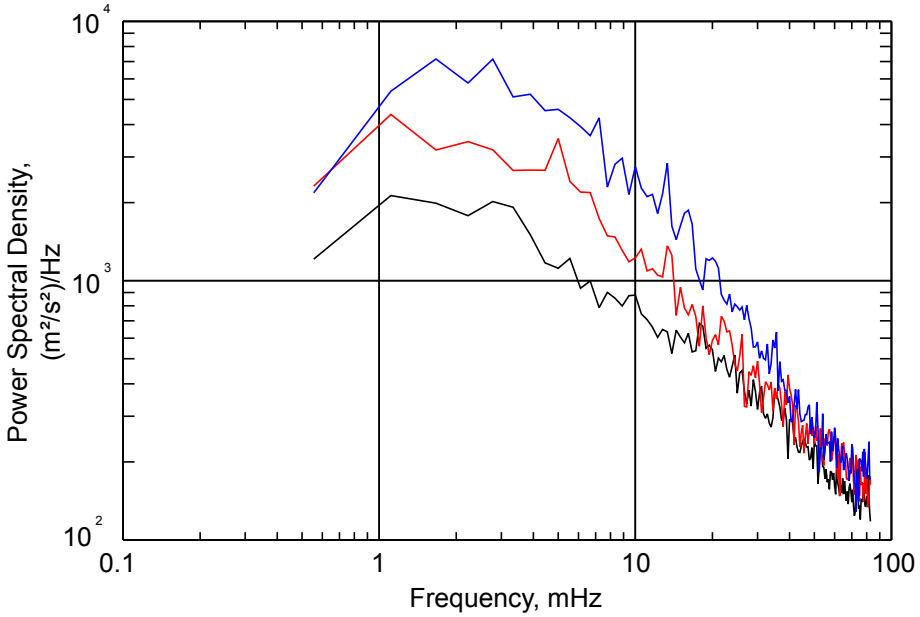

Figure 3.10: Average power spectra for 2008. The red line is the average spectrum for 6:15 to 7:45, black for 9:45 to 11:15, and blue for 13:15 to 14:45 MLT.

$$\phi(f) = \arctan\left[\frac{Im(\overline{S_{xy}})}{Re(\overline{S_{xy}})}\right], \tag{3.2}$$

The cross spectrum of two time series, S_{xy} is found by the product of the Fourier transforms of the two time series.

$$S_{xy}(f) = S_x(f)S_y^*(f) = (\int_a^b x(t)exp^{-i2\pi ft}dt)(\int_a^b y(t)exp^{-i2\pi ft}dt)^* \tag{3.3}$$

(*Bendat and Piersol*, 1966). The Power spectra, S_{xx} and S_{yy}, are the cross spectra of a time series with itself. The overbars in Equations 3.1 and 3.2 indicate that the spectra are averaged over several intervals. The resulting coherence is a function of frequency and will range between zero and one: zero for no agreement and one for perfect agreement. The phase will indicate the lag between the two signals. For example: Taking the coherence between a sine and cosine wave with identical 10 mHz frequencies will give a coherence of γ =1.0 and a phase ϕ =90° at 10 mHz and γ =0.0, ϕ =0° at all other frequencies. The coherence between two entirely random timeseries will approach zero, and the phase will be randomly distributed at all frequencies. In this work, the coherence and phase are determined by analyzing 6 minute Hanning-windowed intervals with 50% overlap over a 1 hour interval.

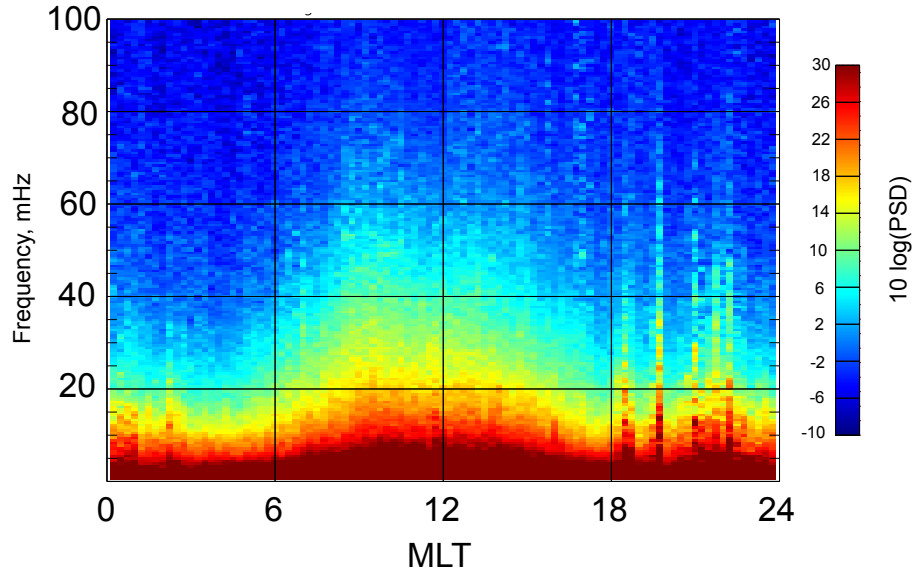

(a) Diurnal power spectra for x (North) component

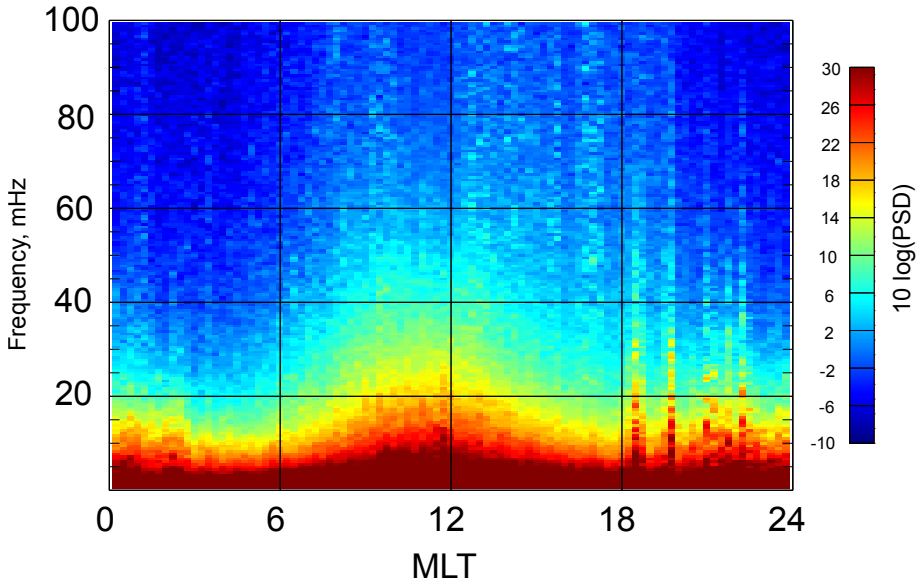

(b) Diurnal power spectra for y (East) component

Figure 3.11: Average daily power spectra for the horizontal components of magnetic field at Taloyoak during summer 2008. Both components show only a single peak near noon.

3.4.2 Event Study

Several events were selected to compare oscillations observed in radar to the ground magnetic field. Events were picked from 2008 THEMIS scans and 2009 ULF scans at Rankin Inlet and compared to Taloyoak magnetometer data. The selected intervals are shown in Table 3.1. Intervals were selected for clear and continuous oscillations observed in radar data. Looking at a single event where activity was present in the radar we also looked at activity on the ground. Oscillations in radar are shown in Figure 3.12(a) for April 21, 2008. The x and y components of magnetic field are shown in Figure 3.12(b). Oscillations are present in both time series. The radar time series was determined as the median ground scatter velocity between ranges 30 and 50. The coherence was determined between the radar and magnetometer time series for the interval 13:30-14:30 UT. The results are shown in Figures 3.12(c) and 3.12(d). There is very little agreement between the time series with coherence levels of 0.5 or less across all frequencies. While oscillations are present in both radar and magnetometer data they do not appear to be related. Furthermore for all the events shown in Table 3.1, coherence between radar and magnetometer data was less than 0.5 at all frequencies.

Year	Date	Time (UT)	Range Gates
2008	April 9	20:30-21:30	25-50
2008	April 17	20:30-21:30	20-50
2008	April 21	13:30-14:30	30-50
2009	June 14	22:00-23:00	20-50
2009	July 24	21:00-22:00	20-50
2009	August 22	20:30-21:30	30-50
2009	September 16	15:00-16:00	30-50
2009	September 16	20:00-21:00	30-50

Table 3.1: Intervals analyzed for coherence between oscillations observed in radar at Rankin Inlet and magnetometer data at Taloyoak.

3.5 Spatial Coherence

ULF scans provided high resolution data from multiple beams and were used to get a 2 dimensional view of the oscillations in radar. Shown in Figure 3.13(a) is an example of simultaneous oscillations in different beams at Inuvik on June 12 2009, when oscillations were present in beams 8, 12, and 15 for more than two hours. For the one hour interval from 00:30 to 1:30 UT, time series were obtained by taking a median of range gates 30-50. The coherence magnitude and phase between beams 8 and

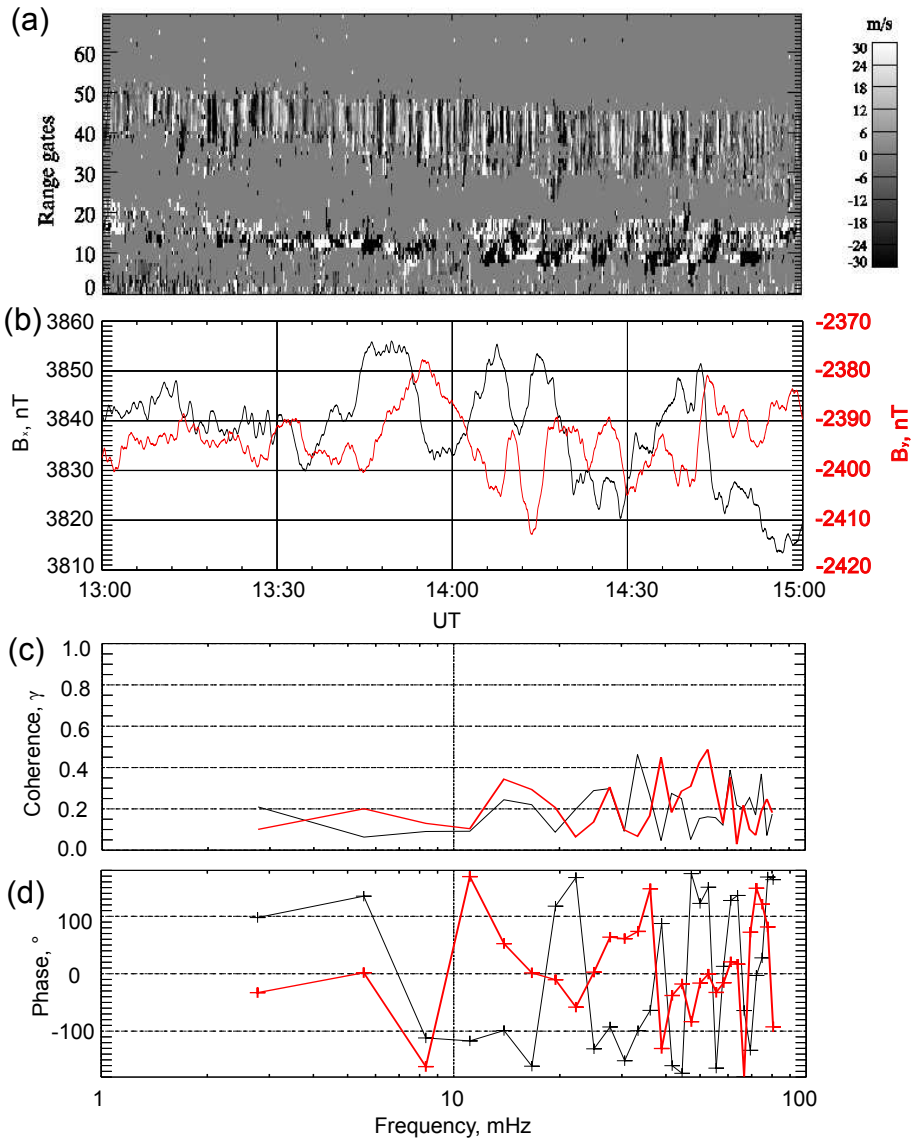

Figure 3.12: The coherence between Doppler velocities at the Rankin Inlet radar (a) and magnetic field values at Taloyoak (b) on April 21, 2008. The x and y components are shown respectively black and red, respectively. (c) Coherence and (d) phase are computed for 13:30 to 14:30.

12 is shown in Figures 3.13(c) and 3.13(d). Poor coherence of less than 0.4 was observed between the two beams across all frequencies. The distance between the oscillations in beams 8 and 12 can be easily approximated. There are ≈12° between beams 8 and 12, and the oscillations are present at ranges 30-50 in ground scatter. If the ground scatter signal interacts with the ionosphere at approximately the midpoint of its trajectory, the range of these signals is 900 km from the ground station. The distance between the oscillations in beams 8 and 12 is therefore approximately 200 km.

On the other hand, looking along a beam's line of sight we see oscillations spanning from range gates 30 to 50. With ≈22.5 km range gates for ground scatter, this corresponds to approximately 450 km along the beam's line of sight. This coherence along the beam's line of sight is shown in Figure 3.14. From the range-time plot shown in 3.13, the Doppler velocity of only range gates 35 and 43 are plotted in Figures 3.14(a) and (b) from 0:15-1:15 UT. The coherence and phase between them are shown in Figures 3.14(c) and (d). The coherence is between 0.6 and 0.8 at frequencies of less than 20 mHz with a phase of approximately zero. Coherence falls to lower values as frequency increases beyond 20 mHz. For ground scatter, the difference in the distances corresponding to range gates 35 and 43 is approximately 180 km, which is comparable to the distance between beams 8 and 12 that show poor coherence.

3.5.1 Comparison of Polar and Auroral latitudes

Comparison of the results from the polar cap region can be made using auroral latitude stations at Saskatoon and Prince George. Shown in Figure 3.15 is a comparison between activity seen in beam 6 of the Saskatoon radar operating in THEMIS mode and the nearby Gillam magnetometer. Oscillations are present in the ionospheric scatter seen between range gates 10 and 20. We analyzed the interval from 2:00 to 3:00 UT between range gates 10 and 20. Good coherence of more than 0.7 is observed at approximately 10 mHz between the radar range gates and the y component of the magnetic field.

To compare the spatial coherence results from the polar cap region to the auroral region, high resolution ULF scans were performed at Saskatoon and Prince George stations during the summer of 2012. Ground scatter was less common during this time of the year and the observed oscillations were more commonly seen in ionospheric scatter. Figure 3.16 shows the presence of oscillations in multiple beams in ionospheric scatter as seen from Prince George on September 17, 2012. A time series was extracted by taking the median of velocity data between ranges 10 and 20. The coherence

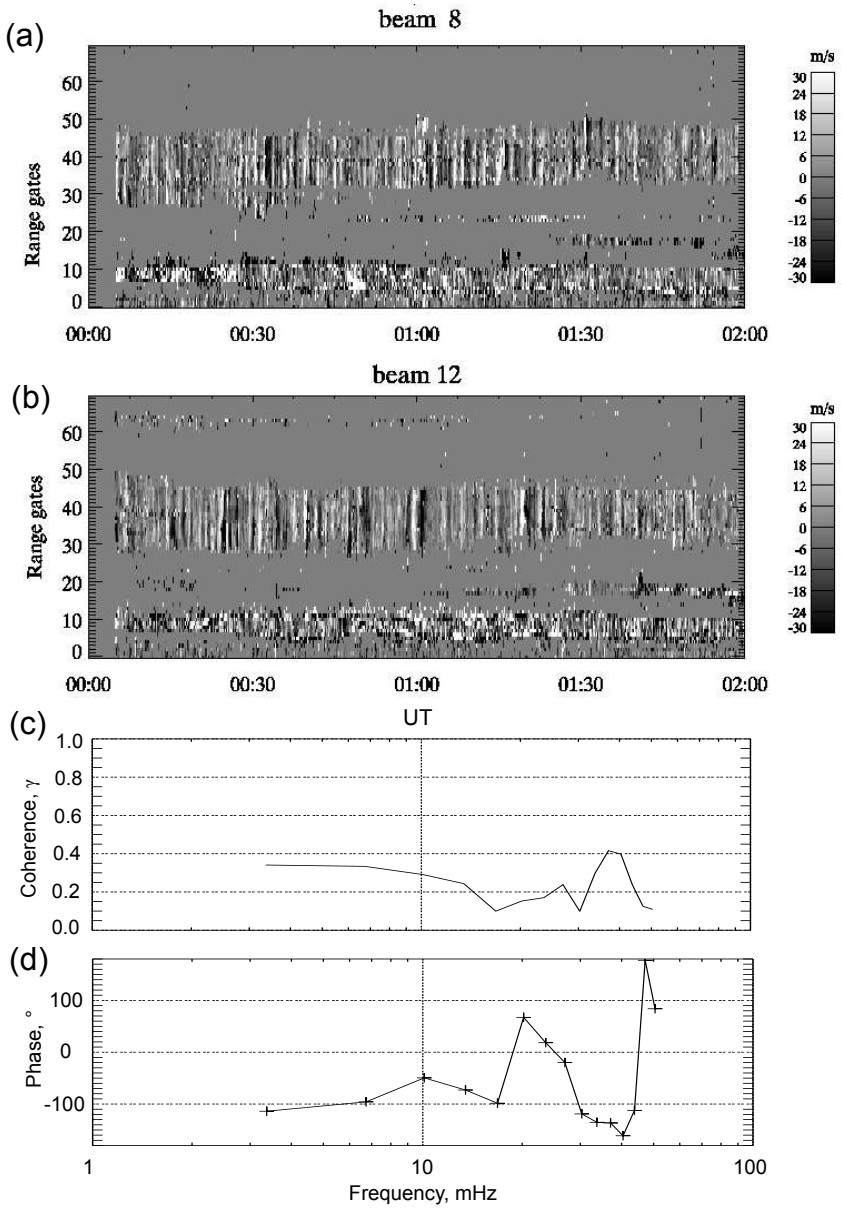

Figure 3.13: The presence of oscillations in (a) beam 8 and (b) beam 12 at Inuvik on June 12, 2009. The (c) coherence and (d) phase of the oscillations are calculated from 0:30 to 1:30.

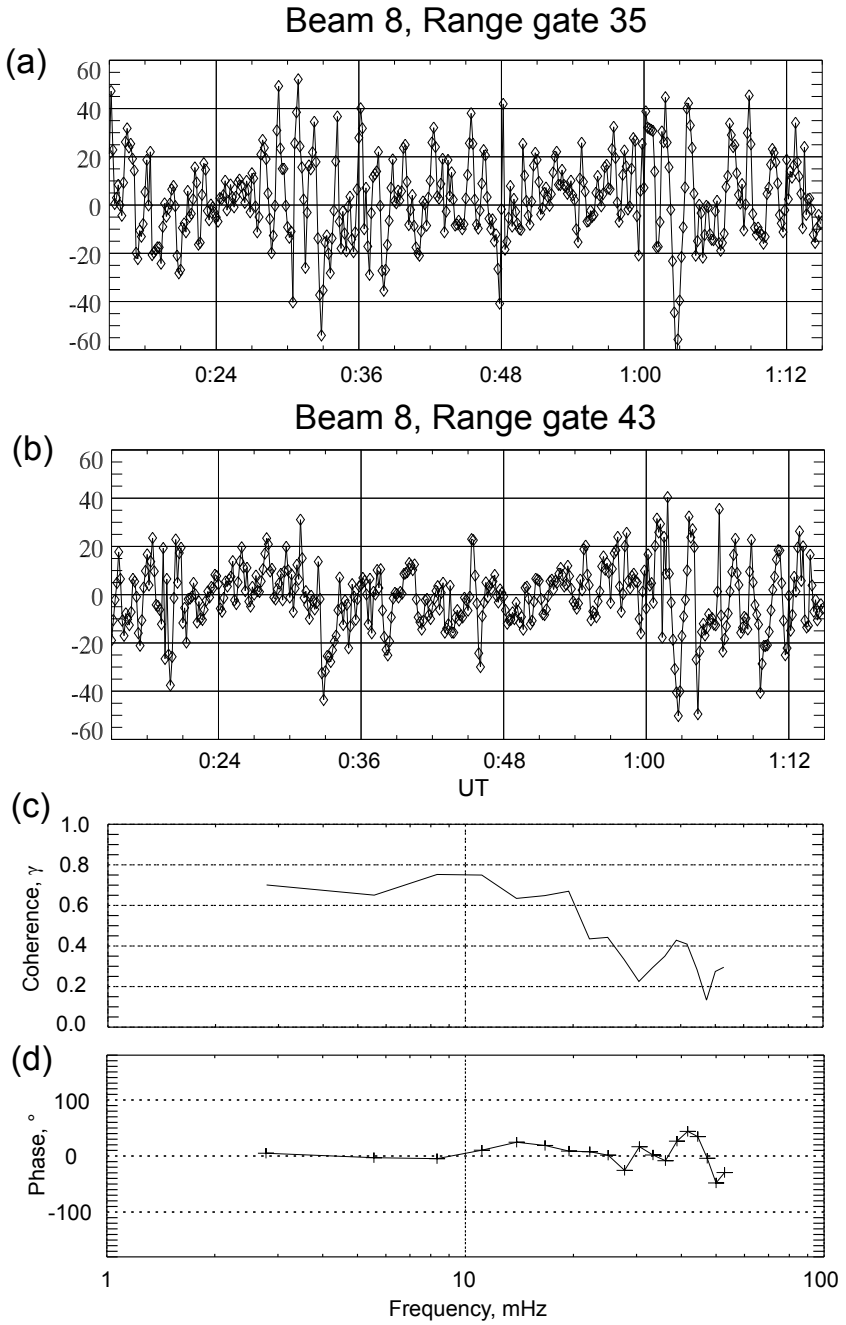

Figure 3.14: Doppler velocity oscillations seen (a) range gate 35 and (b) range gate 43 of beam 8 at Inuvik on June 12, 2009. The (c) coherence and (d) phase between the two range gates.

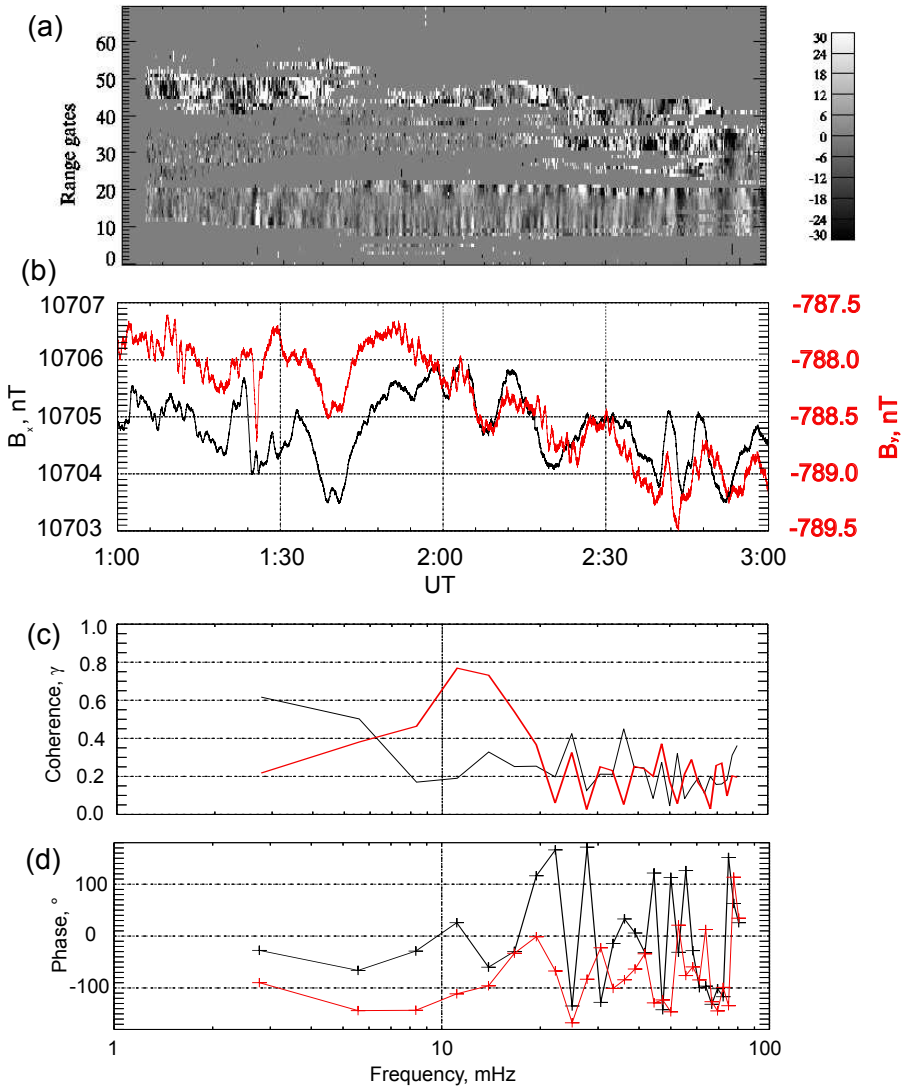

Figure 3.15: Comparison of Doppler velocities at the Saskatoon radar and closely located magnetic field values at Gillam. Formatting is the same as Figure 3.12.

and phase from 4:00 to 5:00 between beams 5 and 8 is shown in Figures 3.16(c) and 3.16(d). We can see coherence of greater than 0.7 and a phase difference of 50° at 10 mHz.

The activity seen in beam 8 is compared with the ground magnetic field at Fort Simpson in Figure 3.17 For the interval 4:00 to 5:00 we see good coherence of 0.7 at 10 mHz when comparing either the x or y magnetometer components to range gates 10 to 20 of beam 8 at Prince George. A phase difference of approximately 50° is found for the x component and 150° for the y component.

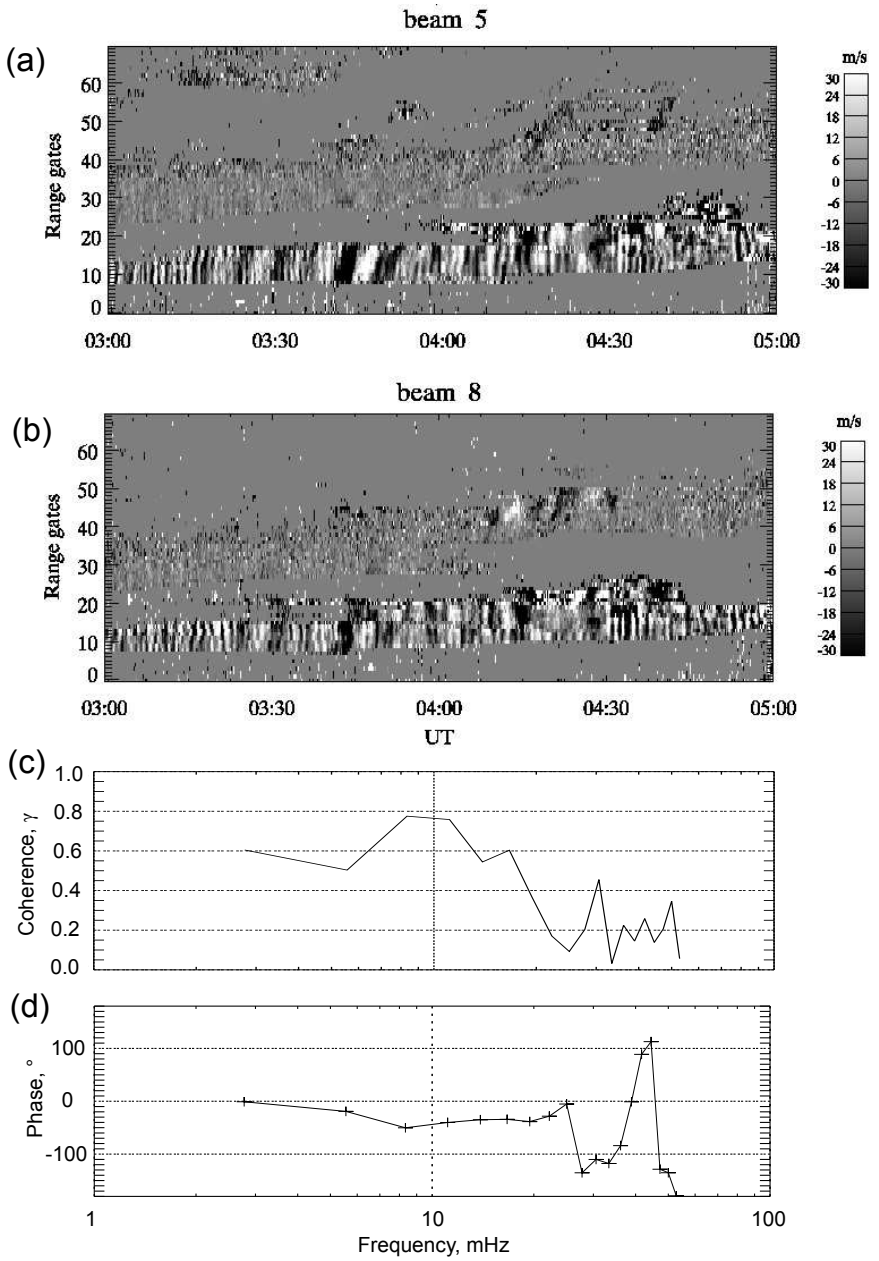

Figure 3.16: Oscillations observed in different beams of the auroral latitude Prince George radar on September 17, 2012. The coherence and phase between the intervals from 4:00 to 5:00 are presented. Formatting is the same as Figure 3.13

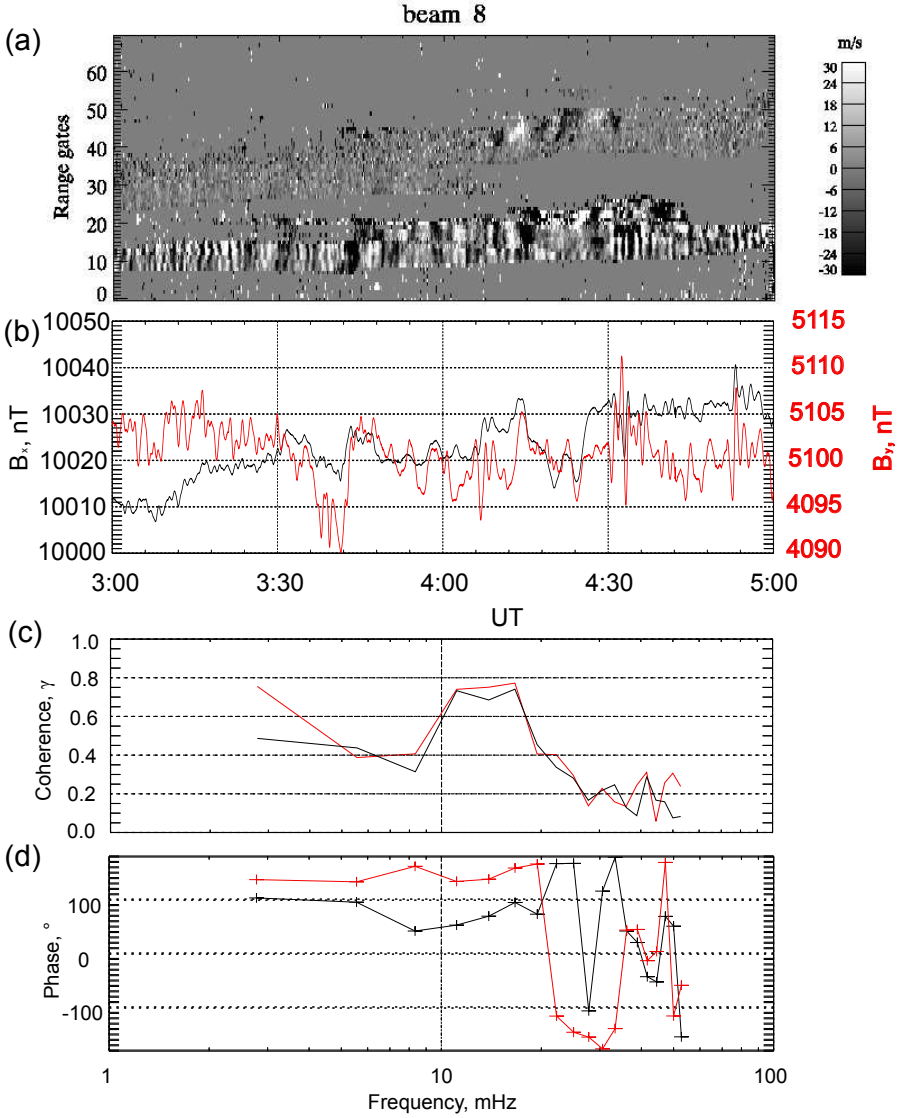

Figure 3.17: Coherence of oscillations seen in radar data from Prince George and magnetometer data from Fort Simpson on September 17, 2012. Formatting is the same as Figure 3.12

Chapter 4

Discussion, Conclusions and Future Work

4.1 Discussion

Ground scatter signals are most useful for observing ULF wave activity. This is in part because the Doppler velocity of ground echoes are free from the large amplitude, changing horizontal drifts that obscure ULF signatures in ionospheric scatter (*Ponomarenko et al.*, 2003). However, using ground scatter for observations has its limitations. The presence of ground scatter depends on having favourable propagation conditions and a suitable ground surface to cause scattering. At night, the absence of photoionization affects the index of refraction, preventing HF signals from reaching the ground. As a result, the presence of ground scatter has a strong local time dependence, as shown in Figures 3.5(b) and 3.9(b). For this reason a diurnal trend for the oscillations can only be determined for the interval 6:00 to 17:00 MLT, when ground scatter is common. In addition, a suitable ground surface is also required for ground scatter to be observed. This surface can be a corrugated ground surface, water waves, or a mountain range. During the winter, ice covers much of the sea surface in the Northern polar cap and makes for a poor scattering surface at high latitudes by suppressing waves. Only mountain ranges return ground echoes year round.

A combination of a poor scattering surface and a decrease in ionospheric electron densities during winter, leads to very little ground scatter observed by polar cap radars (*Ponomarenko et al.*, 2010a). Conversely, there is much more ground scatter observed during the summer months when the ice has melted and the ionosphere is more dense, providing more opportunities to observe the oscillations. Our ability to determine a seasonal trend is thus hampered by the seasonal dependence in ground scatter occurrence.

Our observations of Doppler velocity oscillations in ground scatter signals are coherent and in phase along a beam's line-of-sight. This feature is consistent with Pc3-4 wave observations at lower latitudes (*Ponomarenko et al.*, 2003). However, upon closer inspection, there are significant differences between the oscillations we observe and the properties of Pc3-4 waves.

(1) The spectrum of the oscillations shown in Figure 3.6(e) shows that the power consists of a plateau below 10 mHz and a power law decrease at higher frequencies. The spectrum that we observe at high latitudes is therefore noticeably different from the lower latitude spectrum which shows a much more distinct band-limited enhancement at approximately 30 mHz on top of the power law background (*Ponomarenko et al.*, 2002) which *Yumoto* (1985) has linked to the cyclotron frequency of reflected protons upstream of the bowshock.

(2) The double-humped diurnal feature in Figure 3.9 found using polar cap radar contrasts with the diurnal trend of magnetic oscillations found in the polar cap at Terra Nova Bay by *Villante et al.* (2000) and at mid-latitudes by *Ponomarenko et al.* (2002). Both studies show a single peak centered approximately on magnetic local noon. However, the observed diurnal trend on the ground at the polar cap magnetometer at Taloyoak shown in Figure 3.11 does agree with these studies, showing a single near noon peak in power. It is possible that the single noon peak observed on the ground at Taloyoak is caused by the proximity to cusp latitudes. Ground-based magnetometers have a wide field of view. Activity in the cusp latitude ionosphere could be projected to a wider region on the ground, causing magnetic signatures of cusp latitude ULF waves to be observed at the equatorward boundary of the polar cap (*Ponomarenko et al.*, 2001). This hypothesis could explain the similarities between the trends found by magnetometers at auroral latitudes and in the polar cap region near the open-closed field line boundary.

(3) Comparing the observations with the ground magnetometers to the observations made with polar cap radars we find very little coherence, as shown in Figure 3.12. Upon reaching the ionosphere, low frequency MHD waves should be partially reflected. Some fraction of the incident energy should be converted to electromagnetic waves leading to propagation from the ionosphere through the neutral atmosphere to the ground, as described in the Introduction and detected in the closed field line regions. The lack of agreement between the radar and magnetometer records indicate that the oscillations observed in the polar cap ionosphere do not generate an electromagnetic signal that propagates to the ground.

(4) The poor spatial coherence observed between beams compounds the puzzling nature of the polar cap results. The most recognizable characteristic of the oscillations that we studied is high spatial coherence along the beams' line of sight, as shown in Figure 3.14; it is the reason we're able to easily identify the oscillations. It would therefore seem that the apparent spatial coherence along a beam is due to propagation effects in ground scatter as indicated by Equation 2.9, causing a single localized disturbance to affect several range gates. In this respect the coherence between

beams could be a better estimate of real spatial coherence. In this case the oscillations would have a spatial coherence length of less than 200km. In contrast, Pc3-4 waves are large scale waves with coherence scales of thousands of kilometers as has been demonstrated by e.g. *Howard and Menk* (2001).

These differences between our polar cap observations and the expected properties of Pc3-4 waves lead us to conclude that the observed oscillations are not the Pc3-4 waves that we originally intended to study. Any explanation of the observed Doppler shift oscillations in the polar cap must address the following features. (1) It must cause a Doppler shift in ground scatter. (2) It should lack an electromagnetic component or explain why a magnetic component is not observed simultaneously on the ground nearby. (3) It should be a localized phenomenon with a small spatial coherence length to explain the poor coherence observed between beams. (4) It would have to explain the diurnal trend that has peaks in activity in the early morning and early afternoon with a minimum in activity at noon. (5) The cause must also be very common, happening almost daily during the summer when radar observations of ground scatter are possible.

If the cause was a neutral atmospheric process, given the very low frequency, one potential mechanism for oscillations is infrasound waves. Low frequency compressional waves with frequencies of 30-80 mHz have been detected at high latitudes using microphones placed around the auroral oval. A source of these waves is believed to be supersonic motion of auroral structures (*Wilson*, 1967). The duration of these waves is often usually several minutes, but the waves we observe with radar often last for several hours. It is therefore unlikely that the velocity oscillations we observe are infrasound waves produced by an auroral source.

Another candidate for the observed oscillations could be gravity waves. These are caused by a pocket of air whose density is different from the atmosphere surrounding it. It then rises and falls, continually overshooting its equilibrium point. Gravity waves have a maximum frequency given by the Brunt-Vaisalla frequency with a minimum period of approximately 4 minutes. Our observed oscillations have a period of approximately 100s, ruling out gravity waves.

There is an alternative explanation based on a different approach. A Doppler shifted signal is recognized by SuperDARN as a change in the phase path length of the signal with time. Although the FITACF process interprets a Doppler-shifted signal as the velocity of a target, this change in phase may have other causes. In Chapter 2, it was shown that the Doppler velocity associated with ground scatter can be caused by a vertical motion of the ionosphere. However, in the continuity equation (Equation 2.7) used to derive the Doppler shift of ground scatter (Equation 2.9), chemical

processes were neglected. If we leave these processes in it can be shown that the Doppler shift may in fact be due to variations in the ionization rate along the ray path. From the first term of Equation 2.5 we have

$$\Delta\omega = -2k_0 \int_A^B \frac{\partial n}{\partial t} ds \,, \tag{4.1}$$

where the factor of 2 comes from the doubling caused by the return journey from the scattering point to the transmission station. From the Appleton-Hartree equation in Equation 2.1 and the plasma frequency in Equation 2.2 we obtain

$$\frac{\partial n}{\partial t} = \frac{-e^2}{8\pi^2 \epsilon_0 m_e n f_0^2} \frac{\partial N_e}{\partial t} \tag{4.2}$$

which can be substituted into Equation 4.1 to produce

$$\Delta f = \frac{e^2}{4\pi^2 \epsilon_0 m_e \lambda_0 f_0^2} \int_A^B \frac{1}{n} \frac{\partial N_e}{\partial t} ds \,. \tag{4.3}$$

The Doppler shift Δf can be expressed as the Doppler velocity calculated through the FITACF process using Equation 2.10. If we assume a linear increase in the electron density ΔN_e with time Δt across a uniform portion of the ray path Δs we can estimate the increase in electron density required to cause the observed Doppler shifts from

$$\Delta N_e = \frac{-8\pi^2 \epsilon_0 m_e n f_0^2 v_D \Delta t}{e^2 \Delta s} \,. \tag{4.4}$$

In order to infer a Doppler velocity of 30 m/s over 100s we would require a change in electron density of approximately $7 \times 10^{10} m^{-3}$ along 100 km of the ray's path. This density perturbation may be anywhere from a tenth to half of the E-region density.

Precipitation events can easily cause an increase in the electron density of this order of magnitude. Although the majority of PolarDARN observations occur in the polar cap, PolarDARN sites are located inside the auroral oval. The radar signals must therefore enter the ionosphere inside the auroral oval, a region known for intense particle precipitation. In these events, charged particles flow along magnetic field lines from high altitudes down to the ionosphere and ionize multiple neutral particles per precipitating particle (*Carlson and Egeland*, 1995). An increase in the electron density along a portion of the ray path would cause a negative Doppler shift, and a net recombination of

the ionized particles would be interpreted as a positive Doppler shift. The ion loss rate of the E region is of the order of 10^9 $\mathrm{m^{-3}s^{-1}}$. This is estimated using recombination rates for $[NO^+]$ and $[O_2^+]$ of the order of 10^{-13} $\mathrm{m^3s^{-1}}$ (*Schunk and Nagy*, 2000) and E region ion and electron densities of 10^{11} $\mathrm{m^{-3}}$. Over 100 s, these recombination rates are of the same order as the ionization rates required to cause the observed Doppler shifts. With the aurora known to be highly variable in time and space, time scales of the order of 100 s are easily achieved.

Assuming a motionless ionosphere, ion production, P and loss are responsible for changes in the ion density N,

$$\frac{dN}{dt} = P - \alpha N^2 \,, \tag{4.5}$$

where α is the dissociative recombination rate. If we assume a constant production rate, we obtain the separable differential equation

$$\frac{dN}{P - \alpha N^2} = dt \tag{4.6}$$

which has the solution

$$t = \frac{1}{2\alpha N_{ss}} \ln \left[\frac{(N_{ss} + N)}{(N_{ss} - N)} \frac{(N_{ss} - N_0)}{(N_{ss} + N_0)} \right] , \tag{4.7}$$

where N_0 is the initial ion density and N_{ss} is the steady state value, defined as

$$N_{ss} = \sqrt{\frac{P}{\alpha}} \,. \tag{4.8}$$

We model the case where ions are produced by a stream of auroral electrons as a step function in the production rate, P. When production dominates, $N_{ss} \gg N_0$ and Equation 4.7 reduces to

$$t = \frac{1}{2\alpha N_{ss}} \ln \left[\frac{N_{ss} + N}{N_{ss} - N} \right] . \tag{4.9}$$

On the other hand, when production is turned off $P \to 0$, we have $N_{ss} \ll N_0$ and the solution reduces to

$$t = \frac{N_0 - N}{\alpha N N_0} \,. \tag{4.10}$$

From Equations 4.9 and 4.10 we find that the time required for the ion density to rise or fall to half of the steady state value of $10^{11}\mathrm{m^{-3}}$ is of the order of 100 s. This is consistent with the periods we observe in the polar cap Doppler shifts.

While the existence of the observed oscillations in ground scatter Doppler velocity might be explained by precipitation bursts, the fact remains that we did not observe the Pc3-4 oscillations

that we originally intended to study. The failure to detect Pc3-4 waves using radar may be caused by the magnetic field line orientation approaching vertical in the polar caps. In this case, Alfvén wave magnetic disturbances will become essentially horizontal and the vertical component of $\vec{E} \times \vec{B}$ drift will approach zero. Comparing magnetic field inclination angles, we find that the vertical component of $\vec{E} \times \vec{B}$ drift at 80° MLAT will be half of the vertical drift at 70° MLAT. These geometric consideration would make observations more difficult, especially in the presence of comparable or larger fluctuations caused by particle precipitation. However, the Hall current will still generate an electromagnetic wave that propagates through the neutral atmosphere to the Earth's surface where it can be registered by magnetometers.

4.2 Conclusions

In this work we have used SuperDARN HF radar to observe oscillations in the polar cap ionosphere at Rankin Inlet and Inuvik. These oscillations observed in the Doppler velocity of ground scatter are unlikely to be caused by Pc3-4 ULF waves. We conclude this from the following properties, all of which contrast with those of the conventional Pc3-4 waves.

1. The absence of a band-limited enhancement in the power spectrum of the oscillations,
2. A diurnal trend with a double peak in power at 7 and 14 MLT instead of a single peak near noon,
3. Poor coherence between oscillations observed using HF radar and ground-based magnetometers,
4. Poor spatial coherence between observations made by separate radar beams.

Instead, the observed oscillations may be caused by particle precipitation modulating the E region electron density along the ray path, which is supported by order-of-magnitude estimates. If future studies confirm this hypothesis, it may be possible to use HF radar to study this phenomenon. This would be especially useful on the day-side where optical imagers are saturated by sunlight.

Future studies of ULF waves in the polar cap must be done with caution when using HF radar to study their activity in the ionosphere. The activity that we observe using the visual recognition technique from *Ponomarenko et al.* (2003) masquerades as ULF waves, demonstrating that HF radar is not always a suitable substitute for magnetic field measurements in ULF studies. Without

independent confirmation that ionospheric radar oscillations are caused by ULF waves, either by the presence of large spatial coherence or coherence between radar and magnetometer observations, we cannot be sure that radar observations are the result of ULF waves.

4.3 Future Work

We have proposed that the source of the observed oscillations could be a changing index of refraction caused by auroral precipitation, but more research is needed to test this hypothesis. A new PolarDARN station has recently been completed at Clyde River. The line of sight of the new radar will intersect the line of sight of the Rankin Inlet radar at approximately the range where we observe oscillations. This provides an opportunity to make simultaneous observations of a localized region with multiple beams at orthogonal directions. This spatial resolution may prove useful in improving on spatial coherence estimates. Intersecting lines of sight could provide verification that the oscillations are caused by a localized disturbance that looks like a large-scale perturbation due to propagation effects in ground scatter. In other words, if one beam shows the presence of oscillations at a point of intersection and the other intersecting beam does not, this would indicate that the region causing oscillations is not located at the point of intersection.

Bibliography

Allan, W. and Poulter, E. M. (1992). ULF waves - Their relationship to the structure of the earth's magnetosphere. *Reports on Progress in Physics*, 55(5):533.

Bendat, J. S. and Piersol, A. G. (1966). *Measurement and analysis of random data*. New York:Wiley.

Blelly, P. L. and Alcaydé, D. (2007). Ionosphere. In Kamide, Y. and Chian, A., editors, *Handbook of the Solar-Terrestrial Environment*. Springer.

Bourdillon, A., Delloue, J., and Parent, J. (1989). Effects of geomagnetic pulsations on the Doppler shift of HF backscatter radar echoes. *Radio Science*, 24(2):183–195.

Burgess, D. (1995). Collisionless shocks. In Kivelson, M. G. and Russell, C. T., editors, *Introduction to space physics*. Cambridge University Press.

Carlson, H. C. and Egeland, A. (1995). The aurora and the auroral ionosphere. In Kivelson, M. G. and Russell, C. T., editors, *Introduction to space physics*. Cambridge University Press.

Chisham, G., Lester, M., Milan, S. E., Freeman, M. P., Bristow, W. A., Grocott, A., McWilliams, K. A., Ruohoniemi, J. M., Yeoman, T. K., et al. (2007). A decade of the super dual auroral radar network (SuperDARN): scientific achievements, new techniques and future directions. *Surveys in Geophysics*, 28(1):33–109.

Chugunova, O. M., Pilipenko, V. F., Engebretson, M., and Rodger, A. S. (2006). Statistical characteristics of the spatial distribution of Pc3-4 geomagnetic pulsations at high latitudes in the antarctic regions. *Geomagnetism and Aeronomy*, 46(1):64–73.

Chugunova, O. M., Pilipenko, V. F., Engebretson, M., and Rodger, A. S. (2007). Statistical relations between the probability of occurrence of Pc3-4 pulsations at high latitudes in the antarctic regions and the solar wind and IMF parameters. *Geomagnetism and Aeronomy*, 47(2):205–215.

Cross, R. (1988). *An introduction to Alfvén waves*. IOP Publishing Ltd.

Davies, K. (1990). *Ionospheric radio*. Number 31. IET Publishing.

De Lauretis, M., Francia, P., Vellante, M., Piancatelli, A., Villante, U., and Memmo, D. D. (2005). ULF geomagnetic pulsations in the southern polar cap: Simultaneous measurements near the cusp and the geomagnetic pole. *Journal of geophysical research*, 110(A11):A11204.

Engebretson, M., Posch, J., Pilipenko, V., and Chugunova, O. (2006). ULF waves at very high latitudes. *Geophysical Monograph Series*, 169:137–156.

Francia, P., Lauretis, M. D., Vellante, M., Villante, U., and Piancatelli, A. (2009). ULF geomagnetic pulsations at different latitudes in antarctica. *Annales geophysicae*, 27(9):3621–3629.

Fraser, B. J. (2003). Recent developments in magnetospheric diagnostics using ULF waves. *Space science reviews*, 107(1):149–156.

Fraser, B. J., Horwitz, J. L., Slavin, J. A., Dent, Z. C., and Mann, I. R. (2005). Heavy ion mass loading of the geomagnetic field near the plasmapause and ULF wave implications. *Geophysical research letters*, 32(4):L04102.

Fraser-Smith, A. C. (1982). ULF/lower-ELF electromagnetic field measurements in the polar caps. *Reviews of Geophysics*, 20(3):497–512.

Greenwald, R. A., Baker, K. B., Dudeney, J. R., Pinnock, M., Jones, T. B., Thomas, E. C., Villain, J. P., Cerisier, J. C., Senior, C., Hanuise, C., Hunsucker, R. D., Sofko, G., Koehler, J., Nielsen, E., Pellinen, R., Walker, A. D. M., Sato, M., and Yamagishi, H. (1995). DARN/SuperDARN. *Space Science Reviews*, 71:761–796.

Gul'elmi, A. V. (1974). Diagnostics of the magnetosphere and interplanetary medium by means of pulsations. *Space Science Reviews*, 16(3):331–345.

Hargreaves, J. K. (1992). *The solar-terrestrial environment*, volume 420. Cambridge University Press.

Howard, T. A. and Menk, F. W. (2001). Propagation of 10-50 mHz ULF waves with high spatial coherence at high latitudes. *Geophysical research letters*, 28(2):231–234.

Hughes, W. J. (1974). The effect of the atmosphere and ionosphere on long period magnetospheric micropulsations. *Planetary and Space Science*, 22(8):1157–1172.

Hughes, W. J. and Southwood, D. J. (1976). The screening of micropulsation signals by the atmosphere and ionosphere. *Journal of Geophysical Research*, 81(19):3234–3240.

Hundhausen, A. J. (1995). The solar wind. In Kivelson, M. G. and Russell, C. T., editors, *Introduction to space physics*. Cambridge University Press.

Jacobs, J. A., Kato, Y., Matsushita, S., and Troitskaya, V. A. (1964). Classification of geomagnetic micropulsations. *Geophysical Journal of the Royal Astronomical Society*, 8(3):341–342.

Kaufman, A. A., Kleinberg, R. L., and Hansen, R. (2009). *Principles of the Magnetic Methods in Geophysics*, volume 42 of *Methods in Geochemistry and Geophysics*. Elsevier.

Kivelson, M. G. (1995). Physics of space plasmas. In Kivelson, M. G. and Russell, C. T., editors, *Introduction to space physics*. Cambridge University Press.

Luhmann, J. G. (1995). Ionospheres. In Kivelson, M. G. and Russell, C. T., editors, *Introduction to space physics*. Cambridge University Press.

Mann, I., Milling, D., Rae, I., Ozeke, L., Kale, A., Kale, Z., Murphy, K., Parent, A., Usanova, M., Pahud, D., Lee, E. A., Amalraj, V., Wallis, D., Angelopoulos, V., Glassmeier, K. H., Russell, C., Auster, H. U., and Singer, H. (2008). The upgraded CARISMA magnetometer array in the THEMIS era. *Space Science Reviews*, 141:413–451. 10.1007/s11214-008-9457-6.

Parks, G. (1991). *Physics of space plasmas - An introduction*. Redwood City, CA; Addison-Wesley Publishing Co.

Parker, E. N. (1958). Dynamics of the interplanetary gas and magnetic fields. *The Astrophysical Journal*, 128:664.

Ponomarenko, P. V., Fraser, B. J., Menk, F. W., Ables, S. T., and Morris, R. J. (2002). Cusp-latitude Pc3 spectra: band-limited and power-law components. *Annales Geophysicae*, 20(10):1539–1551.

Ponomarenko, P. V., Menk, F., Waters, C. L., and Sciffer, M. D. (2005). Pc3-4 ULF waves observed by the SuperDARN Tiger radar. *Annales Geophysicae*, 23(4):1271–1280.

Ponomarenko, P. V., Menk, F. W., and Waters, C. L. (2003). Visualization of ULF waves in SuperDARN data. *Geophysical Research Letters*, 30(18):1926.

Ponomarenko, P. V., St-Maurice, J. P., Hussey, G. C., and Koustov, A. V. (2010a). HF ground scatter from the polar cap: Ionospheric propagation and ground surface effects. *Journal of Geophysical Research*, 115(A10):A10310.

Ponomarenko, P. V., St-Maurice, J. P., Waters, C. L., Gillies, R. G., and Koustov, A. V. (2009). Refractive index effects on the scatter volume location and doppler velocity estimates of ionospheric HF backscatter echoes. *Annales Geophysicae*, 27(11):4207.

Ponomarenko, P. V., Walters, C. L., and St-Maurice, J. P. (2010b). Upstream Pc3-4 waves: Experimental evidence of propagation to the nightside plasmapause/plasmatrough. *Geophysical Research Letters*, 37(22):L22102.

Ponomarenko, P. V. and Waters, C. L. (2006). Spectral width of SuperDARN echoes: measurement, use and physical interpretation. *Annales Geophysicae*, 24:115–128.

Ponomarenko, P. V., Waters, C. L., Sciffer, M. D., Fraser, B. J., and Samson, J. C. (2001). Spatial structure of ULF waves: Comparison of magnetometer and super dual auroral radar network data. *Journal of Geophysical Research*, 106:10509–10518.

Schunk, R. W. and Nagy, A. F. (2000). *Ionospheres: Physics*. Cambridge University Press.

Takahashi, K., McPherron, R. L., and Terasawa, T. (1984). Dependence of the spectrum of Pc3-4 pulsations on the interplanetary magnetic field. *Journal of Geophysical Research*, 89(A5):2770–2780.

Troitskaya, V. A. and Gul'Elmi, A. V. (1967). Geomagnetic micropulsations and diagnostics of the magnetosphere. *Space Science Reviews*, 7(5):689–768.

Vallée, M. A., Newitt, L., Mann, I. R., Moussaoui, M., Dumont, R., and Keating, P. (2007). The spatial and temporal characteristics of Pc3 geomagnetic activity over Canada in 2000, as a guide to planning the times of aeromagnetic surveys. *Pure and Applied Geophysics*, 164(1):161–176.

Villante, U., De Lauretis, M., Francia, P., Vellante, M., and Piancatelli, A. (2006). Experimental aspects of mid-frequency pulsations (f= 10–100 mHz) in the southern polar cap. *Space science reviews*, 122(1):107–117.

Villante, U., Vellante, M., and De Sanctis, G. (2000). An analysis of Pc3 and Pc4 pulsations at Terra Nova Bay (Antarctica). *Annales Geophysicae*, 18:1412–1421.

Waters, C. L. (2000). ULF resonance structure in the magnetosphere. *Advances in Space Research*, 25(7):1541–1558.

Wilson, C. R. (1967). Infrasonic pressure waves from the aurora: a shock wave model. *Nature*, 216:131–133.

Yumoto, K. (1985). Low-frequency upstream wave as a probable source of low-latitude Pc3-4 magnetic pulsations. *Planetary and Space Science*, 33(2):239–249.

Yumoto, K., Saito, T., Akasofu, S. I., Tsurutani, B. T., and Smith, E. J. (1985). Propagation mechanism of daytime Pc3-4 pulsations observed at synchronous orbit and multiple ground-based stations. *Journal of Geophysical Research*, 90(A7):6439–6450.

Appendix A

SuperDARN Scans

Year	Month	Start date	Start Time (UT)	End Time (UT)	Mode	Station	Beam(s)
2008	January	1	0	24	THEMIS	RKN	7
2008	January	4	18	24	THEMIS	RKN	7
2008	January	5	0	24	THEMIS	RKN	7
2008	January	8	18	24	THEMIS	RKN	7
2008	January	9	0	24	THEMIS	RKN	7
2008	January	12	18	24	THEMIS	RKN	7
2008	January	13	0	24	THEMIS	RKN	7
2008	January	14	0	24	THEMIS	RKN	7
2008	January	16	18	24	THEMIS	RKN	7
2008	January	17	0	24	THEMIS	RKN	7
2008	January	20	18	24	THEMIS	RKN	7
2008	January	21	0	24	THEMIS	RKN	7
2008	January	24	18	24	THEMIS	RKN	7
2008	January	25	0	24	THEMIS	RKN	7
2008	January	28	18	24	THEMIS	RKN	7
2008	January	29	0	24	THEMIS	RKN	7
2008	February	1	18	24	THEMIS	RKN	7
2008	February	2	0	24	THEMIS	RKN	7
2008	February	5	18	24	THEMIS	RKN	7
2008	February	6	0	24	THEMIS	RKN	7
2008	February	9	18	24	THEMIS	RKN	7
2008	February	10	0	24	THEMIS	RKN	7
2008	February	13	18	24	THEMIS	RKN	7
2008	February	14	0	24	THEMIS	RKN	7
2008	February	17	18	24	THEMIS	RKN	7
2008	February	18	0	24	THEMIS	RKN	7
2008	February	21	18	24	THEMIS	RKN	7
2008	February	22	0	24	THEMIS	RKN	7
2008	February	25	18	24	THEMIS	RKN	7
2008	February	26	0	24	THEMIS	RKN	7
2008	February	27	18	24	THEMIS	RKN	7
2008	February	28	0	6	THEMIS	RKN	7
2008	March	1	0	24	THEMIS	RKN	7
2008	March	4	18	24	THEMIS	RKN	7
2008	March	5	0	24	THEMIS	RKN	7
2008	March	9	2	24	THEMIS	RKN	7

Continued on next page

Table A.1 – continued from previous page

Year	Month	Date	Start Time (UT)	End Time (UT)	Mode	Station	Beam(s)
2008	March	12	18	24	THEMIS	RKN	7
2008	March	13	0	24	THEMIS	RKN	7
2008	March	14	0	24	THEMIS	RKN	7
2008	March	16	18	24	THEMIS	RKN	7
2008	March	17	0	24	THEMIS	RKN	7
2008	March	20	18	24	THEMIS	RKN	7
2008	March	21	0	24	THEMIS	RKN	7
2008	March	24	18	24	THEMIS	RKN	7
2008	March	25	0	24	THEMIS	RKN	7
2008	March	28	18	24	THEMIS	RKN	7
2008	March	29	0	24	THEMIS	RKN	7
2008	April	1	12	24	THEMIS	RKN	7
2008	April	2	0	12	THEMIS	RKN	7
2008	April	5	12	24	THEMIS	RKN	7
2008	April	6	0	12	THEMIS	RKN	7
2008	April	9	12	24	THEMIS	RKN	7
2008	April	10	0	12	THEMIS	RKN	7
2008	April	13	12	24	THEMIS	RKN	7
2008	April	14	0	12	THEMIS	RKN	7
2008	April	17	12	24	THEMIS	RKN	7
2008	April	18	0	12	THEMIS	RKN	7
2008	April	21	12	24	THEMIS	RKN	7
2008	April	22	0	12	THEMIS	RKN	7
2008	April	25	12	24	THEMIS	RKN	7
2008	April	26	0	12	THEMIS	RKN	7
2008	April	29	12	24	THEMIS	RKN	7
2008	April	30	0	12	THEMIS	RKN	7
2008	May	1	0	24	THEMIS	RKN	7
2008	May	7	0	24	THEMIS	RKN	7
2008	May	11	0	24	THEMIS	RKN	7
2008	May	15	0	24	THEMIS	RKN	7
2008	May	19	0	24	THEMIS	RKN	7
2008	May	27	0	24	THEMIS	RKN	7
2008	June	1	0	24	THEMIS	RKN	7
2008	June	2	0	24	THEMIS	RKN	7
2008	June	3	0	24	THEMIS	RKN	7
2008	June	4	0	24	THEMIS	RKN	7
2008	June	16	0	24	THEMIS	RKN	7
2008	June	21	0	24	THEMIS	RKN	7
2008	June	24	0	24	THEMIS	RKN	7
2008	June	25	0	24	THEMIS	RKN	7

Continued on next page

Table A.1 – continued from previous page

Year	Month	Date	Start Time (UT)	End Time (UT)	Mode	Station	Beam(s)
2008	July	1	0	24	THEMIS	RKN	7
2008	July	3	12	24	THEMIS	RKN	7
2008	July	5	0	6	THEMIS	RKN	7
2008	July	5	12	24	THEMIS	RKN	7
2008	July	6	0	6	THEMIS	RKN	7
2008	July	7	0	24	THEMIS	RKN	7
2008	July	11	0	24	THEMIS	RKN	7
2008	July	14	18	24	THEMIS	RKN	7
2008	July	15	0	24	THEMIS	RKN	7
2008	July	19	0	24	THEMIS	RKN	7
2008	July	23	0	24	THEMIS	RKN	7
2008	July	27	0	24	THEMIS	RKN	7
2008	July	31	0	24	THEMIS	RKN	7
2008	August	3	12	24	THEMIS	RKN	7
2008	August	4	0	6	THEMIS	RKN	7
2008	August	5	12	24	THEMIS	RKN	7
2008	August	6	0	12	THEMIS	RKN	7
2008	August	7	12	24	THEMIS	RKN	7
2008	August	8	0	6	THEMIS	RKN	7
2008	August	12	12	24	THEMIS	RKN	7
2008	August	13	0	12	THEMIS	RKN	7
2008	August	14	12	24	THEMIS	RKN	7
2008	August	15	0	12	THEMIS	RKN	7
2008	August	22	12	24	THEMIS	RKN	7
2008	August	23	0	12	THEMIS	RKN	7
2008	August	24	12	24	THEMIS	RKN	7
2008	August	25	0	12	THEMIS	RKN	7
2008	August	28	12	24	THEMIS	RKN	7
2008	August	29	0	12	THEMIS	RKN	7
2008	September	2	6	18	THEMIS	RKN	7
2008	September	3	12	24	THEMIS	RKN	7
2008	September	4	0	24	THEMIS	RKN	7
2008	September	5	0	24	THEMIS	RKN	7
2008	September	6	0	12	THEMIS	RKN	7
2008	September	9	6	24	THEMIS	RKN	7
2008	September	10	0	24	THEMIS	RKN	7
2008	September	11	0	12	THEMIS	RKN	7
2008	September	12	12	24	THEMIS	RKN	7
2008	September	13	0	12	THEMIS	RKN	7
2008	September	14	12	24	THEMIS	RKN	7
2008	September	15	0	12	THEMIS	RKN	7

Continued on next page

Table A.1 – continued from previous page

Year	Month	Date	Start Time (UT)	End Time (UT)	Mode	Station	Beam(s)
2008	September	16	0	24	THEMIS	RKN	7
2008	September	17	0	12	THEMIS	RKN	7
2008	September	18	12	24	THEMIS	RKN	7
2008	September	19	0	12	THEMIS	RKN	7
2008	September	21	0	24	THEMIS	RKN	7
2008	October	1	6	24	THEMIS	RKN	7
2008	October	2	0	6	THEMIS	RKN	7
2008	October	5	6	24	THEMIS	RKN	7
2008	October	6	0	6	THEMIS	RKN	7
2008	October	8	6	18	THEMIS	RKN	7
2008	October	9	6	24	THEMIS	RKN	7
2008	October	10	0	18	THEMIS	RKN	7
2008	October	11	8	18	THEMIS	RKN	7
2008	October	12	8	18	THEMIS	RKN	7
2008	October	13	0	24	THEMIS	RKN	7
2008	October	14	0	18	THEMIS	RKN	7
2008	October	15	6	18	THEMIS	RKN	7
2008	October	16	8	18	THEMIS	RKN	7
2008	October	17	6	24	THEMIS	RKN	7
2008	October	18	0	6	THEMIS	RKN	7
2008	October	21	6	24	THEMIS	RKN	7
2008	October	22	0	6	THEMIS	RKN	7
2008	October	25	6	24	THEMIS	RKN	7
2008	October	26	0	6	THEMIS	RKN	7
2008	October	29	6	24	THEMIS	RKN	7
2008	October	30	0	6	THEMIS	RKN	7
2008	October	31	0	18	THEMIS	RKN	7
2008	November	1	12	24	THEMIS	RKN	7
2008	November	3	12	24	THEMIS	RKN	7
2008	November	4	6	24	THEMIS	RKN	7
2008	November	5	0	6	THEMIS	RKN	7
2008	November	7	12	24	THEMIS	RKN	7
2008	November	8	6	24	THEMIS	RKN	7
2008	November	9	0	6	THEMIS	RKN	7
2008	November	9	12	24	THEMIS	RKN	7
2008	November	11	12	24	THEMIS	RKN	7
2008	November	12	6	24	THEMIS	RKN	7
2008	November	13	0	6	THEMIS	RKN	7
2008	November	16	6	24	THEMIS	RKN	7
2008	November	17	0	6	THEMIS	RKN	7
2008	November	20	6	24	THEMIS	RKN	7

Continued on next page

Table A.1 – continued from previous page

Year	Month	Date	Start Time (UT)	End Time (UT)	Mode	Station	Beam(s)
2008	November	21	0	12	THEMIS	RKN	7
2008	November	24	0	24	THEMIS	RKN	7
2008	November	25	0	6	THEMIS	RKN	7
2008	November	28	0	24	THEMIS	RKN	7
2008	November	29	0	12	THEMIS	RKN	7
2008	December	2	0	18	THEMIS	RKN	7
2008	December	6	0	18	THEMIS	RKN	7
2008	December	10	0	18	THEMIS	RKN	7
2008	December	14	0	18	THEMIS	RKN	7
2008	December	22	6	18	THEMIS	RKN	7
2008	December	26	6	18	THEMIS	RKN	7
2009	January	1	0	8	ULF	RKN INV	[0,4,8], [8,12,15]
2009	January	2	0	24	ULF	RKN INV	[0,4,8], [8,12,15]
2009	January	3	0	8	ULF	RKN INV	[0,4,8], [8,12,15]
2009	January	4	0	8	ULF	RKN INV	[0,4,8], [8,12,15]
2009	January	5	0	8	ULF	RKN INV	[0,4,8], [8,12,15]
2009	January	6	0	18	ULF	RKN INV	[0,4,8], [8,12,15]
2009	January	10	0	24	ULF	RKN INV	[0,4,8], [8,12,15]
2009	January	12	0	12	ULF	RKN INV	[0,4,8], [8,12,15]
2009	January	14	0	24	ULF	RKN INV	[0,4,8], [8,12,15]
2009	January	18	0	24	ULF	RKN INV	[0,4,8], [8,12,15]
2009	January	22	0	24	ULF	RKN INV	[0,4,8], [8,12,15]
2009	January	24	18	24	ULF	RKN INV	[0,4,8], [8,12,15]
2009	January	25	0	6	ULF	RKN INV	[0,4,8], [8,12,15]
2009	January	26	0	24	ULF	RKN INV	[0,4,8], [8,12,15]
2009	January	27	0	8	ULF	RKN INV	[0,4,8], [8,12,15]

Continued on next page

Table A.1 – continued from previous page

Year	Month	Date	Start Time (UT)	End Time (UT)	Mode	Station	Beam(s)
2009	January	28	0	8	ULF	RKN INV	[0,4,8], [8,12,15]
2009	January	29	0	8	ULF	RKN INV	[0,4,8], [8,12,15]
2009	January	30	0	24	ULF	RKN INV	[0,4,8], [8,12,15]
2009	January	31	0	8	ULF	RKN INV	[0,4,8], [8,12,15]
2009	February	2	18	24	ULF	RKN INV	[0,4,8], [8,12,15]
2009	February	3	0	24	ULF	RKN INV	[0,4,8], [8,12,15]
2009	February	7	0	24	ULF	RKN INV	[0,4,8], [8,12,15]
2009	February	8	0	6	ULF	RKN INV	[0,4,8], [8,12,15]
2009	February	10	18	24	ULF	RKN INV	[0,4,8], [8,12,15]
2009	February	11	0	24	ULF	RKN INV	[0,4,8], [8,12,15]
2009	February	15	0	24	ULF	RKN INV	[0,4,8], [8,12,15]
2009	February	18	12	24	ULF	RKN INV	[0,4,8], [8,12,15]
2009	February	19	0	24	ULF	RKN INV	[0,4,8], [8,12,15]
2009	February	22	0	24	ULF	RKN INV	[0,4,8], [8,12,15]
2009	February	23	0	6	ULF	RKN INV	[0,4,8], [8,12,15]
2009	February	26	0	24	ULF	RKN INV	[0,4,8], [8,12,15]
2009	February	27	0	12	ULF	RKN INV	[0,4,8], [8,12,15]
2009	March	2	6	24	ULF	RKN INV	[0,4,8], [8,12,15]
2009	March	3	0	12	ULF	RKN INV	[0,4,8], [8,12,15]
2009	March	4	12	24	ULF	RKN INV	[0,4,8], [8,12,15]
2009	March	5	0	24	ULF	RKN INV	[0,4,8], [8,12,15]

Continued on next page

Table A.1 – continued from previous page

Year	Month	Date	Start Time (UT)	End Time (UT)	Mode	Station	Beam(s)
2009	March	12	6	24	ULF	RKN INV	[0,4,8], [8,12,15]
2009	March	13	0	12	ULF	RKN INV	[0,4,8], [8,12,15]
2009	March	16	0	24	ULF	RKN INV	[0,4,8], [8,12,15]
2009	March	17	0	12	ULF	RKN INV	[0,4,8], [8,12,15]
2009	March	18	12	24	ULF	RKN INV	[0,4,8], [8,12,15]
2009	March	19	0	12	ULF	RKN INV	[0,4,8], [8,12,15]
2009	March	24	6	24	ULF	RKN INV	[0,4,8], [8,12,15]
2009	March	25	0	12	ULF	RKN INV	[0,4,8], [8,12,15]
2009	March	26	12	24	ULF	RKN INV	[0,4,8], [8,12,15]
2009	March	27	0	12	ULF	RKN INV	[0,4,8], [8,12,15]
2009	March	28	6	24	ULF	RKN INV	[0,4,8], [8,12,15]
2009	March	29	0	18	ULF	RKN INV	[0,4,8], [8,12,15]
2009	March	30	0	24	ULF	RKN INV	[0,4,8], [8,12,15]
2009	March	31	0	12	ULF	RKN INV	[0,4,8], [8,12,15]
2009	April	3	0	24	ULF	RKN INV	[0,4,8], [8,12,15]
2009	April	4	0	6	ULF	RKN INV	[0,4,8], [8,12,15]
2009	April	5	0	12	ULF	RKN INV	[0,4,8], [8,12,15]
2009	April	7	0	24	ULF	RKN INV	[0,4,8], [8,12,15]
2009	April	8	0	6	ULF	RKN INV	[0,4,8], [8,12,15]
2009	April	11	0	24	ULF	RKN INV	[0,4,8], [8,12,15]
2009	April	12	0	6	ULF	RKN INV	[0,4,8], [8,12,15]

Continued on next page

Table A.1 – continued from previous page

Year	Month	Date	Start Time (UT)	End Time (UT)	Mode	Station	Beam(s)
2009	April	13	0	24	ULF	RKN INV	[0,4,8], [8,12,15]
2009	April	14	0	24	ULF	RKN INV	[0,4,8], [8,12,15]
2009	April	15	0	24	ULF	RKN INV	[0,4,8], [8,12,15]
2009	April	16	0	6	ULF	RKN INV	[0,4,8], [8,12,15]
2009	April	19	0	24	ULF	RKN INV	[0,4,8], [8,12,15]
2009	April	20	0	6	ULF	RKN INV	[0,4,8], [8,12,15]
2009	April	21	12	24	ULF	RKN INV	[0,4,8], [8,12,15]
2009	April	23	6	24	ULF	RKN INV	[0,4,8], [8,12,15]
2009	April	24	0	6	ULF	RKN INV	[0,4,8], [8,12,15]
2009	April	26	18	24	ULF	RKN INV	[0,4,8], [8,12,15]
2009	April	28	0	12	ULF	RKN INV	[0,4,8], [8,12,15]
2009	May	1	0	24	ULF	RKN INV	[0,4,8], [8,12,15]
2009	May	2	0	24	ULF	RKN INV	[0,4,8], [8,12,15]
2009	May	3	0	24	ULF	RKN INV	[0,4,8], [8,12,15]
2009	May	4	0	6	ULF	RKN INV	[0,4,8], [8,12,15]
2009	May	5	0	24	ULF	RKN INV	[0,4,8], [8,12,15]
2009	May	6	0	6	ULF	RKN INV	[0,4,8], [8,12,15]
2009	May	7	6	24	ULF	RKN INV	[0,4,8], [8,12,15]
2009	May	9	0	24	ULF	RKN INV	[0,4,8], [8,12,15]
2009	May	10	0	24	ULF	RKN INV	[0,4,8], [8,12,15]
2009	May	11	0	24	ULF	RKN INV	[0,4,8], [8,12,15]

Continued on next page

Table A.1 – continued from previous page

Year	Month	Date	Start Time (UT)	End Time (UT)	Mode	Station	Beam(s)
2009	May	12	6	18	ULF	RKN INV	[0,4,8], [8,12,15]
2009	May	13	0	24	ULF	RKN INV	[0,4,8], [8,12,15]
2009	May	17	0	24	ULF	RKN INV	[0,4,8], [8,12,15]
2009	May	21	0	6	ULF	RKN INV	[0,4,8], [8,12,15]
2009	May	21	0	24	ULF	RKN INV	[0,4,8], [8,12,15]
2009	May	22	18	24	ULF	RKN INV	[0,4,8], [8,12,15]
2009	May	23	0	6	ULF	RKN INV	[0,4,8], [8,12,15]
2009	May	25	12	24	ULF	RKN INV	[0,4,8], [8,12,15]
2009	May	26	0	12	ULF	RKN INV	[0,4,8], [8,12,15]
2009	May	27	18	24	ULF	RKN INV	[0,4,8], [8,12,15]
2009	May	28	0	12	ULF	RKN INV	[0,4,8], [8,12,15]
2009	June	2	12	24	ULF	RKN INV	[0,4,8], [8,12,15]
2009	June	4	18	24	ULF	RKN INV	[0,4,8], [8,12,15]
2009	June	5	0	6	ULF	RKN INV	[0,4,8], [8,12,15]
2009	June	5	18	24	ULF	RKN INV	[0,4,8], [8,12,15]
2009	June	10	18	24	ULF	RKN INV	[0,4,8], [8,12,15]
2009	June	11	0	6	ULF	RKN INV	[0,4,8], [8,12,15]
2009	June	12	0	24	ULF	RKN INV	[0,4,8], [8,12,15]
2009	June	13	0	24	ULF	RKN INV	[0,4,8], [8,12,15]
2009	June	14	0	24	ULF	RKN INV	[0,4,8], [8,12,15]
2009	June	18	6	24	ULF	RKN INV	[0,4,8], [8,12,15]

Continued on next page

Table A.1 – continued from previous page

Year	Month	Date	Start Time (UT)	End Time (UT)	Mode	Station	Beam(s)
2009	June	19	0	6	ULF	RKN INV	[0,4,8], [8,12,15]
2009	June	23	12	24	ULF	RKN INV	[0,4,8], [8,12,15]
2009	June	27	6	24	ULF	RKN INV	[0,4,8], [8,12,15]
2009	June	30	12	24	ULF	RKN INV	[0,4,8], [8,12,15]
2009	July	1	0	6	ULF	RKN INV	[0,4,8], [8,12,15]
2009	July	2	6	24	ULF	RKN INV	[0,4,8], [8,12,15]
2009	July	3	0	6	ULF	RKN INV	[0,4,8], [8,12,15]
2009	July	4	0	24	ULF	RKN INV	[0,4,8], [8,12,15]
2009	July	5	0	6	ULF	RKN INV	[0,4,8], [8,12,15]
2009	July	9	0	24	ULF	RKN INV	[0,4,8], [8,12,15]
2009	July	10	0	6	ULF	RKN INV	[0,4,8], [8,12,15]
2009	July	12	6	12	ULF	RKN INV	[0,4,8], [8,12,15]
2009	July	14	12	24	ULF	RKN INV	[0,4,8], [8,12,15]
2009	July	15	0	12	ULF	RKN INV	[0,4,8], [8,12,15]
2009	July	17	12	24	ULF	RKN INV	[0,4,8], [8,12,15]
2009	July	19	18	24	ULF	RKN INV	[0,4,8], [8,12,15]
2009	July	20	0	24	ULF	RKN INV	[0,4,8], [8,12,15]
2009	July	21	0	18	ULF	RKN INV	[0,4,8], [8,12,15]
2009	July	22	0	24	ULF	RKN INV	[0,4,8], [8,12,15]
2009	July	23	0	24	ULF	RKN INV	[0,4,8], [8,12,15]
2009	July	24	0	24	ULF	RKN INV	[0,4,8], [8,12,15]

Continued on next page

Table A.1 – continued from previous page

Year	Month	Date	Start Time (UT)	End Time (UT)	Mode	Station	Beam(s)
2009	July	29	0	24	ULF	RKN INV	[0,4,8], [8,12,15]
2009	August	1	12	24	ULF	RKN INV	[0,4,8], [8,12,15]
2009	August	2	0	6	ULF	RKN INV	[0,4,8], [8,12,15]
2009	August	2	18	24	ULF	RKN INV	[0,4,8], [8,12,15]
2009	August	3	18	24	ULF	RKN INV	[0,4,8], [8,12,15]
2009	August	4	12	18	ULF	RKN INV	[0,4,8], [8,12,15]
2009	August	5	12	24	ULF	RKN INV	[0,4,8], [8,12,15]
2009	August	6	0	12	ULF	RKN INV	[0,4,8], [8,12,15]
2009	August	6	18	24	ULF	RKN INV	[0,4,8], [8,12,15]
2009	August	7	18	24	ULF	RKN INV	[0,4,8], [8,12,15]
2009	August	8	0	6	ULF	RKN INV	[0,4,8], [8,12,15]
2009	August	9	12	24	ULF	RKN INV	[0,4,8], [8,12,15]
2009	August	10	0	6	ULF	RKN INV	[0,4,8], [8,12,15]
2009	August	10	18	24	ULF	RKN INV	[0,4,8], [8,12,15]
2009	August	11	18	24	ULF	RKN INV	[0,4,8], [8,12,15]
2009	August	12	0	6	ULF	RKN INV	[0,4,8], [8,12,15]
2009	August	22	6	0	ULF	RKN INV	[0,4,8], [8,12,15]
2009	August	23	0	24	ULF	RKN INV	[0,4,8], [8,12,15]
2009	August	24	0	24	ULF	RKN INV	[0,4,8], [8,12,15]
2009	September	15	6	0	ULF	RKN INV	[0,4,8], [8,12,15]
2009	September	16	0	24	ULF	RKN INV	[0,4,8], [8,12,15]

Continued on next page

Table A.1 – continued from previous page

Year	Month	Date	Start Time (UT)	End Time (UT)	Mode	Station	Beam(s)
2009	September	17	0	24	ULF	RKN INV	[0,4,8], [8,12,15]
2009	September	18	0	6	ULF	RKN INV	[0,4,8], [8,12,15]
2009	October	14	0	24	ULF	RKN INV	[0,4,8], [8,12,15]
2009	October	15	0	24	ULF	RKN INV	[0,4,8], [8,12,15]
2009	October	16	0	24	ULF	RKN INV	[0,4,8], [8,12,15]
2009	October	17	0	12	ULF	RKN INV	[0,4,8], [8,12,15]
2009	November	19	0	24	ULF	RKN INV	[0,4,8], [8,12,15]
2009	November	20	0	24	ULF	RKN INV	[0,4,8], [8,12,15]
2009	November	21	0	12	ULF	RKN INV	[0,4,8], [8,12,15]
2009	December	21	0	24	ULF	RKN INV	[0,4,8], [8,12,15]
2009	December	22	0	24	ULF	RKN INV	[0,4,8], [8,12,15]
2009	December	23	0	24	ULF	RKN INV	[0,4,8], [8,12,15]
2010	January	7	0	24	ULF	RKN INV	[0,4,8], [8,12,15]
2010	January	8	0	24	ULF	RKN INV	[0,4,8], [8,12,15]
2010	January	9	0	24	ULF	RKN INV	[0,4,8], [8,12,15]
2010	February	1	0	24	THEMIS	SAS	6
2010	February	2	0	12	THEMIS	SAS	6
2010	February	4	0	24	THEMIS	SAS	6
2010	February	5	0	12	THEMIS	SAS	6
2010	February	8	0	24	THEMIS	SAS	6
2010	February	9	0	24	ULF	RKN INV	[0,4,8], [8,12,15]
2010	February	10	0	24	ULF	RKN INV	[0,4,8], [8,12,15]
2010	February	11	0	24	ULF	RKN INV	[0,4,8], [8,12,15]

Continued on next page

Table A.1 – continued from previous page

Year	Month	Date	Start Time (UT)	End Time (UT)	Mode	Station	Beam(s)
2010	February	12	0	24	ULF	RKN INV	[0,4,8], [8,12,15]
2010	February	13	0	24	THEMIS	SAS	6
2010	February	15	6	24	THEMIS	SAS	6
2010	February	16	0	6	THEMIS	SAS	6
2010	February	20	0	18	THEMIS	SAS	6
2010	February	22	6	24	THEMIS	SAS	6
2010	February	23	0	6	THEMIS	SAS	6
2010	February	26	18	24	THEMIS	SAS	6
2010	February	26	18	24	THEMIS	SAS	6
2010	February	27	0	6	THEMIS	SAS	6
2010	February	27	0	6	THEMIS	SAS	6
2010	March	1	0	24	THEMIS	SAS	6
2010	March	2	0	24	THEMIS	SAS	6
2010	March	3	0	24	THEMIS	SAS	6
2010	March	10	0	24	THEMIS	SAS	6
2010	March	11	0	24	THEMIS	SAS	6
2010	March	12	0	24	THEMIS	SAS	6
2010	March	13	0	24	ULF	RKN INV	[0,4,8], [8,12,15]
2010	March	14	0	24	ULF	RKN INV	[0,4,8], [8,12,15]
2010	March	15	0	24	ULF	RKN INV	[0,4,8], [8,12,15]
2010	March	19	0	24	THEMIS	SAS	6
2010	March	20	0	24	THEMIS	SAS	6
2010	March	21	0	24	THEMIS	SAS	6
2010	March	27	0	24	THEMIS	SAS	6
2010	March	28	0	24	THEMIS	SAS	6
2010	March	29	0	24	THEMIS	SAS	6
2010	April	1	0	24	THEMIS	SAS	6
2010	April	2	0	24	THEMIS	SAS	6
2010	April	3	0	24	THEMIS	SAS	6
2010	April	4	0	24	THEMIS	SAS	6
2010	April	6	0	18	THEMIS	SAS	6
2010	April	7	0	12	THEMIS	SAS	6
2010	April	8	6	24	THEMIS	SAS	6
2010	April	9	0	6	THEMIS	SAS	6
2010	April	10	12	24	THEMIS	SAS	6
2010	April	11	0	12	THEMIS	SAS	6
2010	April	13	0	28	THEMIS	SAS	6

Continued on next page

Table A.1 – continued from previous page

Year	Month	Date	Start Time (UT)	End Time (UT)	Mode	Station	Beam(s)
2010	April	14	0	6	THEMIS	SAS	6
2010	April	15	0	24	THEMIS	SAS	6
2010	April	16	0	12	THEMIS	SAS	6
2010	April	20	0	24	ULF	RKN INV	[0,4,8], [8,12,15]
2010	April	21	0	24	ULF	RKN INV	[0,4,8], [8,12,15]
2010	April	22	0	24	ULF	RKN INV	[0,4,8], [8,12,15]
2010	April	23	0	12	THEMIS	SAS	6
2010	April	24	6	24	THEMIS	SAS	6
2010	May	1	12	18	THEMIS	SAS	6
2010	May	3	6	24	THEMIS	SAS	6
2010	May	5	18	24	THEMIS	SAS	6
2010	May	6	0	6	THEMIS	SAS	6
2010	May	8	0	12	THEMIS	SAS	6
2010	May	12	0	24	THEMIS	SAS	6
2010	May	13	0	12	THEMIS	SAS	6
2010	May	14	12	24	THEMIS	SAS	6
2010	May	15	0	6	THEMIS	SAS	6
2010	May	17	0	12	THEMIS	SAS	6
2010	May	19	0	12	THEMIS	SAS	6
2010	May	21	0	12	THEMIS	SAS	6
2010	May	23	18	24	THEMIS	SAS	6
2010	May	24	0	12	THEMIS	SAS	6
2010	May	26	6	18	THEMIS	SAS	6
2010	May	28	0	18	THEMIS	SAS	6
2010	May	30	6	24	THEMIS	SAS	6
2010	June	2	0	12	THEMIS	SAS	6
2010	June	5	18	24	THEMIS	SAS	6
2010	June	6	0	6	THEMIS	SAS	6
2010	June	8	0	12	THEMIS	SAS	6
2010	June	11	0	12	THEMIS	SAS	6
2010	June	14	18	24	THEMIS	SAS	6
2010	June	15	0	12	THEMIS	SAS	6
2010	June	16	6	24	THEMIS	SAS	6
2010	June	19	18	24	THEMIS	SAS	6
2010	June	20	0	12	THEMIS	SAS	6
2010	June	23	18	24	THEMIS	SAS	6
2010	June	24	0	12	THEMIS	SAS	6
2010	June	28	6	12	THEMIS	SAS	6

Continued on next page

Table A.1 – continued from previous page

Year	Month	Date	Start Time (UT)	End Time (UT)	Mode	Station	Beam(s)
2010	June	30	12	24	THEMIS	SAS	6
2010	July	2	12	24	THEMIS	SAS	6
2010	July	6	6	18	THEMIS	SAS	6
2010	July	7	6	24	THEMIS	SAS	6
2010	July	8	0	6	THEMIS	SAS	6
2010	July	9	12	24	THEMIS	SAS	6
2010	July	10	0	6	THEMIS	SAS	6
2010	July	11	12	24	THEMIS	SAS	6
2010	July	12	0	12	THEMIS	SAS	6
2010	July	13	12	24	THEMIS	SAS	6
2010	July	14	0	12	THEMIS	SAS	6
2010	July	15	6	18	THEMIS	SAS	6
2010	July	16	0	18	THEMIS	SAS	6
2010	July	18	0	24	THEMIS	SAS	6
2010	July	19	0	24	THEMIS	SAS	6
2010	July	20	0	24	ULF	RKN	[5,7,8]
2010	July	21	0	24	ULF	RKN	[5,7,8]
2010	July	22	0	24	ULF	RKN	[5,7,8]
2010	July	23	0	24	ULF	RKN	[5,7,8]
2010	October	16	0	24	ULF	RKN INV	[5,7,8], [7,8,10]
2010	October	17	0	24	ULF	RKN INV	[5,7,8], [7,8,10]
2010	October	18	0	24	ULF	RKN INV	[5,7,8], [7,8,10]
2010	October	19	0	24	ULF	RKN INV	[5,7,8], [7,8,10]
2012	October	14	0	24	ULF	SAS PGR	[5,7,8], [5,7,8]
2012	October	15	0	24	ULF	SAS PGR	[5,7,8], [5,7,8]
2012	October	16	0	24	ULF	SAS PGR	[5,7,8], [5,7,8]
2012	October	17	0	24	ULF	SAS PGR	[5,7,8], [5,7,8]
2012	May	5	12	24	ULF	SAS PGR	[5,7,8], [5,7,8]
2012	May	6	0	24	ULF	SAS PGR	[5,7,8], [5,7,8]
2012	May	7	0	6	ULF	SAS PGR	[5,7,8], [5,7,8]

Continued on next page

Table A.1 – continued from previous page

Year	Month	Date	Start Time (UT)	End Time (UT)	Mode	Station	Beam(s)
2012	May	10	0	24	ULF	SAS PGR	[5,7,8], [5,7,8]
2012	May	11	0	24	ULF	SAS PGR	[5,7,8], [5,7,8]
2012	July	19	0	24	ULF	SAS PGR	[5,7,8], [5,7,8]
2012	July	20	0	24	ULF	SAS PGR	[5,7,8], [5,7,8]
2012	July	21	0	24	ULF	SAS PGR	[5,7,8], [5,7,8]
2012	July	22	0	24	ULF	SAS PGR	[5,7,8], [5,7,8]
2012	July	23	0	24	ULF	SAS PGR	[5,7,8], [5,7,8]
2012	July	24	0	24	ULF	SAS PGR	[5,7,8], [5,7,8]
2012	July	25	0	24	ULF	SAS PGR	[5,7,8], [5,7,8]
2012	July	26	0	24	ULF	SAS PGR	[5,7,8], [5,7,8]
2012	July	27	0	24	ULF	SAS PGR	[5,7,8], [5,7,8]
2012	August	5	0	24	ULF	SAS PGR	[5,7,8], [5,7,8]
2012	August	6	0	24	ULF	SAS PGR	[5,7,8], [5,7,8]
2012	August	7	0	24	ULF	SAS PGR	[5,7,8], [5,7,8]
2012	August	8	0	24	ULF	SAS PGR	[5,7,8], [5,7,8]
2012	August	9	0	24	ULF	SAS PGR	[5,7,8], [5,7,8]
2012	September	14	0	24	ULF	SAS PGR	[5,7,8], [5,7,8]
2012	September	15	0	24	ULF	SAS PGR	[5,7,8], [5,7,8]
2012	September	16	0	24	ULF	SAS PGR	[5,7,8], [5,7,8]
2012	September	17	0	24	ULF	SAS PGR	[5,7,8], [5,7,8]
2012	September	18	0	6	ULF	SAS PGR	[5,7,8], [5,7,8]

Continued on next page

Table A.1 – continued from previous page

Year	Month	Date	Start Time (UT)	End Time (UT)	Mode	Station	Beam(s)

Table A.1: SuperDARN scans used

Appendix B

2008 Magnetometer Scans

Year	Month	Day
2008	May	1
2008	May	2
2008	May	3
2008	May	4
2008	May	5
2008	May	6
2008	May	7
2008	May	8
2008	May	9
2008	May	10
2008	May	11
2008	May	12
2008	May	13
2008	May	14
2008	May	15
2008	May	16
2008	May	17
2008	May	18
2008	May	19
2008	May	20
2008	May	21
2008	May	22
2008	May	23
2008	May	24
2008	May	25
2008	May	26
2008	May	27
2008	May	28
2008	May	29
2008	May	30
2008	May	31
2008	June	1
2008	June	2
2008	June	3
2008	June	4
2008	June	5
2008	June	6
2008	June	7

Continued on next page

Table B.1 – continued from previous page

Year	Month	Day
2008	June	9
2008	June	10
2008	June	12
2008	June	13
2008	June	14
2008	June	15
2008	June	16
2008	June	17
2008	June	18
2008	June	19
2008	June	20
2008	June	21
2008	June	22
2008	June	23
2008	June	24
2008	June	25
2008	June	26
2008	June	27
2008	June	28
2008	June	29
2008	July	1
2008	July	2
2008	July	3
2008	July	4
2008	July	5
2008	July	6
2008	July	7
2008	July	8
2008	July	9
2008	July	11
2008	July	12
2008	July	13
2008	July	14
2008	July	15
2008	July	16
2008	July	17
2008	July	18
2008	July	22
2008	July	23
2008	July	25
2008	July	26
2008	July	29
2008	July	30

Continued on next page

Table B.1 – continued from previous page

Year	Month	Day
2008	July	31
2008	August	1
2008	August	2
2008	August	5
2008	August	6
2008	August	7
2008	August	8
2008	August	9
2008	August	10
2008	August	11
2008	August	14
2008	August	15
2008	August	16
2008	August	17
2008	August	18
2008	August	22
2008	August	23

Table B.1: Taloyoak magnetometer data used to determine the diurnal dynamic spectra.